ADVANCED INTRAVASCULAR MAGNETIC RESONANCE IMAGING WITH INTERACTION

by
Xiaoyang Liu

A dissertation submitted to Johns Hopkins University in conformity with the requirements for the degree of Doctor of Philosophy

Baltimore, Maryland
May 2022

Abstract

Intravascular (IV) Magnetic Resonance Imaging (MRI) is a specialized class of interventional MRI (iMRI) techniques that acquire MRI images through blood vessels to guide, identify and/or treat pathologies inside the human body which are otherwise difficult to locate and treat precisely. Here, interactions based on real-time computations and feedback are explored to improve the accuracy and efficiency of IVMRI procedures.

First, an IV MRI-guided high-intensity focused ultrasound (HIFU) ablation method is developed for targeting perivascular pathology with minimal injury to the vessel wall. To take advantage of real-time feedback, a software interface is developed for monitoring thermal dose with real-time MRI thermometry, and an MRI-guided ablation protocol developed and tested on muscle and liver tissue *ex vivo.* It is shown that, with cumulative thermal dose monitored with MRI thermometry, lesion location and dimensions can be estimated consistently, and desirable thermal lesions can be achieved in animals *in vivo*.

Second, to achieve fully interactive IV MRI, high-resolution real-time 10 frames-per-second (fps) MRI endoscopy is developed as an advance over prior methods of MRI endoscopy. Intravascular transmit-receive MRI endoscopes are fabricated for highly under-sampled radial-projection MRI in a clinical 3Tesla MRI scanner. Iterative nonlinear reconstruction is accelerated using graphics processor units (GPU) to achieve true real-time endoscopy visualization at the scanner. The results of high-speed MRI endoscopy at 6-10 fps are consistent with fully-sampled MRI endoscopy and histology, with feasibility demonstrated *in vivo* in a large animal model.

Last, a general framework for automatic imaging contrast tuning over MRI protocol parameters is explored. The framework reveals typical signal patterns over different protocol parameters from calibration imaging data and applies this knowledge to design efficient acquisition strategies and predicts contrasts under unacquired protocols. An external computer in real-time communication with the MRI console is utilized for online processing and controlling MRI acquisitions. This workflow enables machine learning for optimizing acquisition strategies in general, and provides a foundation for efficiently tuning MRI protocol parameters to perform interventional MRI in the highly varying and interactive environments commonly in play. This work is loosely inspired by prior research on extremely accelerated MRI relaxometry using the minimal-acquisition linear algebraic modeling (SLAM) method.

Advisor and first reader: Paul A. Bottomley

Russell H. Morgan Professor, Department of Radiology and Radiological Science, Johns Hopkins University

Second reader: Jerry L. Prince

William B. Kouwenhoven Professor, Department of Electrical and Computer Engineering, Whiting School of Engineering, Johns Hopkins University

Acknowledgements

First of all, my sincere gratitude goes to my research advisor, Dr. Paul A. Bottomley. He has set a huge role model in pioneering the field of MRI with endless curiosity and passion for five decades. As a true innovator, he always fully supports me to explore the wildest ideas and shares his keen perspective on meanings of research. I will always remember his favorite quotation of *the unreasonable man*[†]. I am thankful for all his patient guidance and training for me in critical thinking, research strategizing, experiment design, scientific writing, and presentation skills.

Second, I would like to thank Parag Karmarkar. He is a great and talented engineer with extensive experience in interventional medical devices. He taught me how to make an MR coil when I had no idea for what the tools were in our RF lab. His way of teaching through hands-on experience is most effective. He also provided great support for all our interventional studies with instrument fabrication, experiment logistics and team organization. Besides a colleague and instructor, he is also a generous friend who never hesitates to offer his help.

Besides, I would like to thank Dr. Nicholas Ellens. He trained me on numerous things about HIFU and MR-guided interventions with great patience. It was with his training that I was able to later on carry out these studies independently. His collaboration and guidance were among those most important things that happened not only to my projects, but also to my academic career. He is also a good lab mate whose brightness and buoyancy inspired me through those hard times.

[†] The reasonable man adapts himself to the world; the unreasonable one persists in trying to adapt the world to himself. Therefore all progress depends on the unreasonable man. — George Bernard Shaw, *Man and Superman*

I want to thank Dr. Dara L. Kraitchman, who provided great help with her veterinary expertise in so many studies. I really appreciate her energy and perseverance in these time-consuming experiments. I want to thank Dr. Clifford R. Weiss. We would not be able to perform some of the extremely difficult intravascular experiments without his excellent skills in interventional radiology and generous help. I want to thank Dr. Jens Frahm and Dr. Dirk Voit, who helped us set up and maintain the first and sole real-time MRI system in the Western Hemisphere. I want to thank Dr. Everette C. Burdette for his collaboration on intravascular HIFU with his innovation and entrepreneurship. I want to thank Emery Williams for his collaboration on ultrasound transducers and catheters.

I want to thank Dr. Yi Zhang for guiding me with his knowledgeable perspective of MRI and research. I want to thank Dr. Guan Wang for her training me in IVMRI and for her helpful advice. I want to thank Dr. Shashank S. Hegde for providing detailed instructions on MRI endoscopy. I want to thank Dr. Dan Zhu for her help and smart ideas on my research. I want to thank Meiyappan Solaiyappan for helping me with his experience in computer science. I want to thank Dr. Dengrong Jiang for his informative discussion and hospitality. I want to thank Dr. Zhiliang Wei for his advice and help. I want to thank Dr. Gabriele Bonanno for his help on imaging software. I want to thank Dr. Tao Xiong for his help during my graduate study.

I want to thank Dr. Jinyuan Zhou, Dr. Dan Wu, Dr. Ye Qiao, Dr. Hanzhang Lu, Dr. Peiying Liu, Dr. Li Pan, Dr. Shanshan Jiang, Dr. Miroslaw Janowski, Dr. Piotr Walczak, Dr. Yingli Fu, and Dr. Peter Barker, as they all have given me advice and help on research and experiments. There is always something to learn from their intelligence and diligence. I want to thank Peggy Herman, Debra Race, and Belinda Blinkoff for their

administrative work. I want to thank Dr. Kathleen Gabrielson, Inez Vazquez, Nick Louloudis, Hugh Wall, Cynthia Maranto, Cynthia Schultz for their help and support on human and animal studies.

Furthermore, I would like to thank committee members of my dissertation defense, qualifying and oral exams, Dr. Jerry L. Prince, Dr. Jin U. Kang, Dr. Michael Schär, Dr. Benjamin Tsui, Dr. James C. Spall and Dr. Trac D. Tran. They not only set examples by being great researchers, but also benefit generations of students with their strict teaching.

Last but not least, I want to give my special thanks to my family. I want to thank my parents, who always trust me with their eternal love and support my life choices unconditionally. With my ultimate and sincere gratitude, I want to thank my dear wife, Runjia Zhao, who is also my best friend and life mentor. I would not be able to arrive where I am without her. She has accompanied me all the way through this many years and places, and has opened the window for me to all the good things that life has to offer. She celebrates with me in times of success and comforts me in those of adversity. During this journey, she shows such enormous courage, wisdom and tenacity of which she might not even be aware. I have been learning new things and thoughts from her every day, and I know that this will be a lifelong learning experience.

Table of Contents

List of Tables

List of Figures

Abbreviations

1.5T: 1.5 Tesla

2D: two-dimensional

3-SSIM: three-component weighted structural similarity index

3D: three-dimensional

3T: 3 Tesla

AE: autoencoder

AHA: American Heart Association

ANOVA: analysis of variance

AWG: American Wire Gauge

bFFE: balanced fast-field echo

BIR: B_1-independent rotation

BW: bandwidth

CEM_{43}: cumulative equivalent minutes at 43°C

CEST: chemical exchange saturation transfer

CNAWM: contralateral normal-appearing white matter

CT: computed tomography

DNN: deep neural network

dSRF: discrete spatial response function

EPI: echo planar imaging

ESP: echo spacing

EVLA: endovenous laser ablation

FA: flip angle

FBP: filtered back projection

FFE: fast field echo

FFT: fast Fourier transformation

FLAIR: fluid attenuated inversion recovery

FLASH: fast low-angle shot

FOV: field-of-view

FSSNet: feature-selective synthesizer neural network

FT: Fourier transform

fps: frames per second

FWHM: full width at half maximum

GRE: gradient-recalled echo sequences

GPU: graphics processor units

H&E: hematoxylin and eosin

HIFU: high-intensity focused ultrasound

iMRI: interventional magnetic resonance imaging

IMRUSA: intravascular MR ultrasound ablation

IQA: image quality assessment

IR: inversion recovery

IRE: irreversible electroporation

ISNR: intrinsic signal-to-noise ratio

IV: intravascular

IVC: inferior vena cava

IVHIFU: intravascular high-intensity focused ultrasound

IVMRI: intravascular magnetic resonance imaging

IVOCT: intravascular optical coherence tomography

IVUS: intravascular ultrasound

MESE: multi-echo spin echo

MI: mutual information

MMSE: minimum mean square error

MR: magnetic resonance

MRI: magnetic resonance imaging

MRS: magnetic resonance spectroscopy

MT: Masson's trichrome

MWA: microwave ablation

NLINV: nonlinear inversion algorithm

NMR: nuclear magnetic resonance

NN: nearest-neighbor

NSA: number of averages

OCT: optical coherence tomography

PC: personal computer

PCS: parameterized contrast synthesis

PD: proton density

PDT: photodynamic therapy

PE: phase encoding

PIN: positive intrinsic negative

PRF: proton resonance frequency

PRFS: proton resonance frequency shift

PTFE: polytetrafluoroethylene

PZT: lead zirconate titanate

OD: outer diameter

PCA: principal component analysis

qMRI: quantitative MRI

RF: radiofrequency

RFA: radiofrequency ablation

ROI: region of interest

SD: standard deviation

SENSE: sensitivity encoding

SG: slice gap

SL: slice thickness

SLAM: (spectroscopy with) linear algebraic modeling

SNR: signal-to-noise ratio

SRF: spatial response function

SSFP: steady-state free precession

SSIM: structural similarity index

SVD: singular value decomposition

T_1: spin-lattice relaxation time

T_2: spin-spin relaxation time

TE: echo time

TI: inversion delay time

TR: repetition of time

TSE: Turbo spin echo

UISNR: ultimate intrinsic signal-to-noise ratio

USA: United States of America

XTC: eXTernal Contro

Chapter 1: Introduction

1.1 Overview

Magnetic resonance imaging (MRI) is a noninvasive medical imaging modality that utilizes nuclear magnetic resonance (NMR) to generate images that can reveal underlying anatomy and physiological processes in the human body. MRI has been widely used in the clinic due to its lack of ionizing radiation and its capability for providing versatile contrasts based on differences in tissue NMR relaxation times which provide sensitivity to pathology; flow which provides sensitivity for angiography, perfusion, and diffusion imaging; and NMR phase and frequency information that enables MRI thermometry and spectroscopy. Recent advances in fast MRI techniques and minimally invasive surgeries have made interventional MRI (iMRI) techniques a possibility. Among these, intravascular MRI (IVMRI) is a specialized class of techniques that acquire MRI images directly from inside blood vessels to guide diagnostic or therapeutic procedures which can otherwise be difficult in terms of access, safety and precision. Recent years have seen an increased number of IVMRI studies and applications. Higher speed, finer resolution and more precise control, however, are still needed for IVMRI to advance into clinical use and provide value that can complement existing interventional radiology modalities. In order to explore the potential value of IVMRI in interventional settings, this dissertation explores aspects of IVMRI including system design, device fabrication, software implementation, real-time online computation and display, operation and protocol optimization, with an underlying rationale that iMRI will benefit from the optimization afforded by real-time feedback. This dissertation is organized as follows.

Chapter 1 gives an overview of the dissertation and describes basics of IVMRI.

Chapter 2 presents the development of a therapeutic device that can ablate pathological tissues that are proximal to, surround and/or potentially encroach on blood vessels. In these cases, it is important to achieve efficient ablation of the pathology without injuring the vessels providing access. Prior and current work has demonstrated that among various ablation modalities such as microwave ablation (MWA) and radiofrequency (RF) ablation (RFA), high-intensity focused ultrasound (HIFU) ablation is advantageous in providing precise control while minimizing injury at the tissue-device interface. After design iterations, we develop a novel IVMRI loopless antenna detector that was mated with a water-cooled IVHIFU ablation catheter to provide precision MRI-guided targeting, monitoring and thermal titration of perivascular ablation. Feasibility was demonstrated in *ex vivo* experiments. Progress at various stages have been published and presented at conferences in posters and oral presentations [1–4].

Chapter 3 further explores the performance of the combined IVMRI HIFU device with *ex vivo* and *in vivo* experiments. A protocol was developed to coordinate and streamline the steps of ablation, monitoring and titration of therapy. Software and algorithms dedicated for online processing of the signals being monitored, and the postprocessing of anatomy/thermometry/photography images are also described. Analysis of data from these experiments shows that the integrated system can consistently monitor the ablation status of ongoing procedures and deliver adequate ablation to a selected ablation targets under real-time guidance from online thermometry while affording protection of the vessel wall from thermal injury. Chapters 3 and 4 have been published in part as a journal paper [5].

Chapter 4 pushes the speed of high-resolution MRI endoscopy up to 10 fps to enable real-time endoscopy analagous to that of routine optical and intravascular ultrasound (IVUS) modalities. IVMRI endoscopes suitable for a clinical MRI scanner are developed and incorporated with a highly accelerated real-time MRI system. The real-time system is enabled by highly undersampled radial pulse sequences and corresponding temporally regularized iterative nonlinear inversion algorithm (NLINV) implemented on cascaded graphic processor units (GPUs) in a collaboration with researchers at the Max Planck Institute in Göttingen, Germany. In comparison with conventional MRI and regular real-time MRI systems, the incorporation of MRI endoscopy translates the previously fixed imaging reference frame to a mobile reference frame attached to the intravascular endoscope. This enables use of the interventional coil as a fully interactive endoscope, which makes it easily adoptable in intravascular imaging practices such as IVUS and optical coherence tomography (OCT). Algorithms for post-processing and analysis of IVMRI endoscopy images were also developed to reduce artefacts and/or evaluate performance in real time. This work at various stages was presented at conferences and published as a journal paper [6–8].

Chapter 5 presents work on using the minimal-acquisition, linear algebraic modeling (SLAM) method to dramatically accelerate MRI relaxation time mapping of compartmentalized targets. The author performed experiments and data processing as a secondary author to a colleague in the associated journal publication [9]. This work has been applied to IVMRI in other studies [10]. Moreover, the methodology of accelerated acquisition and reconstruction is connected to the work presented in Chapters 4 and 6, and opened the window for the author explore the topics in speed and contrast.

Chapter 6 proposes a novel and general framework for predicting MRI contrast over a range of acquisition parameters. The methodology is applicable for the (semi-)automatic tuning of image contrast to streamline not only IVMRI, but regular MRI as well, in demanding clinical environments. We for the first time proposed the objective and methods from a perspective of parameterized contrast synthesis (PCS). A protocol for running the scheme on an external computer was developed and implemented with a clinical MRI sequence using minimally invasive code. This design utilizes real-time interactive communication to analyze and optimize image contrast. Data analysis and strategy-prescriber subroutines are implemented as replaceable modules embedded in high-level programming language to enable fast-prototyping of application-specific algorithms for different applications. The sampling-and-prediction algorithm is framed as a feature selection problem, wherein baseline nearest-neighbor method, linear principal component analysis (PCA) method and deep neural network (DNN) method are used to learn contrast patterns from an MRI coil calibration dataset. The prediction performance of this learning process is evaluated with images acquired using standard MRI protocols. Progress on this project was been reported at a conference [11] and a journal paper is in preparation.

Chapter 7 concludes the dissertation, providing insights into the outcomes, their potential impact and directions for further work.

1.2 Magnetic Resonance Physics

1.2.1 Nuclear Magnetic Resonance

When an external constant magnetic field (B_0) is applied to nuclei with nonzero nuclear spin, the nuclei can absorb energy from an oscillating magnetic field (B_1) and

emit electromagnetic signals at a frequency proportional to B_0. This phenomenon is called nuclear magnetic resonance (NMR). NMR was first observed and explored by Nobel Laureates Isidor Rabi, Felix Bloch and Edwards Mills Purcell. Common isotopes that can exhibit NMR are ^{1}H, ^{13}C, ^{31}P, etc., and as ^{1}H (proton) is the most abundant in forms of H_2O, $-CH_2-$ and CH_3- in biological tissue, its signal is most widely used for medical imaging. The spin angular momentum S of these nuclei are associated with a magnetic dipole moment μ via the gyromagnetic ratio γ:

$$\mu = \gamma S \tag{1.1}$$

where γ is a characteristic property of the nucleus and for ^{1}H its value is $\frac{\gamma}{2\pi} = 42.58\ MHz \cdot T^{-1}$.

In bulk matter subject to a constant magnetic field B_0, the collection of magnetic dipole moments of magnitude μ in unit volume gives rise to a net nuclear magnetization M. Although NMR in essence is a quantum mechanical phenomenon, for the practical purpose of medical imaging with MRI, the bulk behavior of the magnetization in most NMR experiments can be described by classical physics. Similar to a gyro precessing in a gravitational field, the precession of magnetization M in a magnetic field B is given by the Bloch equation:

$$\frac{dM}{dt} = M \times \gamma B \tag{1.2}$$

The precession frequency solved from this equation is called the Larmor frequency:

$$\mathrm{f} = \frac{\gamma}{2\pi}\mathrm{B} \tag{1.3}$$

An oscillating magnetic field B_1 tuned to the Larmor frequency applied in the transverse direction of B_0 (traditionally chosen as the z-axis of a Cartesian coordinate

system) can excite the magnetization by inducing a torque that tips it into the transverse plane whereupon it precesses with a net traverse component M_{xy}. According to Faraday's law of induction, it is possible to detect a voltage signal induced by this precession in a detector coil sensitive to the x-y plane. This is the NMR signal. Energy exchange between the nuclear spins and their local environment, between the spins and their "lattice" and between spins and other spins cause the magnetization to return to an equilibrium state in B_0. This process is called relaxation, and its characteristic times are called the longitudinal or spin-lattice relaxation time T_1 and the transverse or spin-spin relaxation time T_2. The Bloch equation including this relaxation phenomenon is:

$$\frac{dM}{dt} = M \times \gamma B - \frac{M_{xy}}{T_2} - \frac{M_z - M_0}{T_1} \tag{1.4}$$

In practice, B_1 is applied with an oscillating frequency falling within radiofrequency range in a short period of time in the form of RF pulses for excitation.

1.2.2 Magnetic Resonance Imaging

Though NMR makes it possible to detect a signal proportional to the transverse magnetization in an excited sample, the signal is still not spatially differentiated and no imaging is afforded. Modern MRI uses spatially varying magnetic fields, denoted by a gradient field vector $\vec{G}$ to resolve signals from different locations. This technique was first used by Paul Lauterbur to generate the first NMR signal images in 1973 [12]. In 2003, Paul Lauterbur and Peter Mansfield shared the Nobel Prize in Physiology or Medicine for their "discoveries concerning magnetic resonance imaging". It should be noted that the purpose of the gradient field is to produce a spatial distribution of the Larmor frequency of the nuclear magnetization. For this purpose, the component of the

applied magnetic field gradient affecting the Larmor frequency is always that which aligns with the main magnetic field B_0 along the z-axis.

Consider a spatial distribution of the component $M_{xy}(\vec{r})$ of an excited sample, up to a multiplication factor. The bulk signal can be written as

$$\begin{aligned} s(t) &= \int M_{xy}(\vec{r}) e^{-j2\pi f(\vec{r})t}\, d\vec{r} \\ &= \int M_{xy}(\vec{r}) e^{-j2\pi \frac{B_0 + \vec{G}\cdot\vec{r}}{2\pi}\gamma t}\, d\vec{r} \\ &= \int M_{xy}(\vec{r}) e^{-j2\pi \frac{\gamma \vec{G} t}{2\pi}\cdot\vec{r}}\, d\vec{r} \cdot e^{-j2\pi f_0 t} \\ &= \mathcal{M}_{xy}(\vec{k}) e^{-j2\pi f_0 t} \end{aligned} \tag{1.5}$$

with

$$\vec{k} = \frac{\gamma \vec{G} t}{2\pi} \tag{1.6}$$

Here $\mathcal{M}_{xy}(\vec{k})$ is the spatial Fourier transform (FT) of $M_{xy}(\vec{r})$, and $\vec{k}$ is the spatial Fourier image space (k-space) coordinate. It can be appreciated from this relation that the introduction of gradient field $\vec{G}$ maps the image k-space magnetization distribution to the signal existing in time dimension. In other words, sampling the signal in time is equivalent to sampling the signal in k-space. With carefully designed gradient field schema, it is possible to sample the whole of k-space and acquire the corresponding image using inverse FT. As the gradient fields are typically applied within a limited period of time during which the NMR signal is evolving, they are also called gradient pulses.

1.2.3 Signal Acquisition and Reconstruction

Selective excitation

Although space information can be encoded by use of gradient fields, in most cases it is still needed to selectively excite portion of a sample to limit the amount of required encoding. This can be achieved by applying spatially-selective RF pulses which involves excitation in the presence of a gradient field. Frequency components of the RF pulse and the resonance frequency distribution encoded by the gradient field, collaboratively determine the excitation profile.

An ideal monochromatic RF pulse with unit amplitude at frequency f_0 is

$$B_1(t) = e^{j2\pi f_0 t}, \qquad -\infty < t < \infty \tag{1.7}$$

In practice, selective excitation is applied always within a limited time window and nearly always with amplitude modulation of the RF pulse which can be approximately modeled with a decaying envelope function $A(t)$. The modulated $B_1(t)$ and its FT are:

$$\begin{aligned} B_1(t) &= A(t)e^{j\omega_0 t} \\ \mathcal{F}\{B_1(t)\} &= \mathcal{F}\{A(t)\} * \mathcal{F}\{e^{j2\pi f_0 t}\} \\ &= A(f) * \delta(f - f_0) = A(f_0) \end{aligned} \tag{1.8}$$

where $\mathcal{F}(\cdot)$ denotes FT and $\omega_0 = 2\pi f_0$ is the angular frequency. Therefore, given gradient field amplitude and direction, the excitation location can be controlled by the oscillation frequency and the excitation profile can be determined by the envelope. A commonly used RF pulse envelope is a truncated SINC function for a rectangular slice excitation applied in the presence of a gradient pulse with a constant amplitude, as its Fourier transform is a RECT (square wave-like) function. For accurate implementation, the truncation of the SINC modulation must be compensated with corrective envelope

designs. Depending on the thickness of the selective excitation, there can be slice (2D or two-dimensional imaging) and slab (three dimensional, 3D imaging) or volumetric selective excitations.

Signal acquisition

Further considering Equations (1.5) and (1.6), one is certainly not bound to a constant gradient field $\vec{G}$ during the gradient pulses. Equation (1.6) can be re-written as:

$$\vec{k} = \frac{\gamma}{2\pi}\int_0^t \vec{G}(\tau)d\tau \tag{1.9}$$

In order to traverse the entire k-space, the gradient fields must be varied in direction and magnitude in various "k-space trajectories". This is commonly accomplished in a series of excitations in which the gradients are varied in one or more spatial dimensions, known as a "pulse sequence". For example, in the most commonly used method in today's clinical MRI called a Cartesian or "spin warp" imaging sequence [13], the magnetization is excited and the gradient fields applied to acquire a single k-space trajectory, with:

$$\begin{aligned} \mathrm{k_x} &= \frac{\gamma \mathrm{G_x t}}{2\pi} - \frac{\gamma \mathrm{G_x t_{RO}}}{4\pi}, t \in [0, t_{RO}] \\ k_y &= n_{PE}\frac{\gamma \Delta G_y t_y}{2\pi} = \frac{n_{PE}}{N_{PE}/2}\frac{\gamma G_y t_y}{2\pi}, n_{PE} \in [-N_{PE}/2, N_{PE}/2] \end{aligned} \tag{1.10}$$

Here $[0, t_{RO}]$ is the time window wherein the temporal signal is read out corresponding to a k-space trajectory, k_x, that encodes signal along the x-direction in each excitation in the form of a frequency distribution which forms a 1D projection. k_y is then changed between each acquisition step (numbered n_{PE}) for a total number of N_{PE} acquisitions by applying a gradient field pulse G_y before each readout window to encode a phase distribution along y direction. Here, the x-direction is called the readout (or frequency

encoding) direction; t_{RO} is called the readout time; the y-direction is called the phase-encoding direction; and N_{PE} is the number of phase-encoding steps.

Another common MRI method is projection reconstruction [12] or radial acquisition, because the method utilizes radial trajectories in k-space such as

$$k_x = \frac{\gamma G_x t}{2\pi} - \frac{\gamma G_x t_{RO}}{4\pi}, k_y = \frac{\gamma G_y t}{2\pi} - \frac{\gamma G_y t_{RO}}{4\pi}$$
$$G_x = G\,cos\,\theta\,, G_y = G\,sin\,\theta\,, t \in [0, t_{RO}] \tag{1.11}$$

Here each acquired radial trajectory is a slice in the 2D k-space, which after inverse FT again results in a 1D-projection of the signal distribution along the direction defined by θ, according to the projection-slice theorem. Acquisitions are then repeated with different values of θ to acquire N_θ such projections. The principle of this method is closely related to that of computed tomography (CT), which came earlier than MRI, and in fact, the first MRI images were indeed generated using the projection method [12].

Besides the two acquisition methods above, there are many other methods that extend or vary the basic Cartesian or radial methods of traversing k-space such as "zig-zag" echo-planar imaging and PROPELLER/BLADE, or even spiral trajectories [14–16].

Reconstruction

Reconstruction is performed to convert the raw signal samples into images. For Cartesian or other rectilinear acquisitions, raw data sampled from temporal signals corresponds to k-space data, and images can be reconstructed through multidimensional fast Fourier transformation (FFT), along with preprocessing and postprocessing steps.

For radial acquisitions, the non-uniformly sampled data points can be interpolated onto a uniform grid, after which FFT can be performed [17]. An alternative algorithm is filtered back projection (FBP), which is the *de facto* standard reconstruction method for

clinical CT. These two methods are closely related, and the density correction in radial acquisition gridding is similar to the ramp filter used in FBP [18]. The methods, however, differ in the space in which reconstruction is computed, resulting in performance differences when implementation [19]. The gridding method is also generalizable for use in all kinds of non-uniform acquisitions.

Acceleration is among the most important topics for MRI research. To this end, reconstruction methods are proposed for parallel imaging employing separate multi-coil detectors, and with signal undersampling. The basic representative examples of these techniques are SENSE and GRAPPA [20,21]. In order to resolve aliased signals resulted from undersampling, SENSE explicitly utilizes the nonuniform sensitivity maps of surface detector coils to replace low-order phase-encoding gradient steps by performing corrections in image space; on the other hand, GRAPPA estimates missing data directly in k-space using patterns learned from a fully-sampled autocalibration region. The relation between SENSE and GRAPPA are further explored from a point-of-view of subspace MRI methods, and the "ESPIRiT" method proposed to incorporate the advantages of both SENSE and GRAPPA [22]. Recent years have also seen trends in reconstruction being performed as a regression task that estimates target parameters by enforcing compliance between undersampled data and an *a priori* model, or a model learned from previous data. Examples include model-based reconstruction for quantitative MRI, "compressed sensing" and deep learning [23–26].

1.2.4 Sequences and Contrasts

Contrast in images come from the difference in signals from different locations. An attractive property of MRI is its versatility in that it can encode differences in M_{xy}

through distinct mechanisms to reveal underlying properties of biological tissues that are related to pathology or function. The most common properties appearing in contrast formulations are proton density (PD), T_1 and T_2, which determine the maximum magnetization and the characteristic times for the signal to decay. Today's MRI, however, has grown far beyond these properties, and has added capabilities of imaging functional, diffusional, temperature, physiological and chemical properties, etc. [27–30].

In order to create such contrasts and acquire such signals successfully, RF pulses and gradient pulses must be applied in a well-designed order, with the timing and amplitude of all the pulse sequence parameters under precise control. There is some common terminology that refers to the adjustable parameters of a pulse sequence, such as repetition of time (TR), which refers to the period between repeated excitations; echo time (TE) usually referring to the center of the readout window (which coincides with a "gradient echo") relative to the initial excitation time; and the flip angle (FA) which refers to the rotation angle through which B_1 tips the magnetization towards transverse plane during excitation. These terms, however, can have different meanings in more complex MRI sequences that are not fully described by a few parameters.

The resulting contrast is in general determined by the relevant underlying properties as well as the sequence parameters *in toto*. For example, the signal of a short-TR steady-state free precession (SSFP) sequence is given by [31]

$$\mathrm{s} = \mathrm{M}_0 \frac{1 - \mathrm{e}^{-\frac{\mathrm{TR}}{\mathrm{T}_1}} \sin(\mathrm{FA})}{1 - \mathrm{e}^{-\frac{\mathrm{TR}}{\mathrm{T}_1}} \mathrm{e}^{-\frac{\mathrm{TR}}{\mathrm{T}_2}} - \left(\mathrm{e}^{-\frac{\mathrm{TR}}{\mathrm{T}_1}} - \mathrm{e}^{-\frac{\mathrm{TR}}{\mathrm{T}_2}} \right) \cos(\mathrm{FA})} \tag{1.12}$$

where the equilibrium magnetization M_0 is proportional to PD.

1.2.5 MRI Thermometry

MRI thermometry describes a class of MRI methods that measures or maps temperature change or absolute temperature based on temperature-sensitive NMR properties of tissue. These properties include PD, magnetic transfer, T_1, T_2, the diffusion coefficient (D) and small shifts in the water proton resonance frequency (PRF). Of these, the PRF shift (PRFS) has proved the most useful in that it has good linearity over a thermal therapy-relevant range and because it is almost independent of tissue type [32–34]. Protons experience different local magnetic field due to the shielding effect electrons which is affected by temperature (T). Their resonance frequency can be written:

$$f = \frac{\gamma}{2\pi} B_0(1 - \alpha T) \tag{1.13}$$

where $\alpha \approx 0.01\ ppm \cdot ℃^{-1}$ is an electron screening constant. Considering the signal phase, $\phi = 2\pi f \cdot TE$, images acquired at different temperatures will have a phase change:

$$\Delta\phi = -\gamma B_0 \cdot TE \cdot \alpha \Delta T \tag{1.14}$$

To estimate temperature change in °C, a baseline image with known temperature is required, which is often obtained by measuring the body temperature simultaneously while acquiring a first image prior to any thermal intervention.

1.3 Intravascular Imaging

Coronary heart disease is a leading cause of death worldwide, caused by blood vessel stenosis usually due to plaque or thrombosis. The most common conventional imaging method to evaluate disease severity and to help with treatment is X-ray coronary angiography. Recent years have seen the development and increased usage of intravascular imaging in these tasks, because unlike X-ray angiography, IV imaging can

now visualize the vessel wall and critical plaques, instead of just inferring stenoses from areas of reduced intensity in contrast-enhanced images of the blood vasculature [35]. Common methods of IV imaging include IVUS and OCT. IVMRI, a subject of this thesis, has the potential for adding value to complement some of the limitations of IVUS and OCT.

1.3.1 Intravascular Ultrasound

The key component of ultrasound imaging is the transducer. A transducer transmits ultrasound waves by converting electric energy into mechanical energy, and it can also detect responsive ultrasound signals when serving as a receiver. In IVUS, the transducer is incorporated on an IV catheter, through which it can image its surroundings inside the blood vessel. Ultrasound imaging differentiates anatomical structures at different depths by measuring the delay in the reflected and refracted signal magnitude relative to the transmission pulse, and lateral structures are resolved as the user moves the transducer or the transmission beam is swept electronically. Due to the finite width of the sound wave pulse and diffraction effects on the beam emitted from transducer, IVUS has finite axial resolution (R_a) and lateral resolution (R_l) given by [36,37]:

$$\begin{aligned} \mathrm{R_a} &= \frac{\mathrm{c}}{2\mathrm{BW}} \\ R_l &= \lambda \frac{l_f}{A}, \text{at focal length} \end{aligned} \tag{1.15}$$

where c is the ultrasound wave speed, BW is the pulse bandwidth, λ is the ultrasound wavelength, l_f is the focal length and A is the transducer aperture size. At first glance it may seem that a shorter wavelength λ and pulse length can achieve a finer resolution, but reducing these adversely affects the BW and diffraction artefacts. Higher frequency also

decreases the penetration depth of ultrasound. Therefore, there are a lot of tradeoffs to consider to achieve the best performance. For modern IVUS transducers operating at frequencies of 20-50 MHz, the axial resolutions are about 70-200 μm, and the lateral resolution which is dependent on axial distance, is about 200-250 μm [37]. Artifacts often seen in IVUS arise from acoustic shadows from objects that are impenetrable to ultrasound, such as highly calcified lesions and the metal structures commonly used in interventions used for treating coronary artery disease.

1.3.2 Optical Coherence Tomography

Optical coherence tomography has similar imaging principles as IVUS, in that it illuminates near-infrared light on samples and measures the backscattered light to reconstruct the structural information at different depths. Compared to sound waves used in IVUS, light in OCT travels much faster, and the measurements are based on interferometry, where a low time-coherence source light is split into a reference beam and a sample beam, and an interferogram of the two beams is measured. In traditional time-domain OCT, a depth scan is performed in the reference arm to acquire an equivalent temporal signal. The interferogram has the form [38]

$$G(\tau) = 2\mathrm{Re}\{\Gamma_{\mathrm{source}}(\tau) * h(\tau)\} \tag{1.16}$$

where $\Gamma_{\mathrm{source}}(\tau)$ is the auto-correlation function of the source light which closely reflects the wavelength width of the source, and $h(\tau)$ is the backscattering profile from the sample corresponding to the depth information to be estimated. The depth scan used in time-domain OCT is often time-consuming as the speed is limited by a mechanical driver.

From another point-of-view, according to a first-order (Born) approximation, the scattered wave can be expressed as [38]:

$$V_S(r, k^{(s)}, t) = V^{(i)}(r, k^{(i)}, t) + \frac{1}{4\pi}\int_{sample} V^{(i)}(r', k^{(i)}, t) \cdot F_S(r', k) \cdot G_H(r, r') \cdot d^3r' \quad (1.17)$$

Here $V^{(i)}(r, k^{(i)}, t)$ is the incident wave function, $F_S(r, k)$ is the sample scattering potential, and $G_H(r, r') = exp(ik|r - r'|)/|r - r'|$ is a Green's function. Under the assumption that the scattered wave is measured at a distance much greater than the sample dimension, this equation can be re-written in the form an inverse FT, and considering only the depth direction z, we have the relation

$$F_S(z) \propto \mathcal{F}\{A_S(K)\} \quad (1.18)$$

where $A_S(K)$ is the complex amplitude of the backscattered field which depends on the backscattered wave vector, K, which is twice the incident wave vector. The spectrum $A_S(K)$ can be obtained by spectral interferometry, where the interferometer is equipped with a spectrometer that resolves the interferogram spectrally. Techniques for resolving depth information based on relation (1.18) are called "Fourier-domain OCT". These improve the imaging speed, largely by eliminating the need for a depth scan.

OCT has applications mainly in ophthalmology, dermatology and interventional cardiology. In all cases, other than for resolving the depth of structures, lateral scans are needed to form tomographic images. Intravascular OCT (IVOCT) is used to help diagnose and/or treat coronary heart disease, where the optical window is located on the side of an IV catheter tip that illuminates the surrounding vessel tissues. The lateral scan is performed by rotating the optics at the transducer tip to form cross sectional images of vessels. As can be appreciated from Equation (1.16), the depth resolution is dependent on

the light source bandwidth, which is typically ~10μm. Analogous to IVUS, the lateral resolution depends on the distance and beam characteristics, and are around 20-40 μm [39]. One drawback of OCT arises from the near-infrared light it uses, which has relatively poor penetration depths depending on tissue type (0.1-2 mm), and is completely attenuated by blood. As a result, blood has to be cleared out of the field-of-view (FOV) by occlusion and/or flushing. The development of Fourier-domain OCT with fast scan rates makes it possible to work with short-duration non-occluding flushing for *in vivo* studies.

1.3.3 Intravascular Magnetic Resonance Imaging

IVMRI uses miniaturized receiver or transmitter/receiver RF coils placed on IV catheters to perform imaging inside blood vessels. The basic imaging principles of IVMRI are the same as are applicable to conventional external MRI, discussed in Section 1.2 Magnetic Resonance Physics. The primary distinguishing feature of IVMRI is that due to proximity to the point of interest and the confined imaging region, a much higher signal-to-noise ratio (SNR) (up to 20-fold) and finer resolution (50-300 μm) than conventional MRI is achievable deep within the body [40–43].

In case of external coil, for a particular coil-sample geometry combination, the measured noise contributing to an SNR measurement is comprised of the coil noise and the sample noise, and the SNR dependence on B_0 can be qualitatively expressed as [44]

$$\psi = \frac{B_0^2}{\left(\alpha B_0^{1/2} + \beta B_0^2\right)^{1/2}} \tag{1.19}$$

where α and β represents factors associated with the coil size and the volume of the sample contributing the noise, respectively. While measures can be taken that render the

relative contribution of the coil noise negligible by eliminating electric (E) field losses, the sample noise is an inherent part of the biological system being studied. Therefore, the best SNR achievable for a given coil geometry, called the "intrinsic SNR" (ISNR), is the evaluated assuming zero coil noise, and is linearly dependent on B_0 for nearly all external whole volume (head, body, phased-array) MRI coil configurations [45]. The "ultimate intrinsic SNR" (UISNR) extends the concept of ISNR and considers the maximum possible SNR independent of coil geometry, and thereby provides a guidance for optimizing coil design [46,47].

Although both the ISNR and UISNR depend linearly on B_0 of external coils, the SNR of internal detectors like IVMRI coils has a fundamentally different B_0 dependence. There are various types of IVMRI coil designs, which can roughly be categorized into loop coils and loopless coils [40,41,48]. Theoretical and experimental investigations show, that for both types of coils, the absolute SNR ψ_s is given by [49]

$$\psi_s \propto \frac{B_0^2}{\sqrt{R_{\text{load}}}} \tag{1.20}$$

where R_{load} is the RF electrical resistance of the sample. The dominant noise comes from direct electric (E)-field losses involving coil-sample coupling, which cannot be eliminated through shielding or distributing coil tuning elements, as is in the case of external coils. Given that the direct E-field losses in the sample and the coil, being primarily dependent on the tissue's RF impedence, do not vary much with B_0, the realizable limiting SNR dependence on B_0 of internal coils is nearly quadratic. This results in a much greater advantage in SNR when IVMRI coils are used at higher magnetic fields, as evidenced by experimental studies [43,49].

Figure 1.1 shows examplary designs of loop and loopless IVMRI coils [50]. The detector in the loop coil is essentially an LC resonant circuit, while the loopless coil is a dipole antenna. Both coils/antennae need to be tuned to the NMR frequency in a lossy medium whose impedance properties are comparable to the sample, and connected to matching networks via tuned coaxial cables of odd multiples of the quarter-wavelength ($\lambda/4$) of the electromagnetic field in the media. It is worth noting that the coils can be used in transmitter/receiver mode and/or receiver-only mode, where, in the latter case, a conventional external transmit coil is used for excitation. In the latter case, a decoupling circuit including a diode switch is engaged to decouple the transmitter from the IV receiver coil during excitation to avoid excessive heating at the internal coil and to suppress induced currents which otherwise counteract the external field, according to Lenz's law.

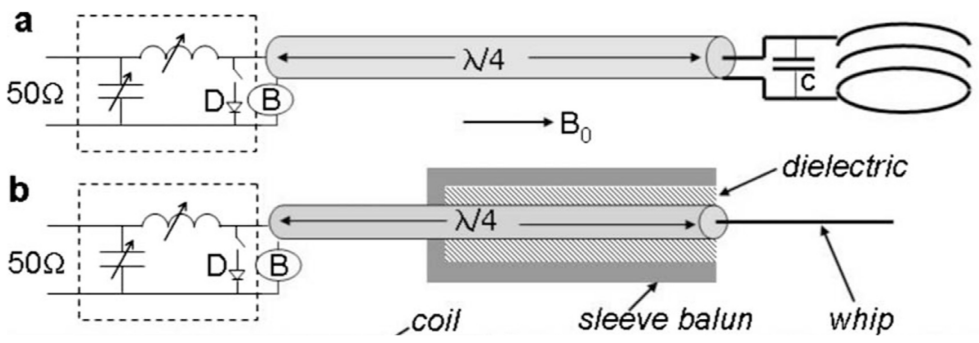

Figure 1.1: Illustration of IVMRI catheter loop coil (a) and loopless coil/antenna (b). D is the switchable diode and B denotes the cable trap balun connected to the cable shield. (Copyright 2009 Wiley. Used with permission from Sathyanarayana S, Bottomley PA. MRI endoscopy using intrinsically localized probes. Medical Physics 2009;36:908–19)

Recent years have seen developments in IVMRI to make it more amenable to clinical deployment. Loopless IVMRI technique has been integrated with RF ablation to deliver IV ablation under MRI guidance [51]. MRI endoscopy was proposed to increase

the speed of IVMRI further by transforming the imaging spatial reference system from the laboratory frame-of-reference to the detector frame-of-reference by eliminating slice selection steps, resulting in a more interactive procedure analogous to conventional endoscopy [42,50]. Further acceleration using compressed sensing has been explored [52]. Rapid and precise, quantitative IVMRI with automatic pathology characterization has also been studied using a combination of IVMRI with MRI relaxometry and with acceleration techniques such as spectroscopy with linear algebraic modeling also included in Chapter 5 of this thesis [9,10,53].

1.4 Ablation Therapy

Ablation is a therapy that deposits destructive energy targeted on pathological tissues such as tumors, dysfunctional myocardium and cerebral tissue and vascular malformations [54–56]. Based on the mechanism of destruction, ablation methods can generally be categorized as thermal and non-thermal.

Thermal ablations include methods that use heat or cold to ablate tissues. In most thermal methods such as RF ablation, microwave ablation, HIFU, and endovenous laser ablation (EVLA), energy in various forms such as electromagnetic and/or acoustic are deposited in tissue and converted into thermal energy via processes of absorption [56–59]. One exception is cryoablation, where tissue injuries are induced by rapid cooling (extraction of energy) via conduction with a cooling probe in contact with the targeted tissue [60].

For thermal heat ablation, there are different ways to titrate the heat exposure at the target to ensure tissue necrosis. One method is to set a critical threshold temperature to maintain for a certain time period [61]. A more comprehensive method is to integrate

the entire temperature history and calculate the cumulative equivalent minutes at 43°C (CEM_{43}) [62]

$$CEM_{43} = \sum_{0}^{t=final} R^{43-T}\,\Delta t \qquad (1.21)$$

$$R = \begin{cases} 0.25, T < 43℃ \\ 0.5, T \geq 43℃ \end{cases}$$

where T is the temperature at each time interval Δt. Previous studies have shown that a threshold of 340 CEM_{43} is widely accepted as the thermal dosage which delineates the boundary of thermal coagulation [34,63,64]. It has also been shown in these studies that MRI thermometry is a suitable method for titrating thermal dose in different tissue locations, by capturing a temporal series of high resolution spatial temperature maps.

Non-thermal ablations include: irreversible electroporation (IRE), where electrical fields are applied to irreversibly increase the permeability of cell membranes and induce apoptosis [65,66]; photodynamic therapy (PDT), where photosensitizers are administered to target locations and activated by light to cause fatally damage malignant tissues [67,68]; chemical ablation, wherein a cytotoxic agent is injected into tissues to induce necrosis [69]. Most of these methods carry risks of complications potentially severe, requiring the careful monitoring and titration of therapy delivery with consideration of the specific mechanisms of operation.

Chapter 2: IVMRI HIFU Ablation System Development

2.1 Introduction

The degree of involvement with adjacent blood vessels is often critical in determining whether a malignancy is surgically resectable. Pancreatic cancer, which has an incidence of 54,000 new cases and 43,000 deaths in the USA per year, is an example for tumor-vessel involvement [61,70–72]. Cancers with extensive tumor-vessel involvement and/or heterogeneous vessel contours around critical vessels like the superior mesenteric artery, are considered non-resectable and have very poor survival rates that are 3-10 times worse than those that are surgically resectable [70,73]. Hepatocellular cancer, with 42,000 new cases and 32,000 deaths annually is another example for tumor-vessel involvement. It has a high incidence of recurrence post-resection (~20%, ~50% and ~75% within 1, 3 and 5 years post-surgery respectively). In both examples, the need to preserve high-value tissue while carefully removing tumor at the margins are critical considerations [74,75]. For these and other pathologies, new methods of precision-guided therapy delivery could have a critical impact on reducing their terrible toll and improving patient outcomes.

Two common types of palliative or potentially curative treatments undergoing clinical trials are percutaneous ablation and extracorporeal HIFU [76–78]. Currently, percutaneous ablations include thermal ablation methods such as RFA, MWA, laser ablation and cryoablation; and non-thermal ablation such as IRE and PDT. These are nearly all performed percutaneously in the abdomen, and are prone to complications mentioned above, such as vascular damage, bowel perforation, fistulae, needle tract metastasis and organ dysfunction [73,79,80]. Extracorporeal HIFU is a non-invasive

alternative to percutaneous techniques which employs an array of external transducers that focus ultrasound energy on a target lesion, under the guidance of noninvasive magnetic resonance imaging. Yet significant challenges remain with HIFU due to the requirement of an ultrasound-transparent window between the HIFU transducers and the lesion, the complexity of tracking the precise motion of the treatment point under MRI, the obstruction or deflection of the incoming ultrasound fan-beam by air or bone, and the need to avoid injury to vital organs and vessels that lie in or near the beam's pathway [81–83].

MRI is arguably an ideal modality for guiding intervention because of its lack of ionizing radiation and its multi-functionality [84]. It offers angiographic-, perfusion-, diffusion-, soft-tissue relaxometry-, pathology- and therapy-sensitive contrast, as well as quantitative thermometry for titrating thermal therapies such as those using HIFU, for example [85–87]. IVMRI employing small internal detectors configured as catheters or guidewires can provide higher resolution (<100 μm) and SNR than regular MRI in clinical scanners [49,50]. They potentially offer a precise, minimally-invasive, diagnostic [10,88] and interventional imaging modality, at least within a range of a few centimeters from the probe. RFA employing a single IVMRI probe for image guidance, energy delivery and thermometry for monitoring dose, has been demonstrated in tissue specimens and *in vivo* in a clinical 3 Tesla (T) MRI scanner [51]. However, the RFA lesions produced this way are limited primarily to the point of contact of the MRI-sensitive portion of the catheter with the tissue, causing injury to the vessel wall in IV applications.

Like IV RFA, HIFU ablations can also be delivered via small ultrasound transducers [89,90]. Unlike extracorporeal HIFU methods, a local IVHIFU approach could avoid much of the difficulty with finding suitable acoustic windows. It could potentially enable the delivery of therapy from inside a nearby blood vessel to a perivascular target, without damaging the intervening vessel wall [91,92]. While IV HIFU's sister technology, IVUS, could be used to guide IV ablations, IVUS currently requires X-ray guidance for deployment and does not provide reliable thermometry. Without precision guidance and thermometry, it would be unable to precisely ablate a margin of tumor around a major vessel while safely preserving the vessel wall itself.

Here we present a novel IVMRI loopless antenna detector combined with a water-cooled IVHIFU ablation catheter to provide precision MRI-guided targeting, monitoring and thermal titration of perivascular ablation.

2.2 Methods

2.2.1 Feasibility Test of IV Ultrasound Ablation

To evaluate the ablation performance of an ultrasound transducer and its effect on imaging signals, a ~60 cm long ultrasound transducer catheter with a 1 mm diameter guidewire lumen was fabricated from polyimide tubing, and integrated with a tubular ultrasound transducer (modified PZT; 2.5 mm OD, 2.2 mm long; 4.66 MHz drive frequency). Ablation power was supplied by a pair of 28 AWG magnet wires, intermittently co-wound on the catheter tubing to form three 3-cm long chokes to suppress the MRI (B_1) transmit RF field. The entire assembly was encapsulated in watertight polyester heat shrink tubing. MRI was provided via a loopless antenna (0.8 mm diameter) mounted on the catheter (Figure 2.1).

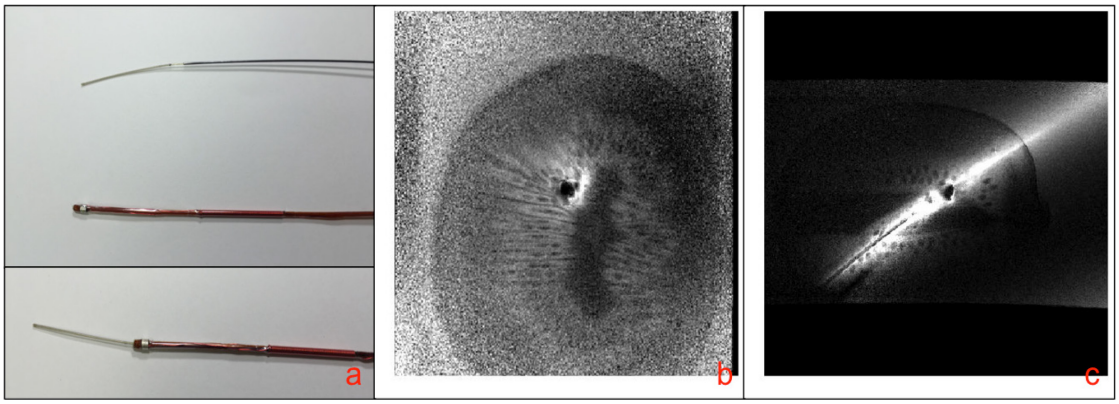

Figure 2.1 (a) IVHIFU transducer and MRI loop-less antenna, (b) Axial MRI of a Kiwi fruit (TSE, 0.2x0.2x4mm^3) (c) The transducer appears as a signal void at center of the hyper-intense region.

MRI studies utilized a Philips 3T scanner equipped with Sonalleve™ thermometry. Performance was first evaluated in a kiwi fruit in a saline phantom (TSE sequence, resolution: 200 µm). Real-time ablation and thermometry was then monitored in a chicken breast immersed in saline using an fast field-echo (FFE) and echo planar imaging (EPI) sequences. Ablated tissue was examined by gross histology and compared to intraoperative MRI thermometry maps.

2.2.2 Iterated Designs of IVMRI HIFU Devices

All MRI studies were performed on a *Philips Achieva* (*Koninklijke Philips N.V.*, Amsterdam, Netherlands) 3T scanner with an in-room image monitor for interventional studies. The scanner was used previously [10,49–51,88]. MRI HIFU ablation catheters were comprised of a loopless IVMRI antenna formed from an 0.8 mm OD, 0.88 m long, biocompatible nitinol coaxial cable with a 42 mm whip tuned to resonate at 128 MHz in a lossy medium (0.35% saline). The antenna was deployed as a receiver coil which was turned-off during excitation via a positive-intrinsic-negative (PIN)-diode in its matching circuit(Figure 1.1; [49,50]). Operated alone, the antenna was tested *in vitro* and *in vivo* on

this system, wherein heating on the wire and cable was kept within ~1 °C during MRI [49,50]. Maximum heating and MRI sensitivity occurred at the cable-whip junction.

The antenna was incorporated into intravascular HIFU ablation catheters fabricated with three different geometries affording single- or dual-beam ablation patterns with properties summarized in Table 2.1 and pictured in Figure 2.2(c, d, e). The antenna's cable-whip junction was aligned in the axial plane orthogonal to the catheter's long axis through the center of the HIFU transducer(s) to provide maximum MRI sensitivity in the ablation plane. The transducer(s) in each catheter were encapsulated in a non-conducting biocompatible polymer jacket. The jacket was water-cooled at a 20-50 ml/min flow-rate via a computer-controlled *Acoustic MedSystems Inc.* (Savoy, Illinois, USA) *TheraVision* pump with an off-the-shelf closed-loop water chiller, located in the MRI console room. The coolant protected the transducers from overheating and also cooled the IVMRI antenna as well as the tissue immediately adjacent to the jacket. The IVMRI antenna was externally affixed to HIFU catheters #1 and #2 (Figure 2.2a) via paper tape to facilitate interchange of probes during development and testing. It should be emphasized that taping was a temporary measure instituted to allow testing of the HIFU probe and to ascertain its compatibility with MRI when in close proximity to the IVMRI antenna. This avoided a permanent fixation that would impair further use of the devices in the event of an unsuccessful outcome. The heating profile and focus size of catheter #1 is shown in Figure 2.3. Catheters #2 and #3 have diverging radiation profiles (Table 2.1). HIFU catheter #3 was fabricated with a 1.45 mm OD central lumen to accommodate a guidewire through which the loopless antenna was inserted for IVMRI (Figure 2.2).

During ablation, the transducers were driven by a 4-channel 6-14 W RF amplifier also controlled by the *TheraVision* unit. A schematic of the combined HIFU/MRI catheters and their connections is presented in Figure 2.4. The RF coupling between the IVMRI antenna and each HIFU catheter #1-3 was documented with S-parameter measurements of the power transfer parameter (S21).

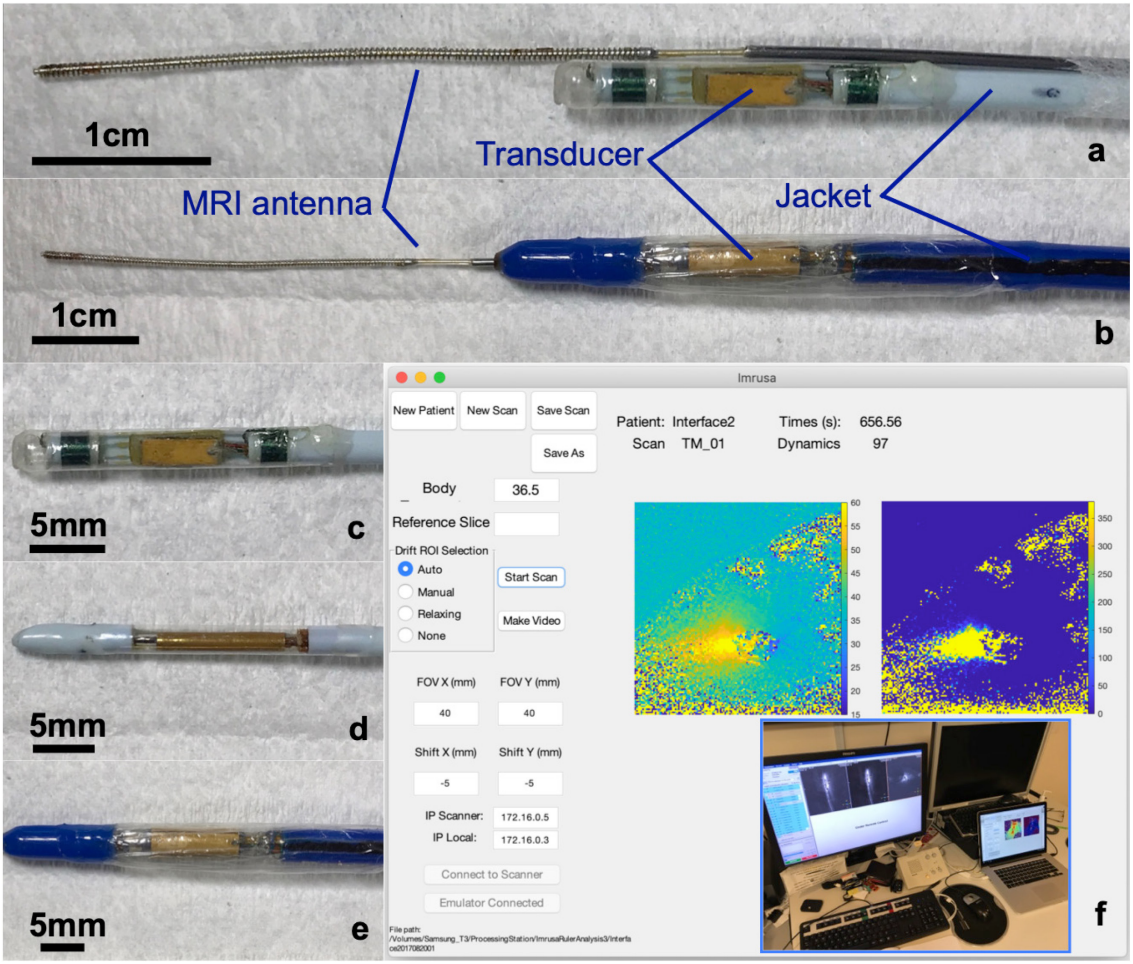

Figure 2.2 Combined IVMRI and IVHIFU ablation catheters (a-e) and the software interface (f). In initial studies, the IVMRI antenna was taped (not shown) to the HIFU transducer (a). Subsequent IVHIFU catheters incorporate a lumen to take an X-ray guidewire or the MRI antenna (b). Catheter denoted #1, #2 and #3 from Table 2.1 are pictured in (c)-(e). A screen-shot of the MATLAB-based real-time thermal monitoring software interface installed on a personal computer (PC), is shown in (f). The monitor is connected to the scanner console computer via an ethernet cable. Inset (bottom right) shows an experiment with data transfer between the scanner console and the PC.

Table 2.1 Specifications of intravascular ultrasound ablation catheters developed for this study.

Name	OD (mm)	Transducer shape	Number of channels	Ablation angle	Operating frequency (kHz)
Catheter 1	2.5	5.5 mm Flat	1	60°	6260
Catheter 2	2.4	10.4 mm Hoop	1	360°	7347
Catheter 3	4.3	10.0 mm Sector	2	†90°/90°	†6473/6818

† Values for channel 1 and channel 2, respectively.

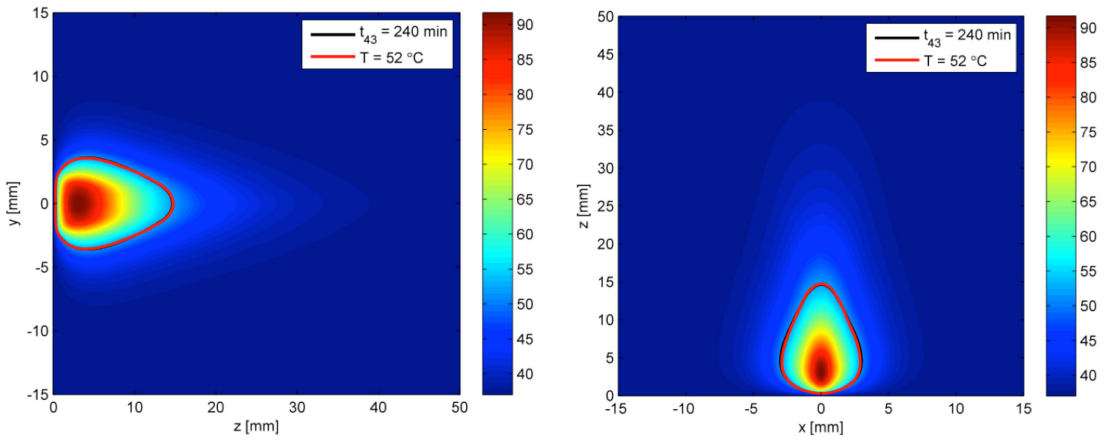

Figure 2.3 Heating profile (simulated) for the flat HIFU transducer used in catheter #1 in muscle tissue after a 60 s ablation at an input power of 15 W/cm^2 at 5 MHz in y-z (left) and x-z (right) Cartesian planes (x is tangential, y is axial and z is perpendicular to the flat plane of the transducer). The natural focus distance, defined as the distance between the hottest spot and the transducer, is 3.4 mm. Full-width half-maximum (FWHM) focus sizes are 3.0 mm, 5.0 mm, and 8.3 mm in tangential, axial and radial directions, respectively. Vertical scale is in °C, with 37 °C as baseline.

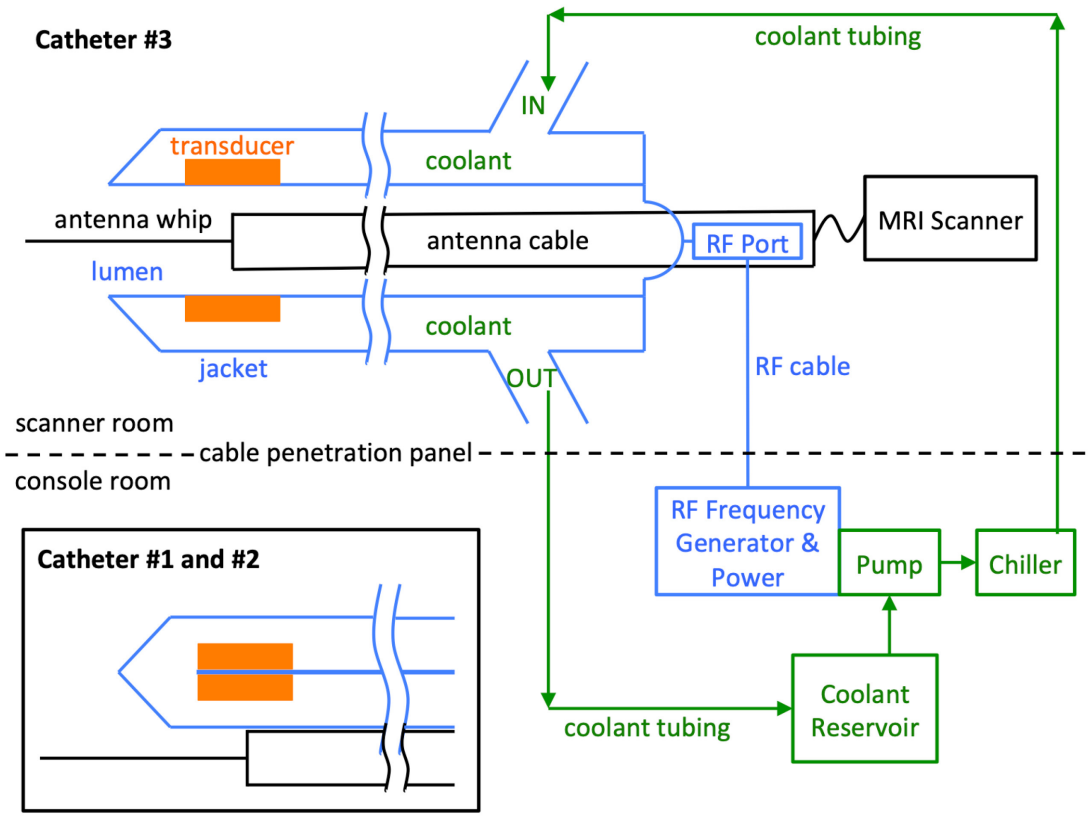

Figure 2.4 Schematic diagram of catheter #3 catheter (top) and catheter's #1 and #2 (bottom left, inset). The MRI system (black), the HIFU RF system (blue) and the cooling system (green) are plotted in different colors. Component sizes are not to scale.

2.2.3 Thermometry

MRI thermometry was performed using the PRFS method and FFE imaging sequences. In initial experiments, FFE magnitude and phase images for each scan were transferred in real-time to a local computer equipped with modified *Sonalleve*™ (*Profound Medical Corp.*, Mississauga, ON, Canada) software for temperature display [93]. The product *Sonalleve* software operates with a transducer array embedded in a patient table that was not used here. Thus the software's focus-planning component was modified to enable selection of the catheter location relative to anatomical MRI scans [93] and the array-based adjustments eliminated. Subsequently, a dedicated

MATLAB (*The MathWorks, Inc.*, Natick, MA, USA) IVMRI ultrasound ablation software interface IMRUSA (Intravascular MR Ultrasound Ablation) (Figure 2.2f) was developed by the author for real-time temperature mapping and measuring thermal dose. This software incorporates drift corrections and accommodates the non-uniform sensitivity profile of the IVMRI antenna. It runs on a laptop connected to the MRI system's console computer via an ethernet cable (Figure 2.2f; inset), through which data is transferred via *MATLAB MatMRI* [94] software based on an 'eXTernal Control' (XTC) protocol [95].

Phase-difference images were computed from dynamically-acquired FFE phase images and converted to temperature maps with a PRFS coefficient $\alpha = -0.0094$ ppm/℃ (see Eq. [1.13]). The temperature of unablated tissue measured with a remote fiber-optic temperature probe (*Neoptix Canada LP, Qualitrol Company LLC,* Fairport, NY, USA) was assumed as a baseline temperature reference. The *MATLAB* software automatically detected the catheter location from the IVMRI antenna's non-uniform sensitivity profile, and selected regions ≥ 5 cm from the transducer to serve as constant-temperature reference points on the thermal maps. These were used to provide a first-order temperature drift correction. During ablation, pre-ablation cooling, and post-ablation cool-down periods, the operating parameters (ablation time, flow rate, power level) of the *TheraVision* system were manually adjusted to achieve the desired heating and cooling based on the real-time MRI thermometry monitor.

Post-ablation, thermal dose maps–measured in cumulative equivalent minutes at 43 °C ('CEM_{43}')–were derived by temporally integrating the dynamic real-time temperature maps [62,96] after de-noising and co-registering them with anatomical images. A CEM_{43} of 340 has previously been assumed as a threshold for producing

necrosis [51,63,64], so MRI-based lesion-dose-threshold CEM_{43}=340 contours were calculated, smoothed to generate continuous loops, and overlaid on co-registered photographs of lesions. The areas of the continuous CEM_{43}=340 loops were measured and tested as a potential IVMRI proxy indicator of lesion size.

2.2.4 *Ex Vivo* Evaluation

Bench-top and in-scanner *ex vivo* studies of tissue specimens were used to characterize system performance. The efficacy of the probe cooling and ablation sub-systems were first evaluated in bench-top ablation experiments on chicken breast muscle. The chicken was immersed in saline at 37 °C, and an IVHIFU catheter inserted. Coolant flow, temperature, IVHIFU power level and duration were adjusted to determine a range of suitable operating parameters for subsequent in-scanner studies. After bench-top ablation, the tissue was sectioned axially at the ultrasound transducer location, and thermal lesions photographed. In-scanner studies were performed on chicken breast tissue as above, and with IVMRI HIFU catheters inserted in the blood vessels of fresh porcine liver specimens. Specimens were immersed in 35 °C saline (0.35%) for ablation. MRI was performed (using 3D balanced fast-field echo, bFFE; TR/TE=6.1/2.3 ms; resolution =300 μm; FOV=150x150x12 mm^3; FA=20°), followed by ultrasound ablation (6 min @ 7 $W_{acoustic}$) during which the catheter was water-cooled (water temperature=22 °C). During ablation, MR thermometry (EPI PRFS imaging; TR/TE =28/16 ms, 0.9x0.9x6 mm^3, 1.2 s/frame) was performed in real-time to monitor temperature change and thermal dose. The ablation was terminated upon achieving a ~1 cm ablation lesion. Lesions were identified by gross anatomy post-MRI, and

correlated with thermal dose as identified by the CEM_{43} contour measured by MR thermometry.

2.3 Results

2.3.1 Feasibility Test of IV Ultrasound Ablation

The ultrasound transducer catheter was tracked as a signal void at the center of the hyper-intense antenna MRI signal (Figure 2.1c), and provided high-resolution imaging in the region adjacent to the transducer (Figure 2.1bc). Real-time MRI thermometry indicated a maximum temperature of ~70 °C during ultrasound ablation, consistent with bench-top testing using fibre optic thermal sensors (Figure 2.5). An approximately 8-9 mm diameter sphere of tissue surrounding the transducer was heated ≥60 °C (Figure 2.5b) based on the MRI thermometry, which matched the 9 mm diameter lesion evident at gross histology (Figure 2.5a).

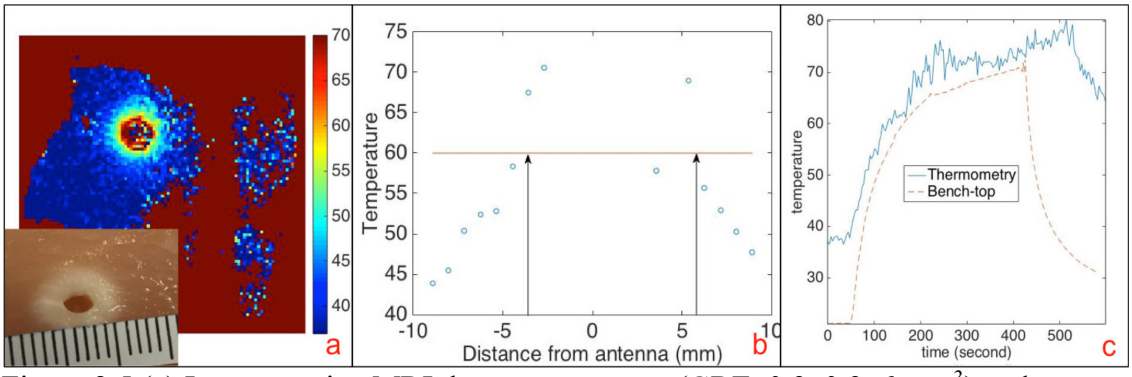

Figure 2.5 (a) Intraoperative MRI thermometry map (GRE, 0.9x0.9x6 mm^3) and gross histology (below, inset), (b) Temperature distribution vs. distance from catheter. Arrows denote tissue region heated ≥60 °C (c) Temperature monitored by MRI thermometry (blue curve) and by fibre-optic sensor (red curve).

2.3.2 Iterated Designs of IVMRI HIFU Devices

The S21 parameters for the IVMRI antenna combined with each of the three catheters from 0.1 MHz to 150 MHz were -70 dB to -25 dB. Bench testing in chicken,

indicated that key factors that improved the preservation of (unablated) tissue immediately adjacent to the IVHIFU catheter were: reducing the temperature of the coolant; and increasing the flow to the catheter. Other factors were: the thermal energy delivered by the ablation transducers, as monitored by MRI thermometry; and transducer geometry. A coolant temperature of 3-4 °C at the pump output and 10-13 °C where it entered the catheter, a flow of ~30 ml/min and a HIFU power ~7 W for ~6 min were found to produce thermal lesions of up to 2 cm^2 while preserving a 1-2 mm margin of tissue abutting the catheter. Parallel to the catheter, the maximum extent of the lesion corresponded to the transducer length (listed in Table 2.1).

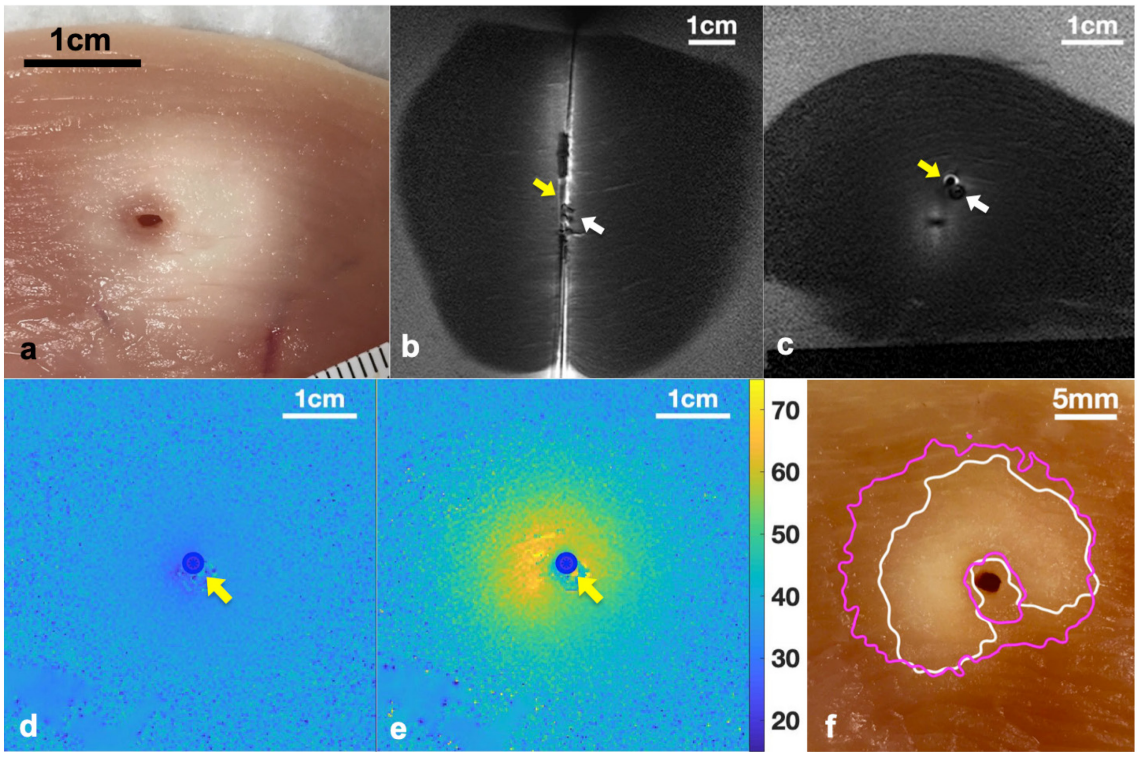

Figure 2.6 Photo of a section of chicken breast tissue in the ablation plane following bench-testing with catheter #2 (a). A preserved tissue margin (pink) surrounds the probe location, inside the ablation lesion (white). The IVHIFU catheter ablation transducer (yellow arrows) and IVMRI loopless atenna whip junction (white arrows) are seen in orthogonal high-resolution IVMRI planes (b,c). Screen shots of online thermometry (scale in °C at right) during pre-ablation catheter cooling (d) and ablation (e) are shown. The catheter position is denoted by blue circles (yellow arrows). Part (f) is a photo annotated with contours of the 86% lethal thermal dose of CEM43=340 as determined by MRI thermometry (magenta) and with a contour (white) enclosing the lesion (bleached).

2.3.3 Thermometry and *Ex Vivo* Evaluation

Exemplary results from chicken are shown in Figure 2.6, where an inner margin of pink preserved tissue at the catheter location is surrounded by a pallid ablation lesion (Figure 2.6a). On MRI, the IVMRI HIFU catheter is easily located via the bright sensitivity of the antenna and signal void at the conductors (Figure 2.6b,c). During pre-ablation cooling, real-time temperature maps reconstructed from dynamic MRI phase images show local temperature decreases ≤10 °C (Figure 2.6d). During ablation, increases of ≤70 °C are evident 3-5 mm away from the catheter (Figure 2.6e), with no

evidence of heating adjacent to the IVMRI probe itself. The MRI thermometry-based CEM_{43}=340 contour co-registered onto a photograph of the section (Figure 2.6f), showed fair consistency with the lesion contour determined by tracing the midpoint in intensity and hue between pixels in ablated tissue (pallid) and those in preserved tissue (crimson; see next chapter).

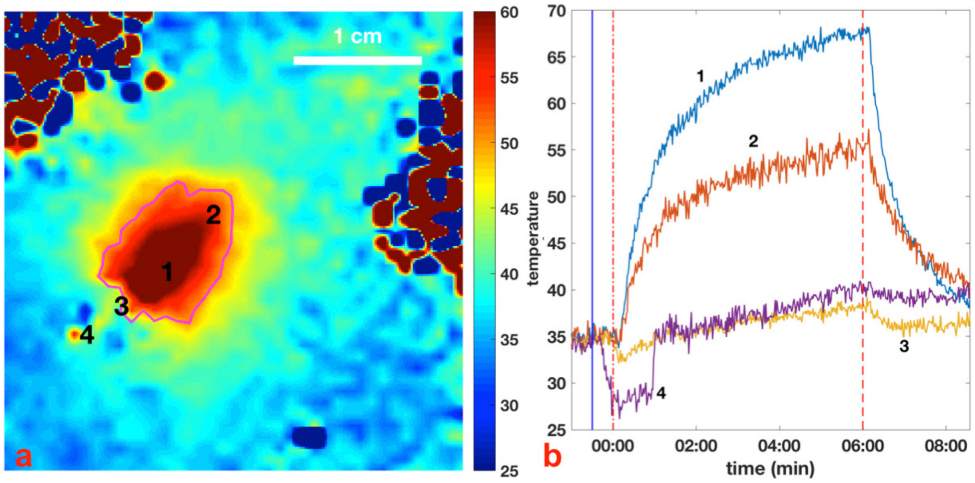

Figure 2.7 (a) MRI thermal map near the end of a 6-min ablation. Four ROIs are marked for temperature behavior analysis: ROI1, ablation focus; ROI2, distant edge; ROI3: edge in the middle; ROI4: transducer location. The magenta line denotes the coagulation thermal dose contour (equivalent to 240 min at 43°C). (b) Temperature changes of ROIs in (a): ROI1 and ROI2 are ablative > 240 Thermal Equivalent Minutes @43 °C. ROI3 and ROI4 are <40 °C. Vertical lines indicate: circulation cooling start (blue solid, -30 s), ablation start (red dashed dot, 0 s), and ablation end (red dashed, 6 min).

Figure 2.7a shows an MRI thermal map acquired at the end of a 6-min ablation with four ROIs annotated, and a photograph of the corresponding anatomical section shows the lesion (Figure 2.8b; magenta circle). Temperature changes during the whole process of treatment are shown in Figure 2.7b. Temperatures in the target ROIs away from the vessel and probe, increase monotonically during ablation up to 67 °C. Meanwhile, temperatures closest to the vessel are relatively constant or initially decrease upon commencement of circulation of the cooling water, and remain <40 °C for the entire

procedure. Contours for a thermal dose equivalent to 240 min at 43 °C (an alternative threshold for coagulation [96]), as calculated from the thermal maps, are also plotted in Figure 2.7a and Figure 2.8b (magenta circle). The thermal dose vs. distance along the axis of peak energy delivery (perpendicular to the transducer's long axis), is plotted in Figure 2.8a. The 240-min-43°C threshold exhibits a 4.6-mm-wide non-coagulation area outside of the transducer, wherein vessel wall is expected to be spared during ablation.

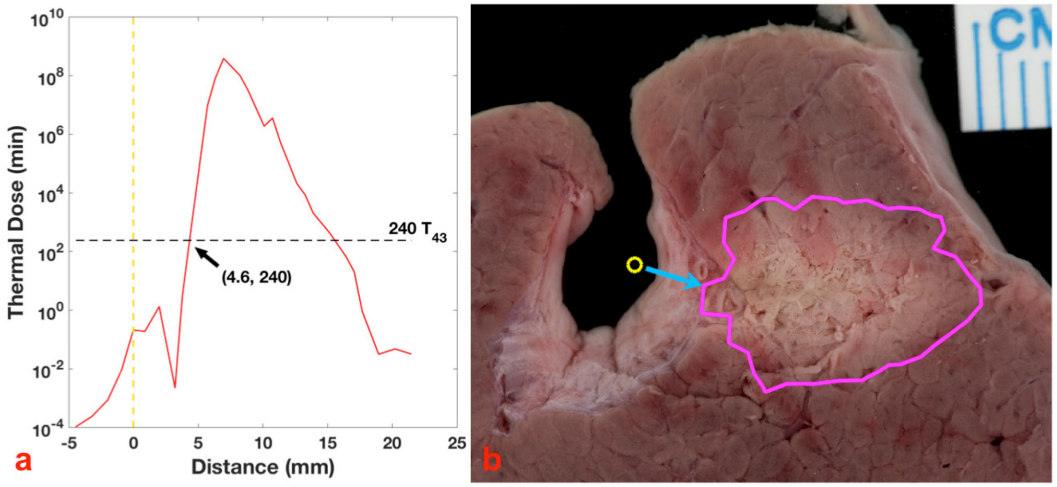

Figure 2.8 (a) Thermal dose vs. distance to the transducer along the main ablation axis (perpendicular to the device cable, position indicated as vertical yellow dashed line). The 240-min equivalent 43 °C ablation threshold is marked (horizontal dashed line), and 4.6 mm no-coagulation gap identified. (b) MRI thermometry-based coagulation contour matched the gross histological lesion. The pale tissue between the lesion and the yellow circle (catheter access) is the vessel wall.

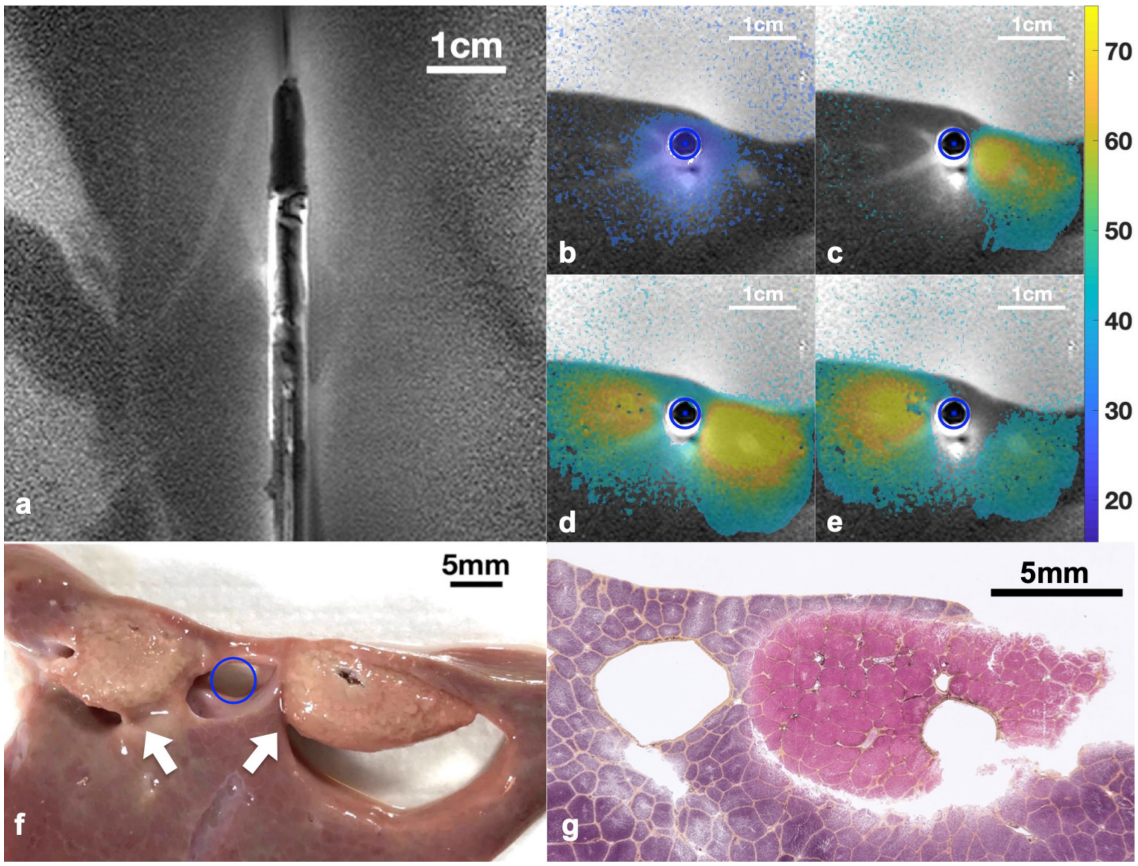

Figure 2.9 IVMRI of catheter #3 with thru-lumen design (from Figure 2.2b) in a porcine liver (a). IVMRI thermometry (scale, °C at right) shows pre-cooling (b); ablation in one direction (c); simultaneous ablation in two directions with both transducers turned-on (d) and after turning one transducer off (e; blue circle denotes catheter position). Part (f) is a photo of the dissected transverse section through the ablation showing a lesion in each direction which has detached from the non-ablated tissue (white arrows; blue circle denotes the vessel hosting the catheter). Part (g) shows the Movat-stained histology indicating a margin of preserved tissue between the vessel wall and lesion.

Incorporating the IVMRI antenna into a lumen–as in HIFU catheter #3 (Figure 2.2b)–improved the visibility of the catheter components in porcine liver (Figure 2.9a). The transducer elements do not interfere with the performance of the IVMRI antenna, suggesting negligible coupling. The inclusion of two transducer elements provided simultaneous and/or sequential thermal beams that heated in opposite

directions (Figure 2.9b-e). Movat-stained histology shows preservation of a non-ablated tissue margin between the vessel wall and lesion (Figure 2.9g).

2.4 Discussion

This chapter discusses the development and iteration of designs for a combined IVMRI and IVHIFU catheter for performing and monitoring perivascular ablation. The selection of IVHIFU as the ablation method over a prior multifunctional RFA approach [51] was purposeful. RFA, while easy to power from the same (shared) IVMRI probe, has a heating profile subject to its relatively long wavelength, that is difficult to focus other than by structure changes, as exemplified in Figure 2.10. In particular, the thermal energy is primarily deposited at the point of contact, which in IV applications, risks extensive vessel wall damage when engaging extra-vascular ablation targets. In contrast, high intensity ultrasound has shorter wavelength at working frequency (~0.25 mm at 6 MHz) and a better localized heating profile (Figure 2.3). The usage of multiple HIFU transducers provides the capability of re-orientating the ablation target (Figure 2.9) and has the potential to be programmed as an array to provide better focalization.

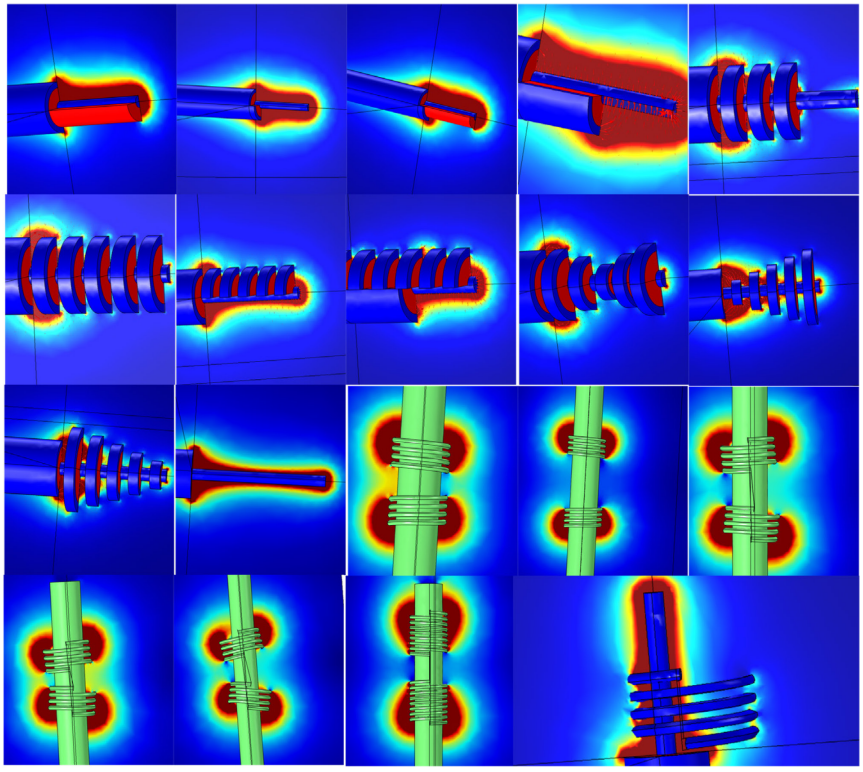

Figure 2.10 RFA heating profiles simulated by finite element analysis (*COMSOL Multiphysics*, *COMSOL AB*, Stockholm, Sweden) for different structures of ablation antenna. The loopless antenna are made from coaxial cables comprised of copper inner and outer conductor (blue) and polytetrafluoroethylene (PTFE) dielectric (red). The opposed-direction solenoid coils (thin green wire) are wired around plastic tubes (green cylinder). It can be seen that local changes such as making the structure asymmetrical and/or periodical hardly affect the field distribution whose wavelength is much larger than the scale of the device.

The ablation feasibility test catheter (Figure 2.1) enabled anatomical MRI and thermometry combined with local HIFU ablation, simultaneously. Although it required two sets of electrical connecting leads, MRI coupling was not a problem due to the large difference in operating frequencies and the use of multiple isolation chokes on the HIFU ablation leads. Note that drift in the MRI thermometry in these experiments necessitated correction. Even so, the local temperatures measured by MRI thermometry and fibre optic thermal probes recorded during steady-state, were in close agreement (Figure 2.5c).

The thru-lumen design of the integrated IVMRI HIFU catheter not only improves image quality (Figure 2.9), but also facilitates interventional procedures allowing, for example, an X-ray guidewire to be easily interchanged with the IVMRI antenna. Catheter #1 and catheter #2 were affixed with loopless MRI antenna through taping (as in Figure 2.1) as a temporary measure during the iterated design of IVMRI HIFU catheters. It allows feasibility testing of ablation capability and MRI compatibility of the HIFU catheter without a permanent fixation that would affect fast replacement of the devices for upgrading or repairment. Gluing or mechanically attaching the HIFU and IVMRI antenna would certainly provide more robust mounting options than the taping used for catheter #1 and #2.

Beyond the feasibility of IVMRI HIFU ablation demonstrated in this chapter, it is yet unclear what is the performance of the system through scalable experiments *ex vivo* and *in vivo*. In the next chapter, we will show systematic testing results that better characterizes the system under more practical conditions, which are enabled by carefully orchestrated workflow and detailed quantitative image/data analysis.

Chapter 3: Performance and In Vivo Testing of High-resolution IVMRI HIFU System

3.1 Introduction

In the previous chapter, we have described the development process of IVMRI HIFU system and have shown the preliminary performance of the system in *ex vivo* ablation. To better understand performance of the system in more practical scenarios, it is helpful to document comprehensive results from repeatable experiments. To achieve this, however, there are still difficulties to overcome. First, it is a demanding task to drive the multi-component system consisting of imaging/thermometry/ablation modules as each module has its own required procedure and configuration to work while all modules have to coordinate with each other at the same time. The complex steps can easily keep operators busy to an overwhelming extent, cause miscommunication among the operating team and make the experiments prone to error. It is even more challenging during *in vivo* experiments than during *ex vivo* ones, as there are often more limitations on timing, resources and error-tolerant rate. Second, there is no protocol for IVMRI HIFU performed *in vivo*. It is an open question how to demonstrate orientation and titration of ablation with such device with unknown impact from blood flow and motion. Third, the results of ablation experiments are presented with multiple forms of data, such as MRI thermometry and histological photography. For repeated experiments, it is important to align and compare lesion sizes measured from different modalities with consistent quantitative methods.

In this chapter, we have addressed the above issues to carry out systematic evaluation of performance of IVMRI HIFU ablation in *ex vivo* and *in vivo* studies. We lay

out the procedures that are required to drive the multiple systems, at the core of which is the IMRUSA software we developed in 2.2.3 Thermometry. The software helps us automate part of onsite analysis tasks and works as a central console of information, which enables us to repeat experiments reliably. Post ablation, image processing techniques are applied to fuse different modalities of images and measure lesion sizes for comparison. Two *in vivo* ablation studies are carried out in the inferior vena cava (IVC) of pigs using the surrounding psoas muscle as the target. It is demonstrated that IVMRI HIFU ablation can be applied with high successful rate in multiple *ex vivo* and *in vivo* studies. The actual thermal lesion region can be accurately predicted from monitoring MRI thermometry, and despite the existence of blood flow, adequate ablation can be achieved *in vivo* with the thermometry guide.

3.2 Methods

3.2.1 Summary of Workflow

A summary of the treatment/monitoring protocol is given in the Figure 3.1. Localization procedures and reference measurement procedures start from separate start points “select treatment spot” and “select baseline spot”, respectively. The step “*Select ablation power and coolant flow rate*” is performed via the *TheraVision* unit described in 2.2.2 Iterated Designs of IVMRI HIFU Devices. The two procedures merge together after thermometry imaging is initiated at “start FFE imaging”, starting from which the software combines data being collected and guides adjustment of the ablation parameters until sufficient ablation is achieved. Data is automatically recorded during the experiments and is ported to post-processing toolkit where image processing and quantitative analysis are performed integrating anatomical imaging, MRI thermometry

and histological photography results.

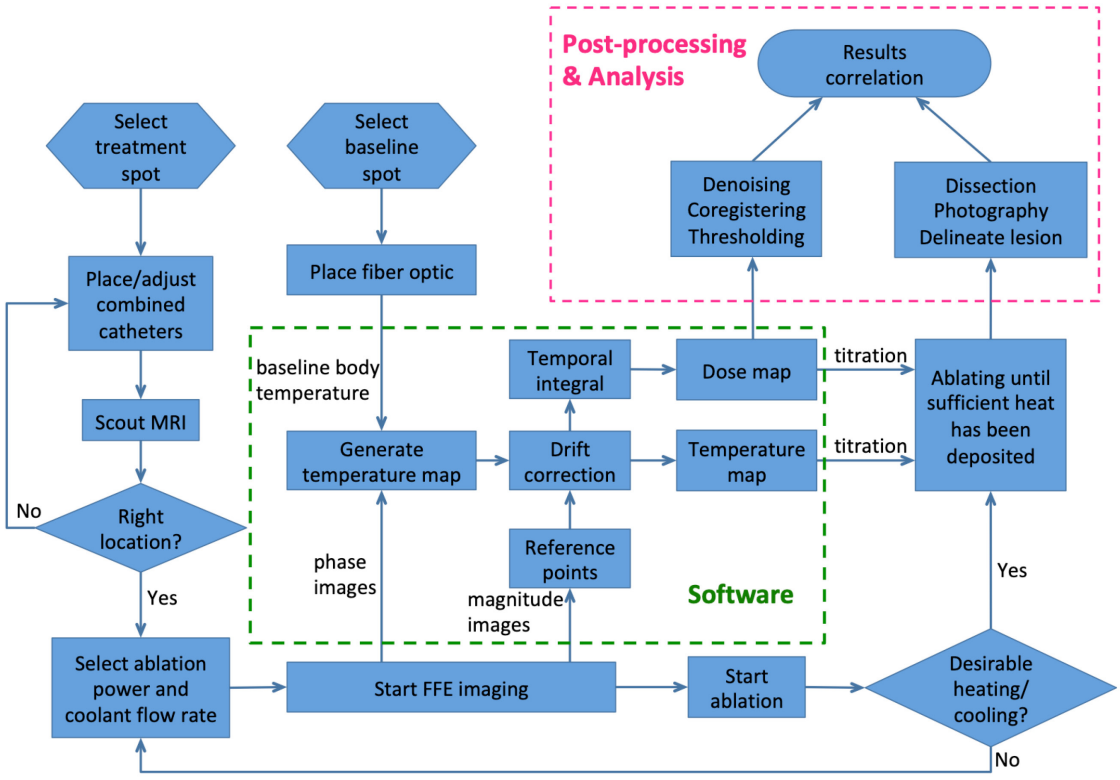

Figure 3.1 Work-flow chart showing protocol steps for IVMRI guided IVHIFU ablation studies. The protocol starts at the two preparation points indicated by hexagons, top left. Steps performed by software and post-processing algorithms are inside the dashed boxes.

3.2.2 *Ex Vivo* Studies

To determine the relationship between thermal dose measured by MRI thermometry and lesion size, and to characterize the ablation unit's settings and MRI thermometry signature that avoided tissue damage immediately adjacent to the probe, *ex vivo* ablations studies were repeated with IVMRI HIFU probes in different locations and different cooling, power levels and specimens.

The IVMRI HIFU catheter used in *ex vivo* studies was comprised of IVHIFU cathter #1 (Figure 2.2c, Table 2.1) taped with a loopless IVMRI antenna as shown in

Figure 2.2a. The catheter was inserted in the blood vessels of fresh porcine liver specimens. Each catheter-bearing specimen was immersed in a 10 L box of saline at 37 °C, which in turn was enclosed in a 1 cm-thick rigid polyurethane thermal insulating jacket. With the *TheraVision* ablation controller in the scanner console room, the coolant circulation tubing was connected to the catheter via a wall-port on the cable penetration panel penetrating the scanner's RF screen-room (see 2.2.2 Iterated Designs of IVMRI HIFU Devices and Figure 2.4),. High-resolution anatomical imaging was performed before and after ablation using balanced FFE (TR=6.2 ms; TE=2.4 ms; FA=20°; resolution=300 μm; slice thickness, SL=4 mm; FOV=150 mm); T_1-weighted FFE (T1FFE; TR/TE=15/3.9 ms; FA=7°; resolution=300 μm; SL=4 mm; FOV=150 mm); and three-dimensional (3D) fat-suppressed, T_1-weighted high-resolution isotropic volume examination (THRIVE; TR/TE=23/11 ms; FA=12°; resolution=300x300 μm; SL=4 mm; FOV=150 mm) sequences.

After locating the transducer and ablation target by sagittal and coronal IVMRI (see the checkpoint "*Right location?*" in Figure 3.1), an imaging plane was placed perpendicular to the HIFU transducer. Coolant was circulated and MRI thermometry commenced with real-time thermal monitoring (Figure 2.2f) using FFE Cartesian (TR/TE=100/25 ms; FA=25°; EPI factor=11; resolution =300 μm; SL=6 mm; FOV=150 mm; acquisition time=6.0 s) or radial (TR/TE=25/12 ms; FA=14°; angle density=50%; resolution=300 μm; FOV=150 mm; acquisition time=6.2 s) sequences. HIFU ablation was typically initiated after 5min of pre-cooling and continued for a period of about 6min.

Post-ablation, samples were sectioned at the ablation plane and photographed. To differentiate lesion from normal-appearing tissue, principal component analysis (PCA) was performed on approximately equal numbers of pixels from normal tissue (crimson) and lesions (pallid) in each photograph based on the International Commission on Illumination uniform color space ('1976 CIELAB') [97]. Color space values for each pixel were projected to the first principal component to generate scalar maps representing the appearance of pixels from normal tissue (lower values) and thermal lesions (higher values). The maps were normalized to a '$CIELAB_{1000}$' scale of 0 to 1000, with a threshold of $CIELAB_{1000}$=500 chosen to contour lesion areas using an active snake-contour object-detection algorithm [98]. The $CIELAB_{1000}$=500 contour traces the midpoint in intensity and hue between pixels in ablated tissue (pallid) and those in preserved tissue (crimson). Vessel walls were then traced manually on the photographs. Portions of the same lesions that extended to different dissections were co-registered based on their positions relative to the vessel wall to determine maximum lesion depths. Anatomical MRI scans were reconstructed at the thermometry plane by interpolation, co-registered with the CEM_{43}=340 dose contour, and annotated with the catheter and vessel wall locations. The images were scaled and co-registered with the contoured photos for comparison.

The gap, L_g (mm), comprised of non-ablated tissue lying between each lesion and the vessel wall, was measured as the average distance between the endo-luminal wall and the closest segment of lesion contour in the marked photographs. The longest radial distance, L_r (mm), between the lesion's distal-most and proximal-most points relative to the endo-luminal vessel wall, and the ablation area, L_a (mm^2), were also measured from

the dissections. L_g, L_r, and L_a were compared with the gap (mm) between the vessel wall and the CEM_{43}=340 contour; the longest radial length of the CEM_{43}=340 lesion contour; and the CEM_{43}≥340 contour area measured by IVMRI thermometry, respectively. Overlap between the CEM_{43}≥340 lesion areas and those from photos were quantified via the Jaccard index, equal to the fraction of the area of the intersection divided by the total area of the two together.

The post-ablation image processing and data analysis were implemented in *MATLAB* and applied identically in 8 (non-selected) consecutive liver ablation experiments performed with catheter #1 from Chapter 2, Table 3.1.

3.2.3 *In Vivo* Studies

To test the IVMRI guided HIFU ablation catheter *in vivo* where blood flow, perfusion, and physiological motion are potentially confounding, ablation experiments were performed in two live pigs under general anesthesia with approval of our Institutional Animal Care and Use Committee. *Psoas* muscle and colon near the inferior *vena cava* were selected as ablation targets. Real-time IVMRI thermometry with the loopless antenna was used to guide, target and titrate thermal dose.

In each anesthetized pig, the right common femoral vein was accessed with a micropuncture kit and sequential fascial dilators. A 16 French (Fr; 1Fr=1/3rd mm) 30 cm *Cook Medical* (Bloomington, Indiana, USA) sheath was placed and HIFU catheter #3 from Chapter 2, Table 2.1 was advanced into the IVC over a 0.035" (0.9 mm) guidewire in the central lumen of the catheter, under X-ray fluoroscopy. The position of the distal tip of the catheter was confirmed by fluoroscopy and cone-beam X-ray computed tomography. The 0.035” guidewire was replaced by the loopless IVMRI antenna. The left

femoral artery was accessed via a 5 Fr (1.7 mm) sheath and a fiber-optic temperature probe placed in the sheath to monitor body temperature far from the ablation site, for determining absolute temperature via the PRFS method. Pigs were heparinized prior to catheterization.

After catheterization, each animal was transferred to the MRI scanner, and the catheters were located by three orthogonal (transverse, sagittal and coronal) T_1-weighted FFE IVMRI projections (TR/TE=9.4/4.6 ms; FA=15°; FOV=300x300x400 mm^3; resolution=1.5 mm; scan time=10 s). Positioning was confirmed by T_2 weighted (T2w) turbo spin-echo imaging (TSE; TR/TE=4 s/95 ms; FA=90°; FOV=200 mm; resolution=0.7 mm, SL=5 mm) using a pair of *Flex-M* (*Koninklijke Philips N.V.*, Amsterdam, Netherlands) surface detector coils placed above and below the abdomen at the catheter's approximate location; and by high-resolution sagittal and coronal T_1 FFE images acquired with the IVMRI antenna using the same protocols as in *ex vivo* studies. The high-resolution transverse images were acquired to provide precise anatomical registration for thermometry for locating the ablation target and avoiding vessel injury. Device advancement and retraction was performed by an operator in the scanner room in communication with the scanner operator.

Pre-cooling was commenced followed by high-resolution real-time MRI thermometry (Pig #1: radial acquisition, TR/TE=25/7.7 ms, FA=14°, angle density=100%, resolution=0.5 mm, FOV=150x150x6 mm^3, acquisition time=7.5 s; Pig #2: Cartesian acquisition, TR/TE=168/17 ms, FA=30°, EPI factor=11, resolution=0.5 mm, FOV=150x150x6 mm^3, time of acquisition=6.0 s) employing the loopless antenna as a receiver and the MATLAB software interface for temperature

monitoring (Figure 2.2f). Based on evidence of heating by MRI thermometry, torque was applied to the ultrasound catheter to rotate the HIFU beam to the intended target. With HIFU power titrated based on IV-MRI thermometry, sufficient heat was deposited in the target to form a lesion, as guided by the results of the *ex vivo* studies. The transducer was powered off and the catheter was withdrawn 1-2 cm along the blood vessel. MRI and ablation procedures were then repeated to create separate or contiguous thermal lesions.

Animals were humanely euthanized, post-ablation. The IVC through which the catheters were routed, the colon wall, adjoining *psoas* muscle and other tissue surrounding the ablation sites were harvested and assessed for lesion formation and comparison with the thermal dose measured by MRI thermometry. Dissected tissues were fixed and processed for histology with hematoxylin and eosin (H&E) and Masson's trichrome (MT) staining which was reviewed by a pathologist (Dr. Kathleen Gabrielson from the Department of Molecular & Comparative Pathobiology, Johns Hopkins School of Medicine, Baltimore, MD, USA). Movat staining was also used to highlight vessel wall in some *in vivo* and *ex vivo* studies.

3.3 Results

3.3.1 *Ex vivo* Studies

Figure 3.2 illustrates an IVMRI-guided HIFU ablation accessed from a blood vessel in a porcine liver using catheter #1 (Figure 2.2c). Dynamic MRI thermometry shows the evolution of the temperature rise 5-10 mm away from the vessel wall (Figure 3.2d-f). Figure 3.3a shows a dissection through the ablation plane. Figure 3.3b is the corresponding $CIELAB_{1000}$ map of the dissection used for segmenting the lesion. Figure 3.3c shows an annotated anatomical MRI reconstructed at the thermometry plane,

delineating the CEM_{43}=340 contour. Figure 3.3d shows the dissection annotated with the CEM_{43}=340 contour, co-registered with the $CIELAB_{1000}$=500 contour. The estimates (depth, area, and gap to vessel) of lesion area enclosed by the CEM_{43}=340 contours and the lesion areas measured from all the samples sections are plotted in Figure 3.4 and are highly correlated (r >0.79; p <0.02). The ablations spared the intervening vessel wall by >0.5 mm in 6 of 8 experiments (Figure 3.4c), with one failure due to parting of the tape affixing the IVMRI antenna to the HIFU catheter, which was a temporary measure as discussed earlier (Chapter 2.4 Discussion). Jaccard indices for the 8 experiments are all >0.51 (Figure 3.4d).

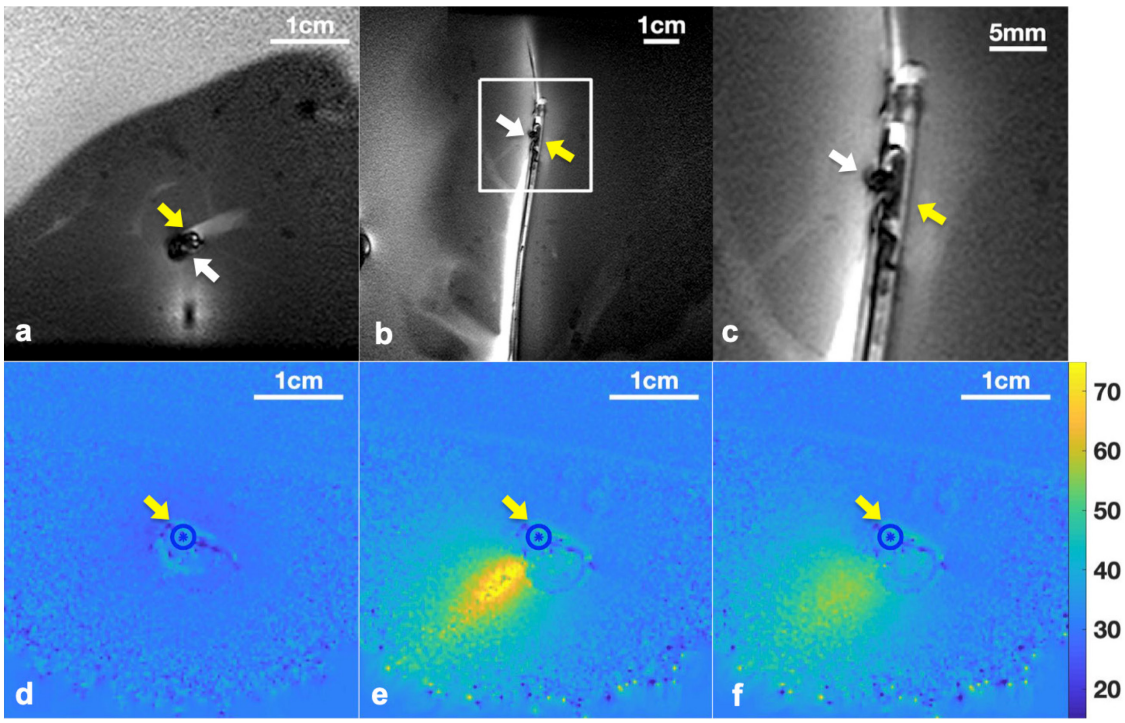

Figure 3.2. Images of the IVMRI antenna (white arrow) and HIFU catheter #1 (yellow arrow) in a blood vessel of pig liver *ex vivo* in transverse (a) and co-axial planes (b: inset denotes the expanded region in c). MRI thermometry shows temperature maps (scale in °C at right) from the transverse slice in (a): before ablation (d); during ablation at maximum temperature (e); and immediately after the HIFU transducer is turned off (f).

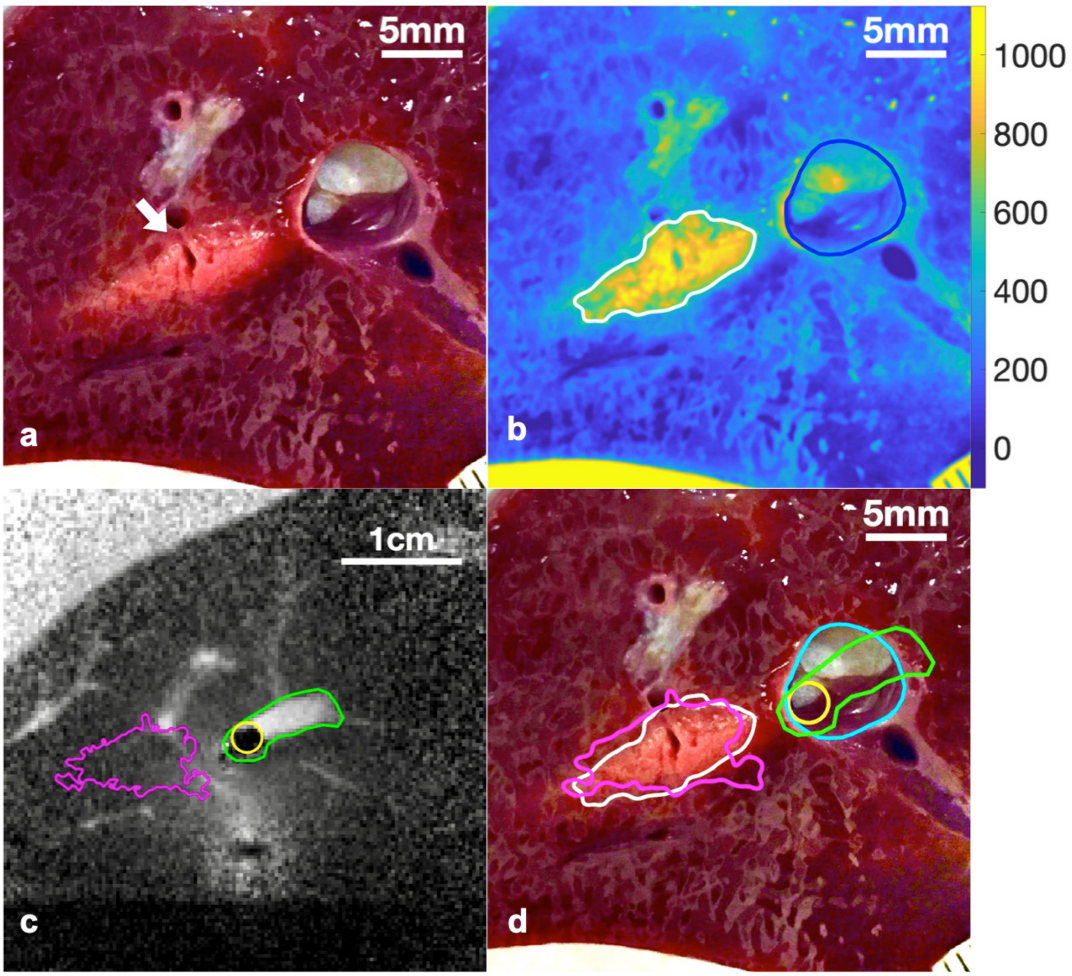

Figure 3.3 Co-registration of lethal thermal dose contours with lesions on tissues slices dissected after ablation experiments performed with catheter #1 located in pig liver blood vessels *ex vivo*. Tissue slices at the ablation location expose the pallid lesion area (white arrow) (a). The projected, normalized color mapping of the section differentiates the lesion from normal tissue (b, scale at right). The lesion area (white line) is identified by an active contour algorithm for object detection. The vessel wall is manually traced (blue line). The $CEM_{43} \geq 340$ (magenta line) contour is calculated from MRI thermometry and co-registered on the anatomical MRI reference scan (c). The catheter (yellow circle) position and the enclosing vessel (green line) are identified manually on the reference scan. Landmarks identified from MRI, MRI thermometry and the photo color map are co-registered on the original photo for comparison and correlation (d).

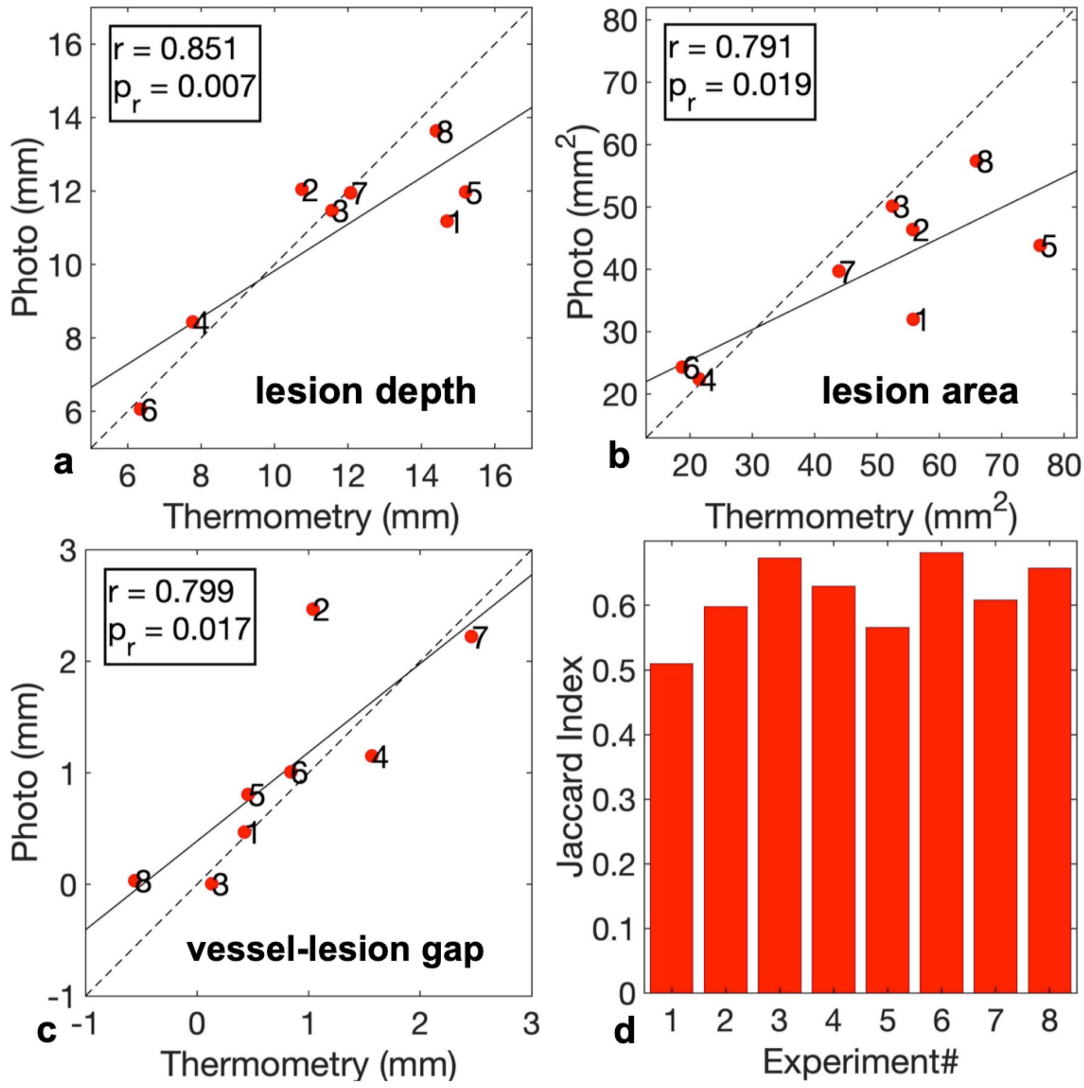

Figure 3.4 Comparison of lesion sizes exceeding a thermal dose $CEM_{43} \geq 340$ as measured from MRI thermometry, with lesions measured from photos of the dissected ablation planes. The radial depth, L_r (a); area, L_a (b) of lesions; and the average gap between lesion and vessel wall, L_g (c), are correlated (correlation coefficient, $r > 0.79$; Pearson probability, $p < 0.02$; solid lines, least-squares regression line; the dashed line is the identity line). Numbers near the data points denote the experiment number (a-c). Part (d) shows the Jaccard index (area of intersection divided by the area of the united lesion areas) for each experiment.

3.3.2 In vivo Studies

Sagittal T2wTSE images confirmed the location of the IVMRI HIFU ablation catheter #3 in a porcine IVC *in vivo* via its hyperintense signal (white arrow, Figure 3.5c). With three orthogonal image projections, the catheter was easily located within a minute.

A high resolution, axial MRI acquired from the IV antenna in the catheter lumen is shown in (Figure 3.5d). Thermometry for several ablations in the *psoas* muscle and colon are shown in Figure 3.6a-e. Initially, power was applied to the HIFU transducer to determine the ablation path. Within 7-15 s it was evident that the HIFU beam was not facing the *psoas* muscle target. This was maintained for 70 s to produce the thermal map in Figure 3.6c. The catheter was then rotated towards the target (Figure 3.6d). In addition, to the *psoas* muscle, power was applied to the transducer on the opposite side of the catheter to test whether it could access and ablate the colon (Figure 3.6d,e). The HIFU power levels were ~11 W for 6 min per transducer. The MRI times were 10 s for a scout localization image; 5 min for localization and high-resolution anatomical MRI; and 8-12 min for thermometry scanning during and post-ablation for each treatment target.

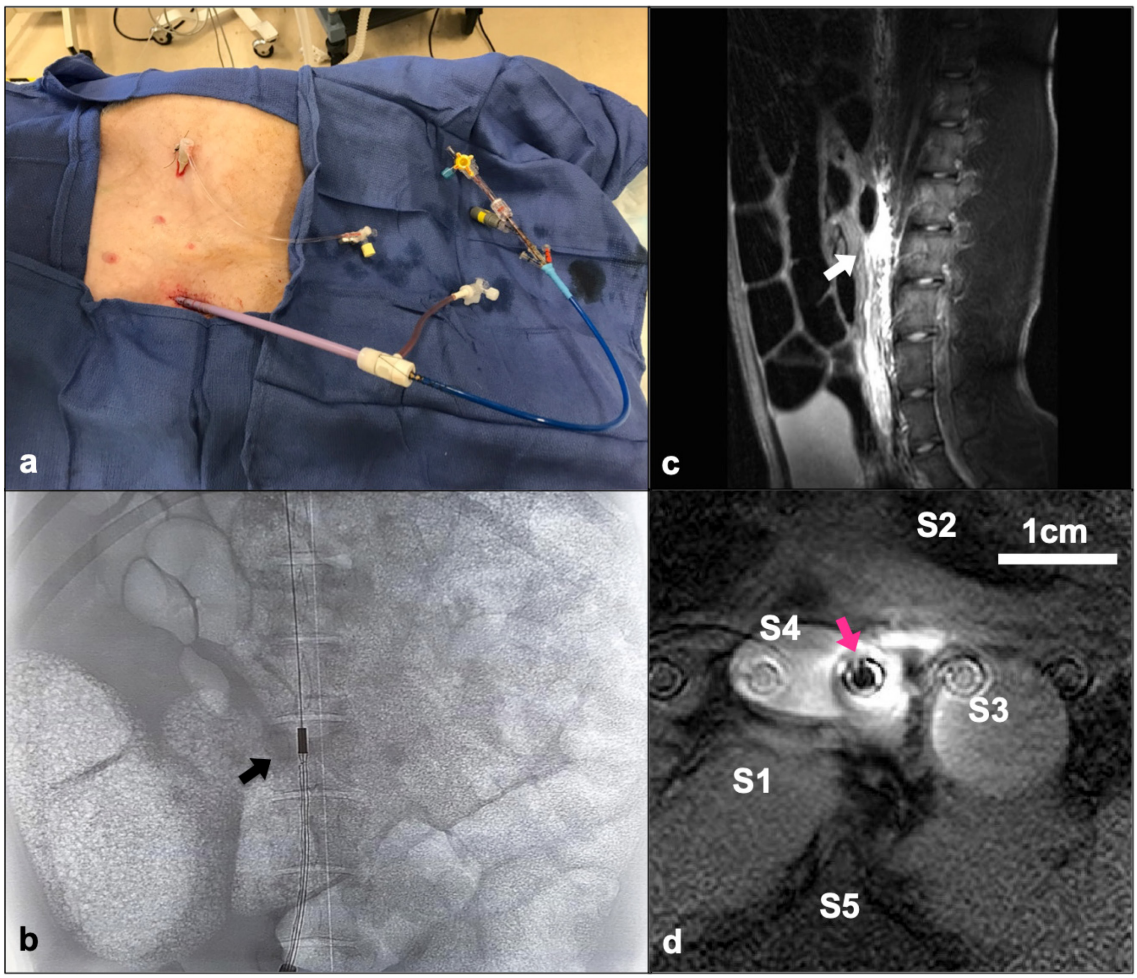

Figure 3.5 Placing an IVMRI HIFU catheter #3 in a porcine IVC from the right femoral vein *in vivo* (a) confirmed by fluoroscopy (b). The left femoral artery is accessed by a 5 French sheath (a), for a fiber-optic temperature probe to monitor the body temperature for base line calibration of the PRFS method. Sagittal T2wTSE MRI (c; white arrow). High-resolution IVMRI (d; pink arrow denotes catheter; S1 is the targeted psoas muscle; S2 is the colon, a second target; S3, aorta; S4 is the IVC; S5 is the spine).

Post-mortem sectioning revealed thermal lesions on the mucosa surface of the colon (Figure 3.6f) and the *psoas* muscle where ablations were performed (Figure 3.6g,h). We observed no evidence of a lesion at the site of the mis-directed beam. Histopathology confirmed skeletal muscle degeneration, edema and hemorrhage in H&E stained slides, consistent with thermal lesions.

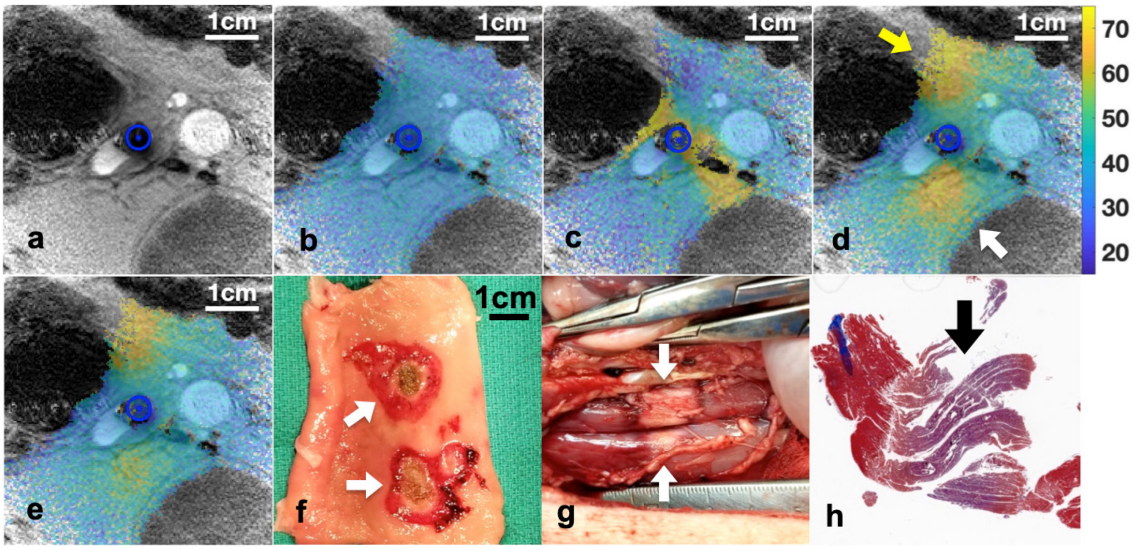

Figure 3.6 Anatomical reference scan for an *in vivo* porcine study (a); and IVMRI thermometry frames (scale in °C at right) acquired pre-ablation (b); Initial mis-direction of the thermal beam was detected by thermometry (c) and redirected to the psoas muscle; during ablation of the psoas muscle (white arrow) and colon (yellow arrow; d); and immediately after turning the transducer power off (e). Blue circles denote the catheter location. Part (f) shows thermal lesions in the colon mucosa from multiple ablations (white arrows). Part (g) shows thermal lesions in psoas muscle (g, white arrows). Part (h) shows MT-stained histology of the lesion (black arrow).

In a second pig study, ablations were performed at three locations approximately 1cm apart during a 'pullback' to create a contiguous ablation lesion during simultaneous thermal monitoring. At each location, an anatomical reference image was acquired for thermometry, followed by continuous thermometry (Figure 3.7b-d). As in Figure 3.6c, the HIFU beam in the first location (Figure 3.7b) was mis-oriented too far clockwise relative to the target and the catheter was rotated slightly for the second and third ablations (Figure 3.7c,d).

Post-mortem dissection revealed evidence for three thermal lesions on the *psoas* muscle at the ablation locations beneath the IVC. The first lesion was rotated relative to the others (Figure 3.7e, white arrow). The second and third lesions (yellow and cyan arrows) were contiguous. The thermal lesions were confirmed by histopathologic

evidence of skeletal muscle degeneration, edema and hemorrhage. The IVC segments dissected post-ablation showed no gross lesions visually, but vessel wall hemorrhage was noted in some histological slides. Whether hemorrhage was caused by mechanical abrasion from the catheter or by thermal injury was unclear.

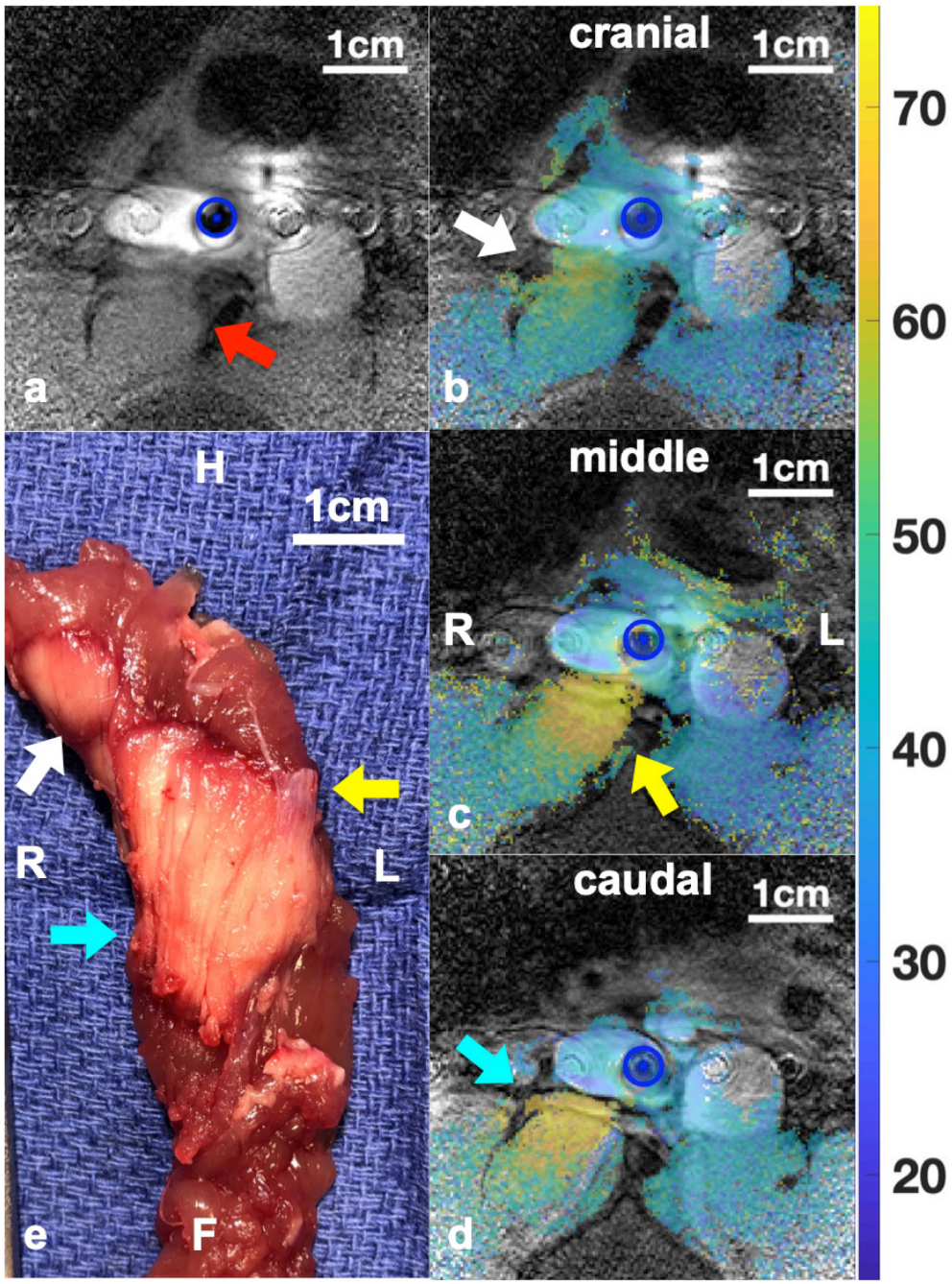

Figure 3.7 IVMRI thermometry of ablations performed at three locations (during pullback from head to feet direction) in the psoas muscle in a second *in vivo* porcine study using catheter #3. The anatomical MRI reference scan at the first location (a) shows the ablation target (red arrow). Part (b-d) shows the temperature rise (white, yellow and cyan arrows) during ablation (scale in °C at right) at three pullback locations. In (b) the thermal beam is slightly clockwise of the target so the device was rotated for the acquisitions in (c) and (d). Blue circles denote the catheter location. Part (e) shows the post-mortem photo of thermal lesions in the psoas muscle. The first ablation lesion (e; white arrow) is skewed relative to the second and third lesions (e; yellow and cyan arrows) which extend to form a continuous lesion.

3.3 Discussion

Chapters 2 and 3 are the first reports on IVMRI-guided transvascular HIFU ablation. The technology combines IVMRI's advantages of high-resolution, multi-functionality and a unique thermal mapping capability [51], with access to extra-vascular ablation targets afforded by IVHIFU. It thus presents an ablation therapy option for situations where conventional extra-corporeal MRI-guided HIFU may not be possible due to acoustic opacity, or to the presence of critical tissue or vessels in the path of the external beam. The results demonstrate that IVMRI guided HIFU ablation can be reliably performed up to the edge or within a millimeter of, the intervening vessel wall without thermal injury (Figure 2.6, Figure 3.3, Figure 3.4). Surprisingly perhaps, the performance of the IVMRI antenna was little impaired by the presence of the HIFU transducers and cooling system. Although we used X-ray fluoroscopy to guide initial catheter placement, a fully MRI-guided interventional procedure is the ultimate goal, and we are testing whether high-speed 'MRI endoscopy' can be developed to serve as a possible MRI-based catheterization modality [52,99,100]. Meanwhile, the present *in vivo* studies demonstrate a viable protocol for locating the ablation catheter relative to the anatomy; manipulating the ablation transducers to direct them at an ablation target; and titrating the delivery of thermal therapy. As such, the technology seems promising for treating tumors that are currently surgically inaccessible, or that are non-resectable due to perivascular involvement.

IVMRI probes of the same design used here have been tested *in vitro* and *in vivo* at 1.5T and 3T, and were shown to be safe from RF heating when used alone [49,50]. Here, the probes were turned-off during MRI transmission, but their use in conjunction

with a HIFU catheter could introduce new coupling mechanisms and risks of heating. However, the high isolation indicated by the S21 measurement; the lack of MRI artifacts other than the absence of signal from components that lack mobile protons (Figure 2.6, Figure 2.9a, Figure 3.2); and the preservation of tissue immediately adjacent to the catheter (Figure 3.4), suggest that electromagnetic coupling, if extant, is minimal. Moreover, the IVMRI probe benefits from the HIFU transducer's cooling system and non-conducting polymer sheath, especially in catheter #3 used *in vivo*. Here, the whip junction–which is expected to heat the most [49]–is completely enclosed by it, so if it does heat during MRI, the water cools it. While loopless IVMRI antennas were used here because of their small size, loop antennas could also be deployed if the isolation from the HIFU transducer is similarly maintained. Incorporating them into the HIFU transducer space instead of the lumen would allow an OD of ~2 mm, and a discoidal-shaped FOV suitable for transmit/receive MRI endoscopy [50].

The highly-localized sensitivity of the IVMRI antenna (Figure 3.5c) enables localization of the transducer in a few projections that could be incorporated into an automated pre-scan localization routine [100] and followed by user-prescribed high-resolution imaging and thermometry. Although not used here, the localized sensitivity profile of each projection may also provide a means of motion-correction [52]. Like conventional thermometry, high resolution IVMRI thermometry is subject to drift in the reference phase during procedures [33,101–103]. Acquiring a reference phase image prior to commencing each ablation, limits the potential drift period to the duration of each ablation. Moreover, for highly localized IVHIFU ablation targets, monitoring temperature

remote from the ablation site, which presumably remains at body temperature (Figure 3.6, Figure 3.7), provides a measure of drift for correcting temperature.

Of the three HIFU transducer designs introduced in Chapter 2, the testing here showed that the flat (catheter #1) and cylindrical segment or 'sector' (catheter #3) transducers penetrated deeper than the transducer with the 360° radial pattern (catheter #2), if only because the latter had a higher driving frequency (Table 2.1) and hence a higher attenuation in tissue [104]. Nevertheless, the catheter #2 transducer preserved a ring of tissue and was more efficient at ablating a circular lesion for creating an ablation margin around the vessel, for example (Figure 2.6a). Including the lumen in catheter #3 (Figure 2.2b) provided easier device exchange without risking detachment. It also facilitated multi-modality image guidance–X-ray fluoroscopy and MRI–with less metal artifacts in the images (Figure 2.9a). More precise control and tailoring of the thermal ablation beam could be achieved in future by adding more individually-powered transducer elements.

Improving the IVMRI HIFU catheter design to reduce its diameter and increase its flexibility is important for facilitating interventional procedures, especially where access to pathologies from smaller vessels is being sought. While the evidence is inconclusive, we think that the overall size and flexibility of catheter #3 (4.3 mm OD), was the likely cause of the occasional hemorrhage seen in the second *in vivo* study, given the absence of MRI thermometry and histological evidence for vessel wall heating at ablation sites where exposure was greatest(Figure 2.9, Figure 3.4, Figure 3.5, Figure 3.6). Heating affects are potentially ameliorated by adjusting the coolant temperature and/or flow. Catheter biocompatibility is best evaluated with sham procedures not involving

MRI or HIFU. The development of an IVMRI HIFU needle may be another option for interstitial targets or where vessel size is limited.

That the temperature and flow of coolant to the probe affects the preservation of adjacent tissues suggests a dual role for it in cooling both catheter and the tissue immediately surrounding it. Although we set the *TheraVision* system's water-cooling heat exchanger in the console room at 3 °C and used closed-cell polyurethane thermal insulation on the 5 m long coolant hoses, the combined effect of the ~20 °C room temperature and heating during ablation, resulted in a coolant temperature at the catheter head of an intermediate 10-13 °C. The coolant temperature at the catheter could be reduced by establishing a reservoir inside the scan room or by increasing the flow-rate. However, the flow-rate is limited by catheter size, whose diameter is ultimately constrained by vessel size.

The acquisition of temporal MRI thermometry data enabled calculation of the thermal dose in CEM_{43} and the estimation of the shape and size of thermal lesions (Figure 3.3, Figure 3.4a,b). As a threshold for producing thermal coagulation and lesions [63,64], we observed that the CEM_{43}=340 contour derived from MRI thermometry tended to overestimate the size of lesions identified by quantitative analysis of the sample dissections (Figure 3.4). In some experiments (#1, #5 in Figure 3.4a,b), significant areas of lesion appeared on different slices which may have contributed to underestimation in the individual dissections, as compared to thermometry. Some tissue loss and deformation of lesion areas is also inevitable during the preparation of dissections. The finite length of the HIFU transducer (~1 cm) and limited depth of ablation parallel to the catheter's long axis are other mitigating factors.

In addition, CEM_{43}-based methods can overestimate thermal injury in a manner that depends in a complex way on the temporal temperature profile [64]. Lesions manifesting significant color changes at gross examination are likely to correspond only to fully-coagulated cores and may not extend to the entire lesion area. Indeed, various studies have shown that the coagulation core continues to expand up to 2 weeks post-ablation, gradually establishing a rim that is evident on MRI and comprised of non-viable liquefying cells at histology [105–108]. Both of these considerations would tend which would reduce CEM_{43}-based over-estimation of lesion size *in vivo*.

In conclusion, IVMRI guided and IVMRI titrated IVHIFU has the potential for precision ablation of perivascular tumor and other pathological tissues, while preserving vessel wall. The technology potentially offers a new approach to treating localized disease including inaccessible tumors or pathologies involving critical blood vessels. It is possible that such a procedure could render a non-resectable tumor, resectable. As the current study demonstrates feasibility of IVMRI-guided IVHIFU, given the size of the current devices, further *in* vivo testing would require evaluation on a large animal tumor or disease model.

Chapter 4: Real-time high-resolution MRI Endoscopy

4.1 Introduction

Atherosclerosis is a prevalent factor in cardiovascular disease and a leading cause of mortality and morbidity [109–111]. While over a million X-ray guided catheterizations are performed in the USA annually to diagnose and treat the disease, X-ray angiography can only detect lumen contours which limits its ability to assess early and advanced lesions and their progression [112–114]. Coronary X-ray CT angiography can assess plaque burden via the presence of calcification, but is unable to characterize many of the soft tissue pathologies that distinguish the American Heart Association's (AHA) classifications for vessel disease [115,116]. Other minimally-invasive imaging options include IVUS and OCT, which are clinically available but not widely used. These can offer improved spatial resolution and contrast for evaluating stenoses, identifying potentially vulnerable lesions, and facilitating intervention [35,117,118]. Confounding factors are the presence of calcifications in the case of IVUS [119,120]; and optical penetration and a requirement for blood-free access to the vessel wall, in the case of OCT [39,121]. Moreover, all of these modalities employ X-ray guidance and hence expose patients and operators to ionizing radiation. Our goal is high-resolution MRI endoscopy with real-time imaging speeds comparable to existing endoscopy modalities.

IVMRI is a newer approach that employs miniature MRI detector coils mounted on guidewires or catheters for use in higher-field MRI scanners. It can provide high-resolution and soft tissue contrast for characterizing different stages of vessel disease without using X-rays [10,50,100]. An 'MRI endoscopy' mode is also possible with IVMRI, wherein a continuous stream of images is acquired from the point-of-view of the

detector coil, to which the image frame is intrinsically locked. This is achieved by dispensing with the traditional MRI slice-selective excitation which is fixed to the scanner's frame-of-reference. Instead, the highly-localized receiver sensitivity profile of the tiny MRI coil combined with an endoscopic MRI sequence that employs adiabatic MRI (RF) excitation, limits MRI sensitivity to a 3-5 mm (full-width-half-maximum) thick uniformly-excited 'sensitive disk' which is intrinsically locked to the coil and moves with it. Like an optical endoscope used for colonoscopy, the MRI endoscope provides a 'probe's eye' view from inside the vessel. Unlike optical endoscopy, MRI endoscopy can see through the vessel contents and the vessel wall to potentially locate and characterize trans-luminal and extra-vascular disease as the probe is advanced [88,100]. Unfortunately to date, MRI endoscopy has been limited to about 2 fps at 300 μm resolution for real-time visualization in blood vessels [100]. The speed is limited because state-of-the-art SENSE MRI methods are not possible with a single-channel endoscope, and because the reconstruction (and acceleration) rates of existing iterative compressed MRI methods have not been fast enough and have required off-line iterative processing that is unsuitable for practical endoscopy applications [52]. Thus, true real-time MRI endoscopy at frame-rates suitable for interventional, catheterization or endoscopy procedures has not yet been realized.

A highly-accelerated real-time MRI system was recently developed for conventional multi-channel MRI with transmitters and receivers that are fixed to the scanner frame-of-reference and its localizing gradient system [122–124]. The system uses highly under-sampled radial pulse sequences and a temporally-regularized, iterative, NLINV reconstruction algorithm, implemented with cascaded GPUs to provide

essentially instantaneous image reconstruction and visualization. Here we report the novel incorporation of this technology to create a real-time (single-channel) MRI endoscope that can move relative to the scanner's frame-of-reference with continuous microscopic visualization at up to 10fps, in-plane resolution of 200-300 μm and an imaging FOV of 2-3 cm without inducing significant local heating. After calibration and safety testing, a uniform MRI excitation FA is excited by the tiny coil at the end of the endoscope using adiabatic "B_1-independent rotation" (BIR-4) RF pulses [125], and the size of the FOV or 'sensitive disk' is adjusted independent of the scanner's frame-of-reference. The software operates on a regular clinical MRI scanner with the GPU hardware connected via a high-speed ethernet cable (Figure 4.1). Results from animal and human vessels *ex vivo* and from animal vessels *in vivo* are demonstrated and the structural and temporal information in the highly-accelerated image streams are compared with fully-sampled MRI endoscopy scans using image similarity metrics, and with tissue dissections and histology.

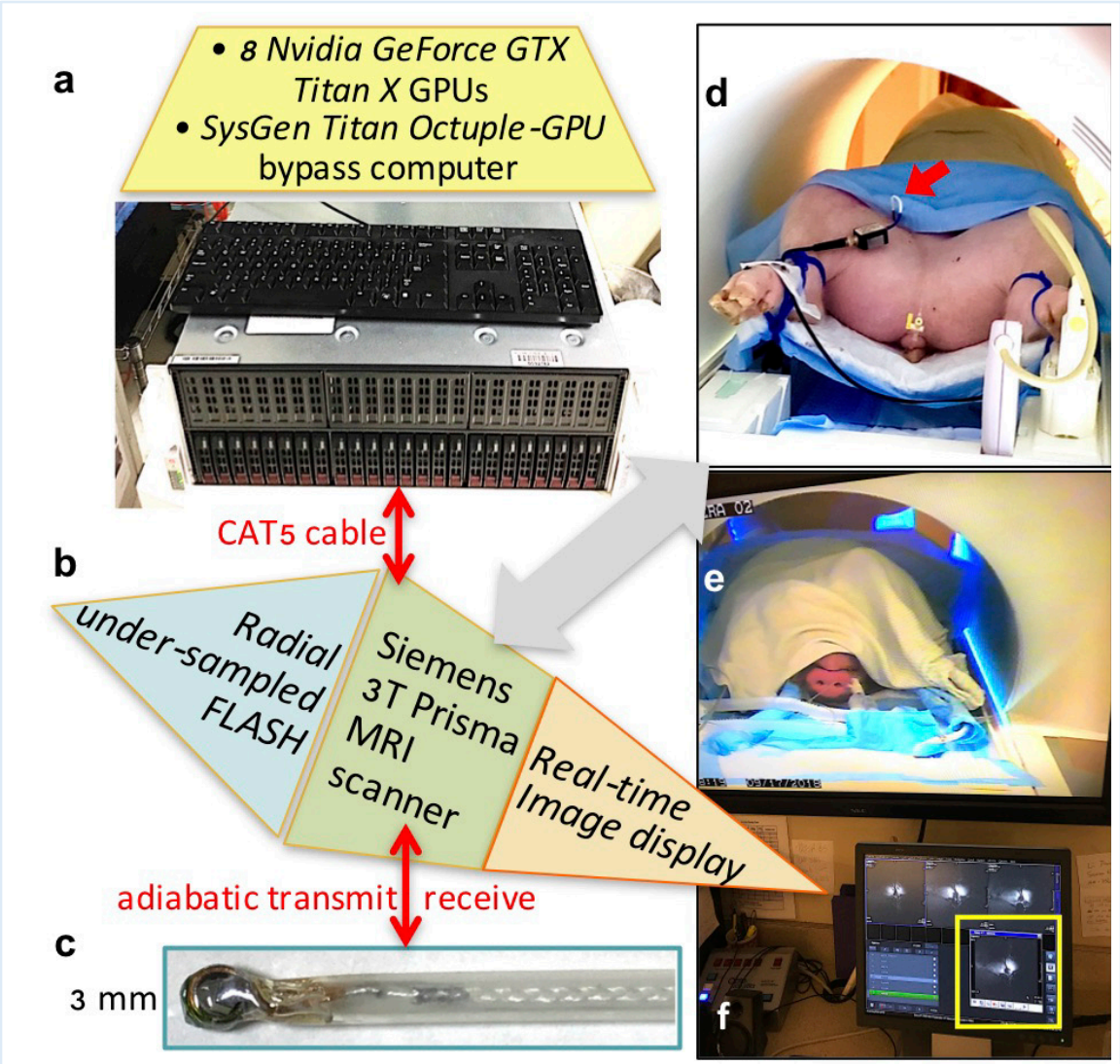

Figure 4.1 (a-c) Block diagram of the MRI endoscope. (a) 8-cascaded GPUs controlled locally by a GPU computer programmed to perform undersampled radial image reconstruction in real time are connected to (b), a 3T clinical MRI scanner via a CAT5 computer cable (red arrow). The MRI scanner is programmed for high-speed (fast low-angle shot, FLASH) MRI to drive (c), a 3mm transmit/receive endoscope (red arrow), via a tuned interface and preamplifier. (d) The endoscope accesses the vasculature of a (porcine) subject lying in the magnet of the MRI scanner (grey arrow) via the femoral artery, during (e) video monitoring as (f) the endoscopic images are displayed in real-time on the at the scanner's display window (yellow box) and on an in-room monitor.

4.2 Methods

4.2.1 MRI Endoscopy

Four 3 mm diameter prototype MRI endoscopes were fabricated for use in studies performed on a clinical 3T MRI scanner (*Prisma*, Siemens Healthineers AG, Munich, Germany). The endoscopes had 3-5 turn transmit/receive coils that were tuned to the 123.2 MHz MRI frequency with micro-chip capacitors and mounted on ¼-wavelength ($\lambda/4 \approx 42$ cm), 50 Ω, flexible, 1.25 mm diameter, silver-plated micro-cable and enclosed in a 2.4 mm polymer sheath (Nylon 12, 64 Shore D hardness; Figure 4.1c. and Figure 4.2). The endoscopes were matched to 50 Ω when immersed in saline with tissue-comparable RF electrical properties (Figure 4.2) and interfaced to the MRI scanner via two ganged (gain, 26 dB+20 dB) low-noise (noise figure, 0.4-0.5 dB) preamplifiers at the receiver's front-end [50]. A switchable 20 dB attenuator was connected to the scanner's RF transmitter amplifier output.

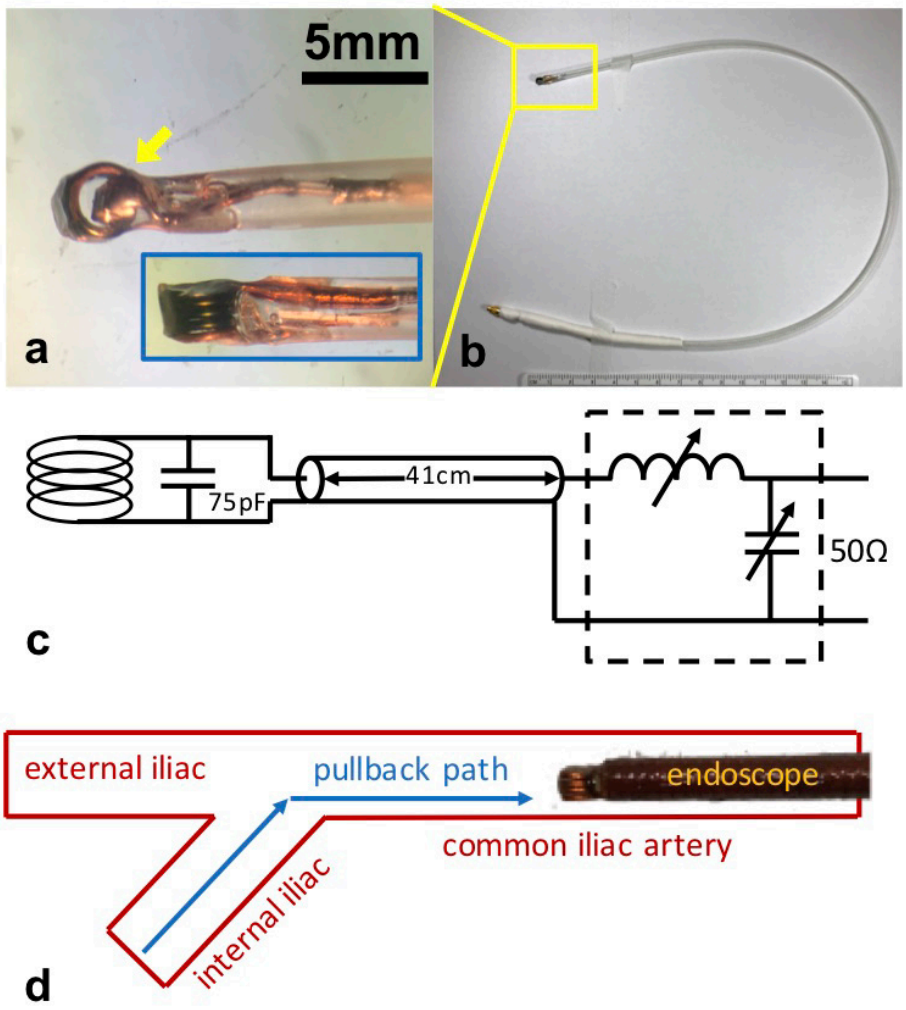

Figure 4.2 MRI endoscope. Photos of: (a) a 5-turn, 3 mm diameter, endoscopic MRI coil tuned to the 123.2 MHz MRI frequency with a tuning capacitor inside (yellow arrow). (b) The coil is mounted on a flexible 41-cm 50 Ω flexible coaxial cable (silver-plated copper conductor; perfluoroalkoxy-dielectric and jacket; 1.25 mm outer diameter) in a polymer sheath (Nylon 12, 64 Shore D hardness, 2.4 mm outer diameter). (c) Circuit diagram showing the coil, coaxial cable and matching circuit (dashed box) which is connected to the scanner preamplifiers. (d) A 'pullback' protocol in the left common iliac artery from an internal iliac branch.

The MRI acceleration unit was comprised of 8 *Nvidia GeForce GTX Titan X* (*Nvidia*, Santa Clara CA) GPUs and a 'bypass' computer (sysGen/TITAN Octuple-GPU, Sysgen, Bremen). This unit was developed by Dr Jens Frahm and associates and assembled at the Max Planck Institute in Goettingen, Germany as described

previously [122–124] with Drs Jens Frahm and Dirk Voit from the institute collaborating on this project. The unit was connected to the Siemens scanner via a single ethernet cable and configured to provide continuous real-time image display at the scanner console (Figure 4.1). MRI was accelerated using highly under-sampled radial acquisitions (9-17 projections per image frame), and reconstructed in the bypass computer with a highly-parallelized version of the NLINV algorithm [126] which jointly estimates image and coil sensitivity (minimum latency period, 1 frame). Although the NLINV reconstruction also accommodates corrections for the slow-varying sensitivity profiles of regular MRI coils, a spatial pre-filter was developed at Johns Hopkins and applied to the raw projection data to compensate for the extreme inverse-radial (~1/r) dependence of the coil's detection sensitivity and enhance conspicuity in the periphery of the FOV, analogous to that used previously [50]. The filter and its effect are detailed in 4.2.5 Preprocessing Filter. During high-speed endoscopy, radial projections were acquired from a continuous application of a fast low-angle shot (FLASH) MRI sequence [127] programmed with the adiabatic BIR-4 pulses (pulse duration: 4 ms; frequency sweep: ±10 kHz) in lieu of spatially-selective excitation. Applying these pulses with the endoscopic coil as a transmitter restricted the MRI sensitivity to an approximately discoidal volume (Figure 4.3a) that moved with the probe, no longer locked to the frame-of-reference of the scanner's localizing gradient system [100].

The sequence operating parameters were adjusted to match the probe's excitation and detection sensitivity, which declines rapidly with distance from the coil. The amplitude of the excitation field (B_1) sets the adiabatic threshold of the BIR-4 pulses and effectively sets the radius of the sensitive disk. This was calibrated by varying the

scanner's nominal transmit voltage (Tx at the RF power amplifier, excluding intervening losses) from 1.6–25 V with the endoscope placed in the saline phantom using a long repetition period (TR=5 s) short-echo-time (TE=4.4 ms) gradient-recalled echo (GRE) BIR-4 sequence. The average radial sensitivity profile was plotted as a function of distance from the coil (Figure 4.3a,b). Nominal transmit RF voltages of 6.3 V and 18.8 V were chosen for *ex* and *in vivo* studies, to provide effective FOVs of ≥20 mm and ≥30 mm, respectively (Figure 4.3b). RF heating of the endoscope during continuous high-speed endoscopy with the probe at the same location for 2 minutes (600 images) at TR=20 ms was measured in the saline phantom in the scanner with fiber-optic temperature probes placed at the tip where peak heating occurs and at more remote locations [50,51,100].

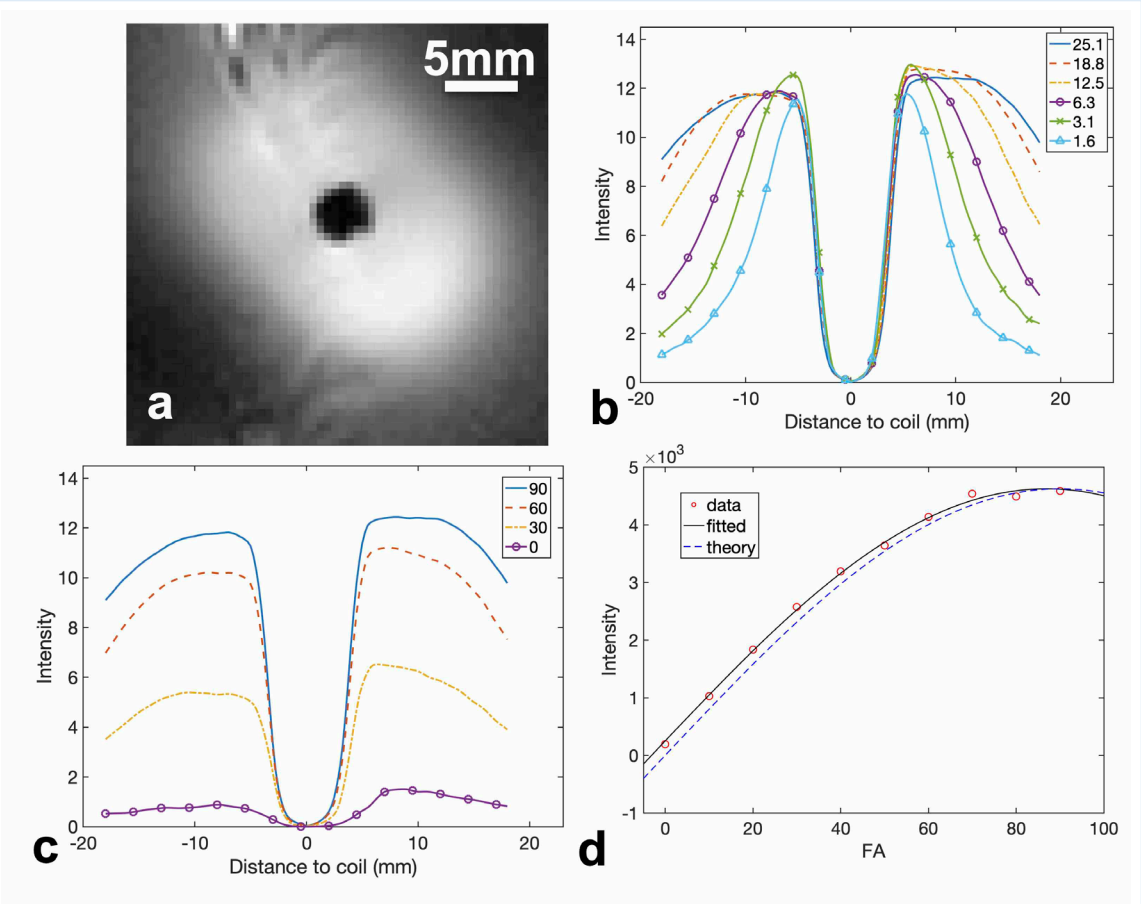

Figure 4.3 Adjusting the adiabatic BIR-4 excitation pulse during endoscopic MRI to independently control FOV and sensitivity. (a) Image of the endoscope's 'sensitive disk' in a homogeneous phantom (GRE image; repetition period, TR=5 s; echo time, TE=4.36 ms; nominal BIR-4 flip angle, FA=90°; FOV=38 mm; transmit voltage Tx=25.1 V). (b) Adjusting FOV. Reducing pulse power (Tx) at a constant FA=90° decreases the BIR-4 pulse's threshold for adiabaticity and hence the FOV. (c) Sensitivity optimization. The average radial MRI signal plotted with different BIR-4 FAs at Tx=25.1 V. The FOV is independent of FA. (d) Calibration of FA. The image intensity as a function of the nominal FA of the BIR-4 pulse fitted to a sine function reveals a fixed 5° offset error in FA.

The MRI FA of the BIR-4 pulse was adjusted to maximize the SNR with the probe stationary. FA is set by phase jumps within the pulse [50,125] which are typically miss-set in MRI scanner hardware [128]. This is normally remedied by cycling the BIR-4 pulse's phase which was not possible here because the extreme acceleration precluded repetition of phase-cycled projections. Instead, the FA of the BIR-4 pulses was calibrated

in the saline phantom, with nominal 'scanner' FAs varied between 0° and 90° at 10° increments at long TR and a fixed Tx=25.1 V (Figure 4.3c). The maximum image intensity for a given Tx was fitted to the sine of the nominal FA (Figure 4.3d) to determine the true FA [128], and the resultant offset error (5°) subtracted from the scanner FA when applying our BIR-4 sequences and reporting the FAs.

4.2.2 *Ex Vivo* Experiments

High-speed real-time MRI endoscopy was first tested in healthy porcine blood vessels (4 samples) and in diseased human blood vessels (7 samples) *ex vivo*. Fresh porcine vessels (≤24 hrs post mortem) were obtained from commercial research suppliers (Animal Biotech Industries, Doylestown, PA; Spear Products Inc, Coopersburg, PA). De-identified human vessels harvested post-mortem from elderly voluntary donors were obtained from the John Hopkins' autopsy service. These commonly show evidence of atherosclerosis lesions and calcifications detectable by MRI endoscopy. Vessels were mounted on a rubber platform at the center of a (0.35%) saline solution placed in the MRI scanner. The MRI endoscope was placed at the distal end of the vessel, the endoscopy sequence commenced, and the coil retracted by an operator from the end of the scanner (Figure 4.2d).

Real-time BIR-4 FLASH MRI endoscopy of porcine carotid arteries was performed at 6 and 10fps (FOV=45 mm; resolution=200 μm; FA=10°; TR/TE=11.5/6.68 ms; projections/image frame =15 for 6 fps (172.5 ms/frame), 9 for 10 fps (103.5 ms/frame); pullback rate = 2 mm/sec). A fully-sampled BIR-4 GRE Cartesian MRI sequence used previously [50,100] (denoted 'conventional' MRI endoscopy), was applied at 0.3 fps to provide an unaccelerated reference for comparison

(FOV=45 mm; resolution=200 μm; FA=10°; TR/TE=15/6.61 ms; 3.34 s/frame). The duration of each endoscopy stream was ~30 s. 3D high-resolution 'static' images were also acquired at locations of interest (BIR-4 GRE; FOV=45 mm; resolution=200 μm; phase encoding steps, PE=225; FA=10°; TR/TE=100/6.61 ms; SL=2 mm; 16 slices; scan time=6.1 min).

Human iliac artery segments were studied with real-time MRI endoscopy at 6fps and 10fps (FOV=40 mm; resolution=220 μm; FA=10°; TR/TE=11/6 ms; projections/frame=15 for 6 fps (165 ms/frame), or 9 for 10 fps (99 ms/frame); pullback rate = 4 mm/sec) and with fully-sampled conventional MRI endoscopy (FOV=40 mm; resolution=220 μm; PE=182; FA=10°; TR/TE=13/5.55 ms; 2.37 s/frame) for comparison. The locations of suspected vessel lesions were identified and static 3D high-resolution MRI was then performed at these locations (BIR-4 GRE; FOV=50 mm; resolution=100 μm; FA=10°; TR=20 ms; TE=10.1 ms; SL=2 mm; 16 slices; scan time=1.9 min). The vessels were then removed and dissected at image locations, fixed, and Movat-stained for histology.

4.2.3 *In Vivo* Experiments

In vivo studies were performed with the MRI endoscope in the IVC of anaesthetized 50 kg female Yorkshire pigs (Figure 4.1d, e). The IVC was accessed percutaneously via the femoral vein under X-ray fluoroscopy guidance in studies approved by our Institutional Animal Care and Use Committee. During MRI endoscopy, an operator at the MRI scanner bore-opening, retracted the endoscope continuously as the image stream was displayed in real-time on the console monitor (Figure 4.1f). A portable in-room console was available for monitoring or adjusting sequences. IVC endoscopy

was performed at 300 μm resolution using the 6 and 10 fps accelerated sequences (FOV=40 mm; resolution=220 μm; FA=10°; TR/TE=11/6 ms; projections/frame= 15 for 6 fps (165 ms/frame), or 9 for 10 fps (99 ms/frame); pullback rate = 4 mm/sec), and with the 0.3 fps fully-sampled 'conventional' sequence (FOV=40 mm; resolution=220 μm; PE=182; FA=10°; TR/TE=13/5.55 ms; 2.37 s/frame).

4.2.4 Image Evaluation

To correlate dynamic endoscopy series acquired at 0.3 fps, 6 fps and 10 fps with static 3D reference scans acquired from the same samples, the structural and temporal information in the highly accelerated image streams is compared with fully sampled MRI endoscopy scans using image similarity metrics and with tissue dissections and histology. For this purpose we used the Mutual Information (MI) and the Structural Similarity Index (SSIM) [129,130], along with processing procedures that register image series spatially/temporally and gauge inter-frame smoothness.

Mutual Information and the Structural Similarity Index

Mutual information is a widely used criterion for aligning multi-modal medical images (CT, MRI, PET, etc.) describing the amount of information shared by two images of different contrast characteristics [129] or as here, 3D 'static' reference scans acquired with different scan protocols. In this study, MI of two images A and B were calculated as

$$\begin{aligned} \mathrm{MI}(A,B) &= \mathrm{H}(A) + \mathrm{H}(B) - \mathrm{H}(A,B) \\ &= \sum_a \sum_b p_{AB}(a,b) \log \frac{p_{AB}(a,b)}{p_A(a) p_B(b)} \\ &= \sum_a \sum_b \frac{\mathrm{h_{AB}(a,b)}}{\mathrm{N}} \log \frac{\mathrm{h_{AB}(a,b)}}{\mathrm{h_A(a) h_B(b)}} + \log \mathrm{N} \end{aligned} \tag{4.1}$$

where H(X) is the entropy of image X; $p_{AB}(a, b)$ is the joint probability distribution of pixel values; $p_A(a)$ and $p_B(b)$ are marginal probability distributions; $h_{AB}(a, b)$ is the joint histogram; $h_A(a)$ and $h_B(b)$ are histograms of each image; N is the number of pixels in each image. The metric normalized for the number of pixels is

$$\frac{2MI(A,B)}{H(A)+H(B)} \in [0,1] \tag{4.2}$$

The structural similarity index measure (SSIM) is a perception-based measure of similarity of two images for quantifying quality degradation [130]. The three-component weighted SSIM (3-SSIM) better correlates with perception by emphasizing edge regions of features vs. smooth regions [131]. This is better-suited to endoscopy where most information is concentrated within the focus vs. the large uniform area around the periphery. In the present study 3-SSIM was calculated using the procedure described in [131].

Image Streams Spatial and Temporal Registration

In this study, the reference 3D endoscopy images had different contrast from the 2D endoscopy scans. The MI was used to register the reference scan and endoscopy streams acquired at different frame rates, both spatially and temporally.

As illustrated in Figure 4.4, the foregrounds of two images acquired from different streams of the same sample were determined by brightness thresholding. Then the foregrounds were translated within a search range to discover corresponding landmarks from which the MI is maximized. After registering spatially each pair of images from the two streams, a mutual information matrix $MI \in R^{n_1 \times n_2}$ was formed, wherein n_1 and n_2 were the number of image frames in each stream, respectively. The curve formed by the

maxima of the MI in the matrix determined the temporal correspondence between the streams (Figure 4.5).

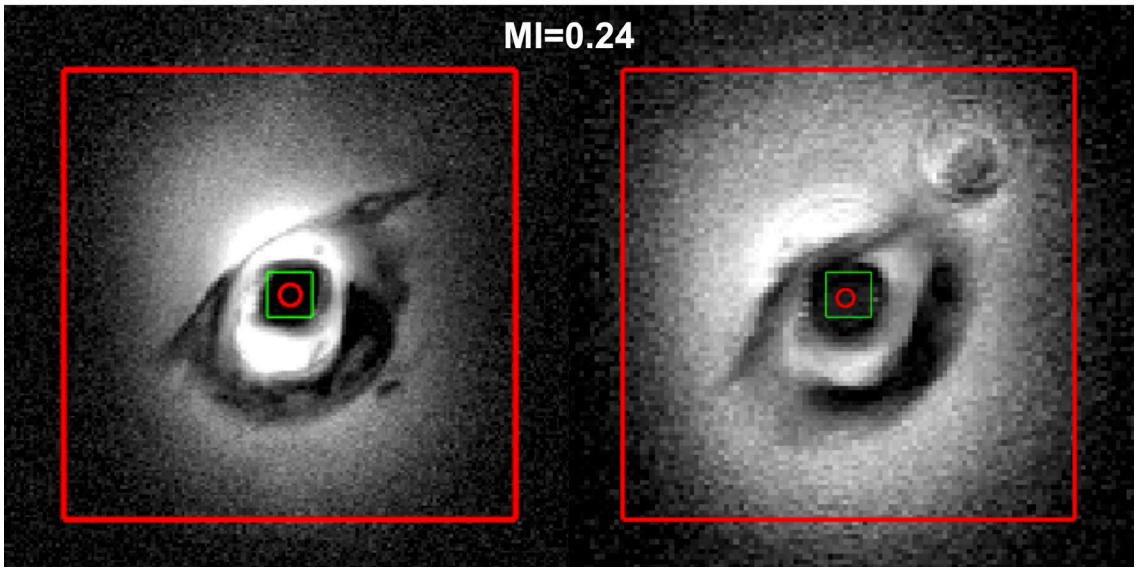

Figure 4.4 Left: image from a 3D static reference scan. Right: image from a 0.3 fps fully-sampled dynamic endoscopy scan. Red boxes show foreground patches. Green boxes are search region (5 mm square) for translation. Red circles are corresponding landmarks found for registration.

Inter-frame Transitions in Real-time Endoscopy

To quantify the continuity of real-time image streams, the change of the location of the coil was treated as a vector over time. Considering scans from the same sample wherein the coil starts at location $\overrightarrow{L_0}$ and ends up at $\overrightarrow{L_T}$, we have:

$$\overrightarrow{L_T} = \int_0^T \overrightarrow{\Delta L_t} dt + \overrightarrow{L_0} \tag{4.3}$$

Assuming that real-time scans of the same sample follow similar paths, the average magnitude of $|\overrightarrow{\Delta L_t}|$ is inversely proportional to the smoothness of inter-frame transitions. The average inter-frame translation distance (ΔL) of the center was calculated for 6fps and 10fps streams. The center of the foreground was determined by taking the weighted center of pixel values. The average translation distance was thus calculated as

$$\Delta L = \frac{1}{T-1}\sum_{t=2}^{T}\sqrt{(x_t - x_{t-1})^2 + (y_t - y_{t-1})^2} \qquad (4.4)$$

where x_t and y_t are coordinates of foreground center of the frame at dynamic t; and T is the number of frames in the image stream.

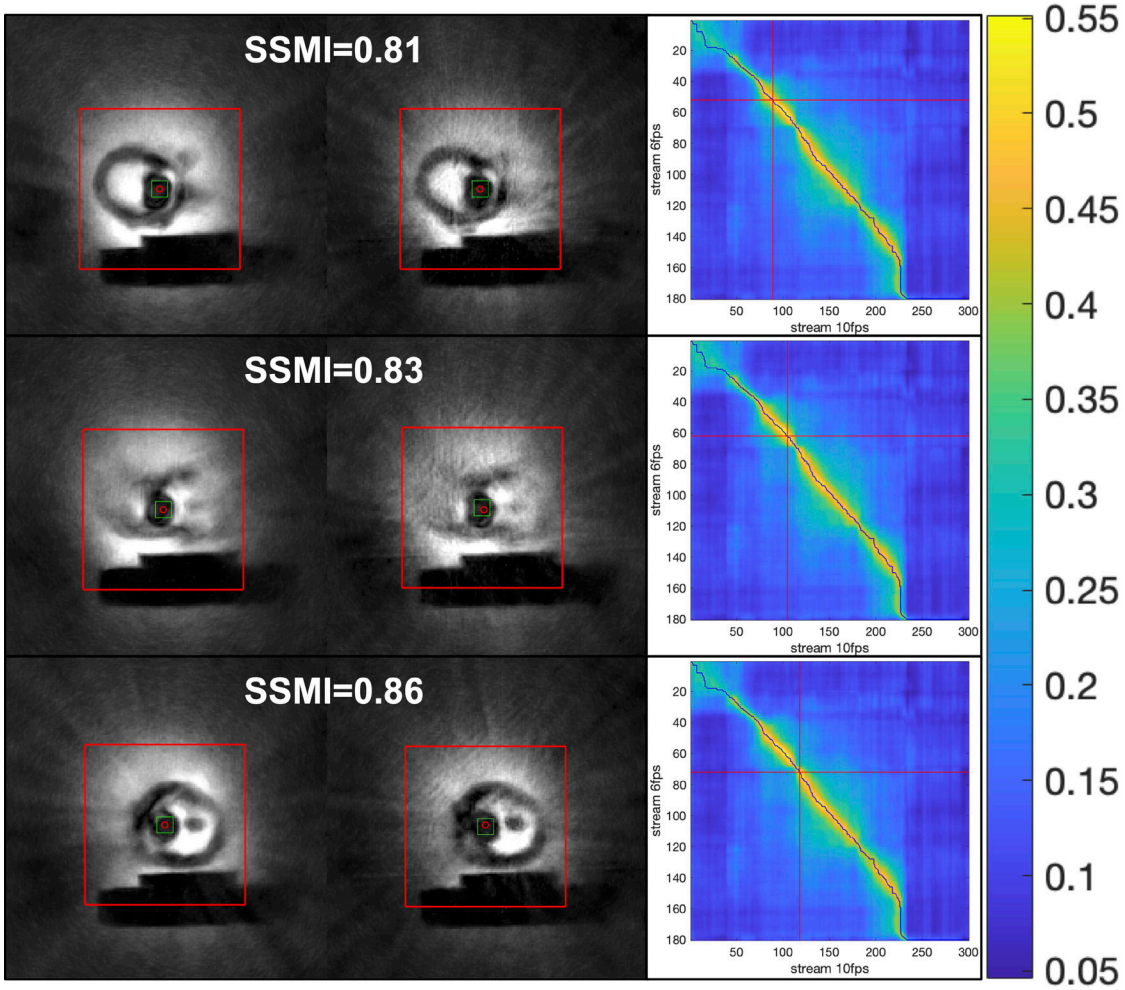

Figure 4.5 Examples of three dynamic scans from 6 fps (left column) and 10 fps (middle column) real-time endoscopy data streams from an iliac artery when the coil transitions from a side branch (Figure 4.2d) into the main lumen (top row: start transition; middle row: between the two lumens; bottom row: main lumen). Color maps (right column) show corresponding locations in the MI matrix of the temporally registered dynamics (vertical axis: dynamic indices of the 6 fps stream; horizontal axis: dynamic indices of the 10 fps stream). The blue (roughly diagonal) curves trace the MI maxima; the red cursor crosses show the specific image pairs exemplified on the left (top row: #52 vs. #89; middle row: #62 vs. #104; bottom row: #72 vs. #118).

Image Streams Comparison with the Metrics

The MI of each dynamic frame was determined for each static (3D) reference image slice, and the dynamic frame with the largest MI assigned to that reference location. The average MI for each dynamic endoscopy series at each frame rate as compared to the reference scans, was then computed for each series. The structural similarity of real-time endoscopic images acquired at 6 fps and 10 fps was compared with the 0.3 fps conventional endoscopy images by first registering them based on the maximum MI as above. The average 3-SSIM (range, [0,1]) [130,131] was then computed. The 3-SSIM of the 10 fps vs. the 6 fps scans was calculated similarly. Potential sensitivity to motion was compared by computing the average ΔL between adjacent frames of the 6 and 10 fps data streams Equation (4.4).

MI, 3-SSIM, and ΔL were determined for 11 samples (4 porcine vessels and 7 diseased human vessels) from which 3 dynamic scans (0.3 fps, 6 fps and 10 fps) and one static (3D) reference scan were acquired. MI was compared using two-way analysis of variance (two-way ANOVA) with frame rates and samples as independent variables. Multiple comparisons of different frame rates were performed using Tukey's honest significance test. Differences between 3-SSIM at 0.3 fps, and ΔL at 6 and 10 fps were assessed by paired t-testing. The apparent SNR was calculated in the accelerated scans from the quotient of the average signal in a 1 cm square centered on the endoscope, and the SD of background noise measured in a 0.5 cm square 1.5 cm from the center.

4.2.5 Preprocessing Filter

A simple inverse radial spatial filter was used in prior work to compensate for the approximately inverse-radial (1/r) coil sensitivity profile of endoscopic MRI

detectors [50]. Here, the NLINV reconstruction removes most of the undersampling artifacts [122] without such correction. However, the highly nonuniform sensitivity profile can suppress some of the useful information in the peripheral FOV during downstream reconstruction. We found that preprocessing the projection data to provide a slower-varying coil sensitivity profile improves image homogeneity, contrast and conspicuity. As the raw (inverse FT) data is an integral of the signal along the projection path, a heuristic preprocessing filter was designed to support the underlying solenoidal detection sensitivity of the endoscope, with the correction profile:

$$f(r) = \int_{-d/2}^{d/2} dx \Big/ \int_{-d/2}^{d/2} \frac{1}{x^2 + r^2} dx = \frac{\sqrt{R^2 - r^2}}{\log\left|\frac{R + \sqrt{R^2 - r^2}}{r}\right|} \tag{4.5}$$

where r is the distance to the coil center, R is the coil's sensing range, and $d = 2\sqrt{R^2 - r^2}$.

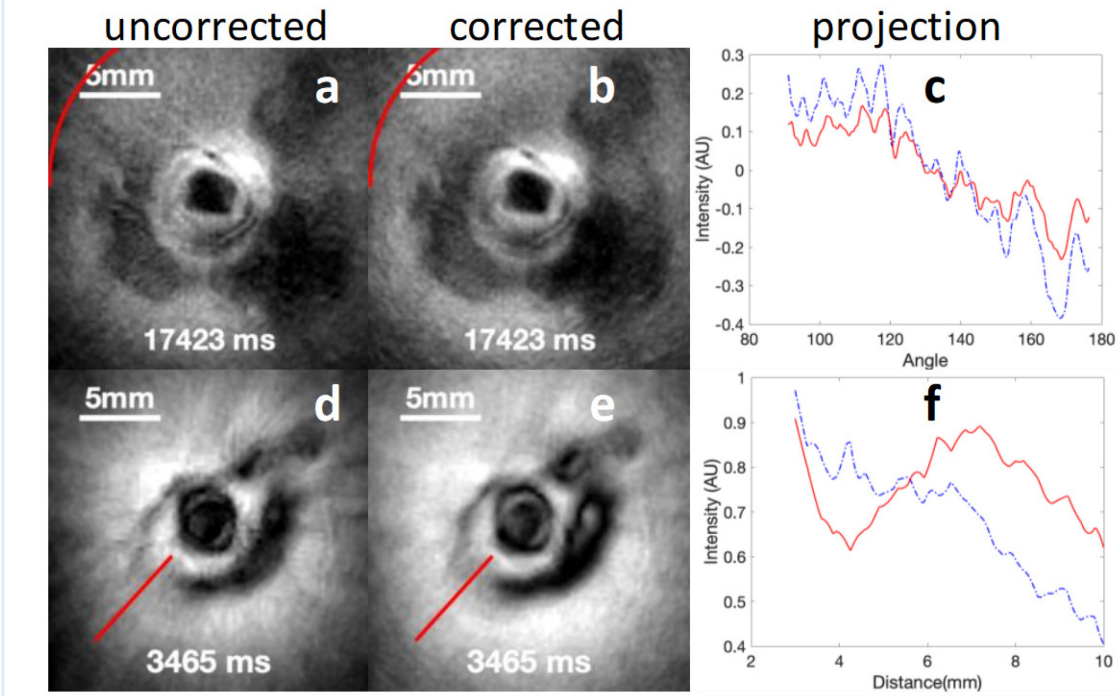

Figure 4.6 Example of image frames from 6fps porcine carotid (a, b) and human iliac (d,e) specimens without pre-filtering (a, d) and after applying Equation (4.5) (b, e). Part (c) plots image intensity vs. polar angle around the arcs indicated in red in the images. These plots shows a reduction in peripheral angular fluctuations associated with radial spokes in the pre-filtered image (red) vs. no filter (blue). Part (f) shows the improvement in uniformity in the radial dimension afforded by pre-filtering (red curve vs. blue curve).

The filtered projection data are fed to the GPU bypass computer and acceleration unit for reconstruction with the NLINV program. Examples of images in Figure 4.6 with and without the Equation (4.5) pre-filter correction show a reduction in both the angular intensity fluctuations and the radial decline in signal sensitivity (Fig. 4c,f). Endoscopy videos (Appendix A: MRI Endoscopy Videos) with and without filtering are included for side-by-side comparisons.

4.3 Results

Figure 4.7 shows endoscopic image frames from a pig carotid artery specimen in an 0.35% saline phantom at 200 µm nominal (in-plane) resolution. Frames in rows a1-a4

were recorded using highly under-sampled radial acquisitions at five different positions at 6 fps and visualized in real-time. Frames b1-4 were recorded in real-time from approximately the same locations but at 10 fps. These are respectively 20 and 33 times faster than 0.3 fps 200µm resolution images acquired using a 'conventional' fully-sampled endoscopy sequence depicted in frames c1-4, with a minimum latency period being one frame. Access information for videos of the image streams can be found in Appendix A: MRI Endoscopy Videos. Figure 4.7 (d, e) shows a 'static' fully-sampled 3D endoscopic image acquired in 368 s at the same nominal resolution as a reference. Figure 4.7 (f) shows a vessel dissection.

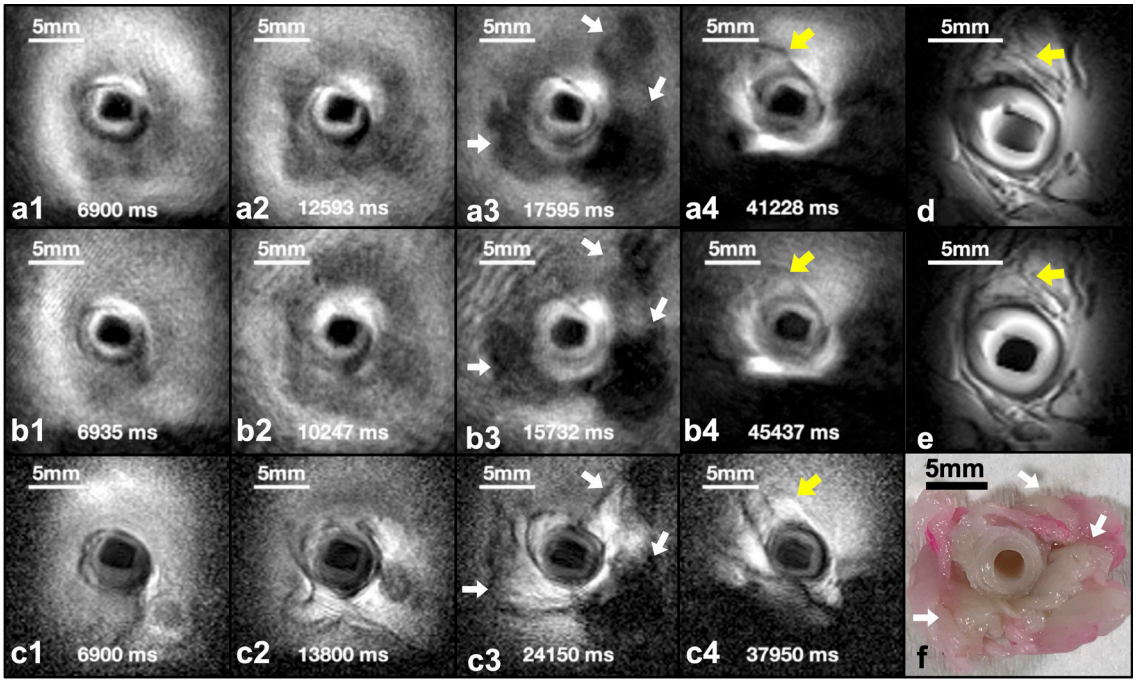

Figure 4.7 MRI endoscopy of a porcine carotid artery *ex vivo*. Imaging frames at 6 fps (a1-4) and 10 fps (b1-4), and from a fully-sampled 0.3 fps MRI endoscopy (c1-4) acquired at approximately the same locations. Access for videos are provided in Appendix A: MRI Endoscopy Videos. (d and e) High-resolution 'static' 3D endoscopic images at the location of the 4th column. (f) Dissection at location of the 3rd column. (white arrows, adipose; yellow arrows, attached tissues).

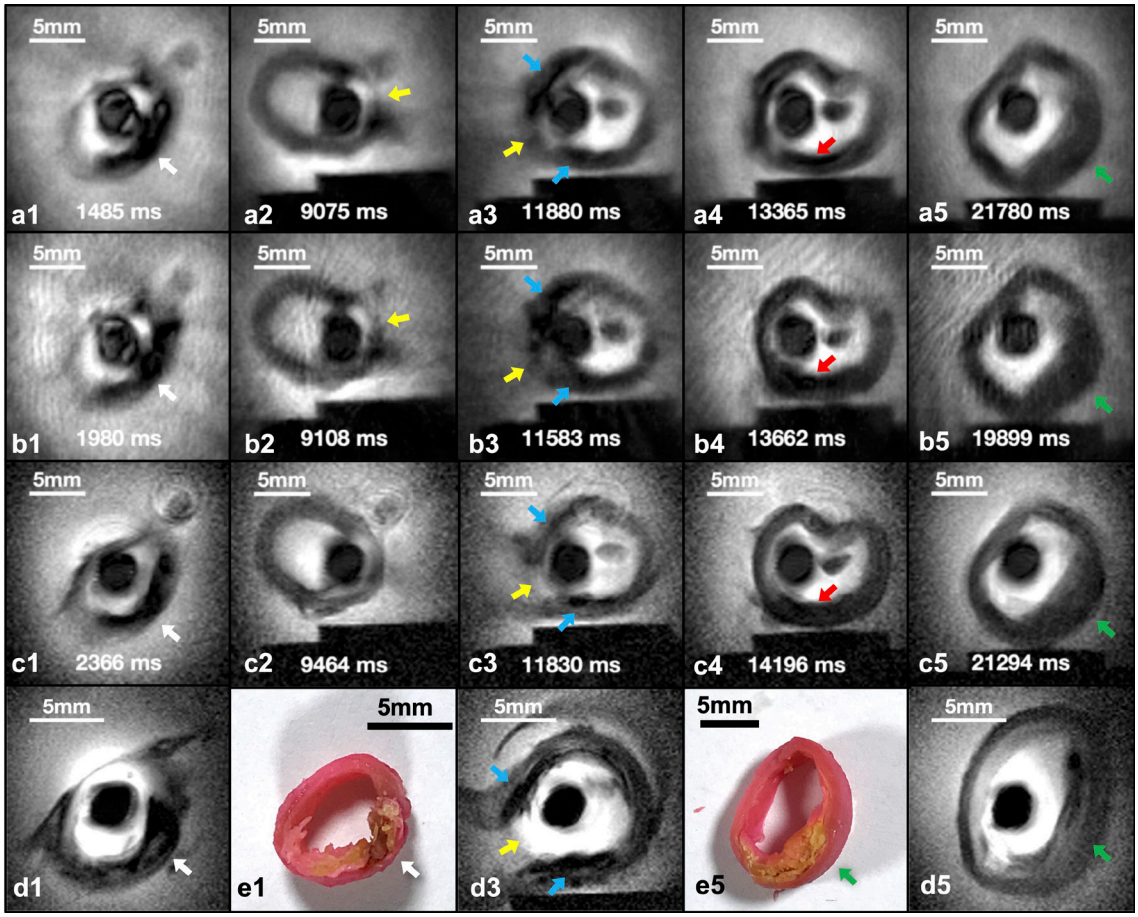

Figure 4.8 MRI endoscopy of a diseased ex vivo human iliac artery. Image frames from 6 fps (row a) and 10 fps (row b) real-time scans, 0.3 fps fully-sampled endoscopy stream (row c) and high-resolution static 3D endoscopic reference scans (row d) at approximately the same locations transitioning from a branch to the main lumen (see Figure 4.2d). The vessel wall opens at the transition (yellow arrows in a2, a3, b2, b3, c3 and d3). Access for videos are provided in Appendix A: MRI Endoscopy Videos. Each column of images corresponds to approximately the same locations except the vessel wall dissection in e1 corresponds to d1 and e5 corresponds to d5. Fibro-calcific plaque (white, blue, red and green arrows) and intimal thickening (green arrow) were identified by Movat-staining on histology of the sections.

Figure 4.8 presents images from a diseased human iliac artery specimen obtained from our institution's autopsy service, immersed in saline. Each column derives from approximately the same locations. Frames in row a and row b were sequentially acquired in real-time using highly under-sampled 220 µm endoscopy sequences at 6 fps and 10 fps, respectively. As the endoscope is withdrawn through the artery, the branching of

the internal iliac (see Figure 4.2d) is seen as a lateral opening in the vessel wall (Figure 4.8-a2, a3, b2, b3; yellow arrows). Videos of these image streams plus a 0.3 fps, 220 µm 'conventional' fully-sampled endoscopy stream 20-33 times slower can be found in : MRI Endoscopy Videos. Images in row c are reference scans from fully-sampled 0.3 fps endoscopy stream, and those in row d derive from high-resolution (nominally 100 µm) static 3D endoscopic images acquired in 112 s. Post-study dissections of the vessel wall in e1 and e5 show atherosclerosis with fibrocalcific plaques and intimal thickening corresponding to images d1 and d5, respectively.

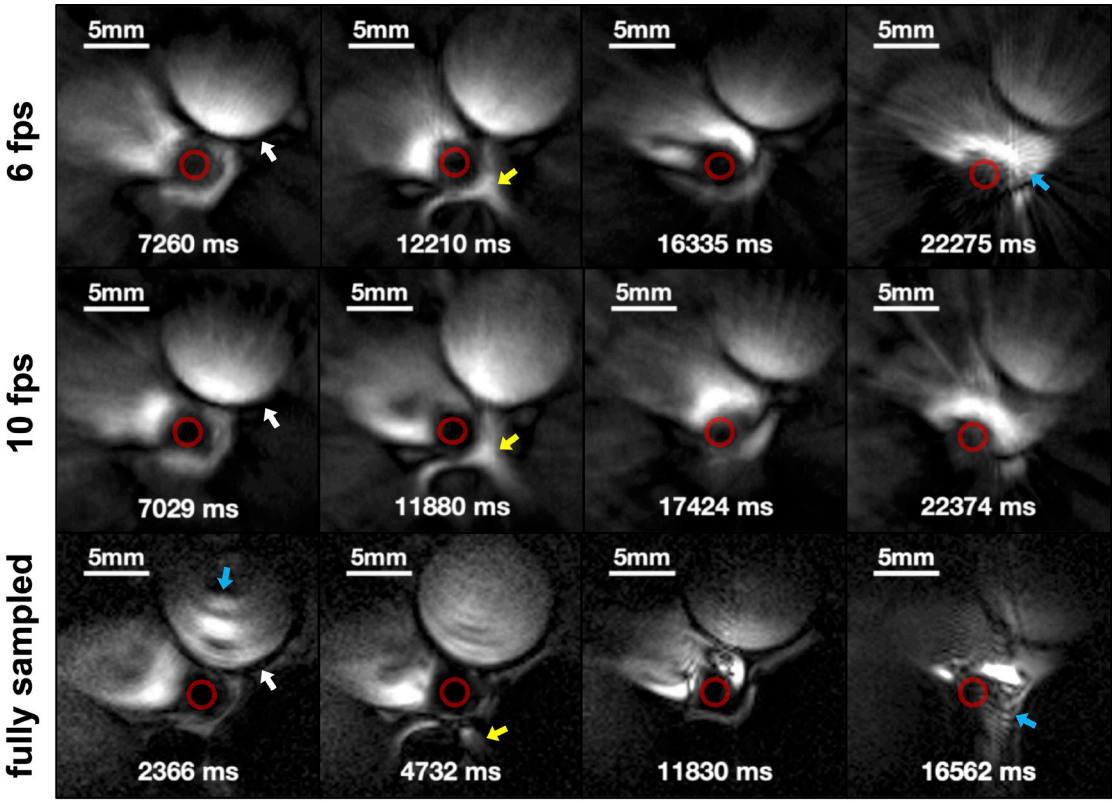

Figure 4.9 MRI endoscopy frames from a porcine IVC in vivo. Row 1, 2, and 3 were acquired at 6 fps, 10 fps and fully-sampled at 0.3 fps. Images in each column are in approximately the same location (white arrows, the aorta abutting the IVC; yellow arrows, structures near the spine; red circles: coil positions; blue arrows, motion artifact in the slower scans)

In vivo MRI endoscopy frames from a pig inferior *vena cava* are shown in Figure 4.9: the endoscopy streams can be found in : MRI Endoscopy Videos as well. The top two rows of images were acquired using under-sampled 6 fps and 10 fps endoscopy, 20 and 33 times the speed of the fully-sampled 0.3 fps images shown in the third row. The nominal spatial resolution was 220 μm and each column of images is from approximately the same location for comparison.

The MI and 3-SSIM metrics used to compare the similarity between the high-speed 6-10 fps (200-300 μm nominal resolution) highly-undersampled images and the slow 'conventional' fully-sampled scans are summarized in Table 4.1. The results are from 11 samples (4 porcine vessels and 7 human diseased vessels) acquired with 3D MRI (100-200 μm nominal resolution; 50-370 s scan-time) and fully-sampled endoscopy at 0.3 fps (200-300μm nominal resolution). Two-way ANOVA analysis show significant differences in MI between the high-resolution static 3D reference scans acquired in 50-370 s which used Cartesian spatial encoding, and the 0.3-10 fps dynamic scans acquired with radial encoding ($p<0.001$). However, while the fully-sampled 0.3 fps method outperformed the 6-10 fps highly undersampled scans ($p<0.001$), the 20 to 33-fold acceleration incurred only an ~7% cost to MI. The 3-SSIM metric, which reflects degradation in image contrast and emphasizes structural errors of perceptual significance [130,131], was only slightly better at 6 fps than at 10 fps (57 vs. 55; Table 4.1) using the 0.3 fps scans for reference. These results suggest little loss of fidelity at the higher scan rate.

Table 4.1 Comparison of image similarity indices

Metric	0.3 fps	6 fps	10 fps
MI (vs. 3D 50-370 s reference)	25.8±4.1	23.8±2.9*	24.2±3.1*†
3-SSIM vs. 0.3 fps	—	57.3±10.4	55.1±9.7§
3-SSIM vs. 6 fps	—	—	68.0±10.8
ΔL(mm)	—	0.34±0.20	0.28±0.14$^{\#}$

Values are means±standard deviations (SD). MI and 3-SSIM are in %. * $p<0.001$ vs. 0.3 fps scans (two-way ANOVA, degrees of freedom of frame rates=2). †Not significantly reduced vs. 6 fps scans. $^{\S}p<10^{-5}$ vs. 6 fps scans (paired t-test). $^{\#}$ $p=0.03$ vs. 6 fps (paired t-test).

As a gauge of motion sensitivity, a comparison of the average frame-to-frame displacement of the endoscope, ΔL showed an 18% reduction at 10 fps vs. 6 fps ($p=0.03$). The apparent image SNR in a 1-cm square centered on the endoscopy coil was 15±3 averaged from the 11 real-time endoscopy samples recorded at 6 fps and at 10 fps.

4.4 Discussion

This work demonstrates for the first time that the speed of MRI endoscopy can be increased twenty- to thirty-fold to 10 fps and visualized in real-time on a clinical 3T MRI scanner using high-speed highly-undersampled MRI radial acquisition, highly-parallelized GPU-based reconstruction, and a transmit/receive device moving independent of the scanner's frame-of-reference. Undersampling was previously proposed as a means of accelerating MRI endoscopy [52]. However, it could only be done on retroactively-acquired, fully-sampled data, and the iterative reconstructions took minutes to complete, resulting in a process that was incompatible with any practical endoscopy application. The present results are five times faster than prior best efforts at real-time endoscopy [100]. The advance here was achieved using stand-alone hardware developed for real-time MRI that connected to the scanner via a simple ethernet cable [122], and a modified MRI pulse sequence that replaced slice selection with

adiabatic excitation to provide imaging from the viewpoint of the coil at the endoscope's tip. The MRI frame-rates of 6-10 fps are comparable to X-ray fluoroscopy rates of 7.5-15 fps, and are faster than a 4 fps fluoroscopy rate recently advised for mitigating radiation dose [132] which is not an issue for MRI. Our MRI endoscopy frame-rates are also comparable to the 2-10 fps rates used in optical gastro-intestinal endoscopy procedures [133,134]. MRI endoscopy enabled continuous real-time feedback to guide catheter passage through blood vessels *ex* and *in vivo*. It could thus serve as a value-added complement or alternative to diagnostic or interventional X-ray catheterization, optical endoscopy and IVUS procedures, benefitting from MRI's advantages of soft-tissue sensitivity, lack of ionizing radiation, and the ability to see through vessel contents and vessel wall uncompromised by calcifications, as compared to optical and IVUS methods.

Highly-accelerated, under-sampled, real-time MRI endoscopy is not artefact- or cost-free, however. Our analysis showed that highly-undersampled real-time MRI endoscopy can achieve ≥20 times the frame-rate of conventional fully-sampled endoscopy at a cost of a ~7% reduction in mutual information. Compared to the fully-sampled experiments, there was no significant difference in MI between 6 and 10 fps. However, comparing the 3-SSIM with 0.3 fps scans in 10 fps vs. 6 fps revealed a small difference likely attributable to an increase in undersampling 'spoke' artifacts at the higher speed (compare Figure 4.7b and Figure 4.8b with Figure 4.7a and Figure 4.8a). Nevertheless, 10 fps, provided smoother frame transitions and less sensitivity to motion than 6 fps, with a reduction of about 18% in the frame-to-frame displacement (ΔL) to a value (0.28 mm) commensurate with the spatial resolution, and comparable to the

increase in speed. Note that spoke artefacts were attenuated and conspicuity was improved in the peripheral FOV using a simple analytical preprocessing filter applied to the raw projection data, which better compensated for the extreme inverse-radial (1/r) inhomogeneity of the endoscopic coil and downstream NLINV reconstruction (see 4.2.5 Preprocessing Filter). Note also that while the comparative metrics were averaged from 11 sets of cine streams, a caveat is that they all derive from images acquired at different rates and times from vessel transits that are unlikely to follow exactly the same track or sample the exact same locations due to the very nature of endoscopy. Thus, a perfect MI or SSIM cannot be expected.

Surprisingly perhaps, the difference in artefacts at 6 fps versus 10 fps is less obvious *in vivo* (Figure 4.9) than *ex vivo* (Figure 4.8). This may reflect a trade-off between the improved ability to freeze physiological motion in the living animal at higher speeds, offsetting the increase in spoke artefacts at the higher frame rate. Still, moving the probe too fast or nonuniformly within the frame acquisition period (jerking or changes in catheter-sheath friction, etc.), is liable to cause 'glitches' of intense spoke artifacts from the afflicted projections (annotated in the appendix videos). The effect is not uncommon to other intravascular imaging modalities wherein glitches are ignored or the frames automatically dropped from the imaging stream. Nevertheless, there is certainly room to improve artifact suppression. Indeed, the hyper-intense radial artifacts resemble metallic artifacts in X-ray CT images which have been addressed using data-adaptive artifact-reduction algorithms [135,136] that might be adaptable here. Meanwhile, given the real-time feedback at our frame rates, the MRI operator can just pause in advancing the endoscope, whereupon replacement images will appear in very

short order. By comparison, the much slower speed of fully-sampled MRI endoscopy renders it prone to artifacts from motion occurring during the acquisition of each image frame, even when the probe is not being advanced (Figure 4.9). When motion is paused at locations of interest, more projections can always be acquired at high speed to improve spatial—at the expense of temporal—-resolution. A regular high-speed mode can be resumed as soon as the probe is advanced further or retracted.

A characteristic of MRI endoscopy is the highly nonuniform excitation field (B_1) around the endoscopic coil when it is used for transmission and–by the Principle of Reciprocity–its highly non-uniform sensitivity when deployed as a receiver (Figure 4.3). Both of these properties are used to localize the endoscopy coil first by enabling the elimination of MRI slice selection–which is normally fixed to the scanner frame of reference; and second by reducing the effective FOV and hence the number of spatial encoding steps or projections needed for imaging. The adiabatic (BIR-4) pulse maintains a uniform MRI flip angle inside this effective FOV, which may be defined as the volume of tissue ('sensitive disk'; Figure 4.3a) enclosed by the B_1-contour that corresponds to the pulse's threshold for adiabaticity. Outside of this B_1-threshold, the FA fades rapidly to zero. MRI endoscopy requires two independent adjustments of the pulse. First, the B_1 amplitude sets the spatial extent of the sensitive disk (Figure 4.3b); and second, the pulse's internal phase is adjusted to set FA within the FOV to optimize the SNR and the desired image contrast (Figure 4.3c). Regarding the latter, the use of the endoscopy coil for excitation; the use of adiabatic pulses to combat the non-uniform B_1; and the focus on speed to facilitate MRI endoscopy applications analogous to those of other modalities; are all confounding factors for adjusting MRI contrast by conventional means while the

endoscope is moving. The efficacy of adding a FA=180° pulse to generate MRI relaxation-time (T_1) contrast, for example, depends on the speed that the probe advances to locations outside the range of the 180° pulse. With the probe stationary, however, MRI relaxation times *can* certainly be quantified using conventional or accelerated approaches [10].

The primary safety concern for internal devices is the localized heating induced by MRI's radio frequency (RF) pulses, which is not well-gauged by the volume-averaged RF specific absorption rates used for general MRI [137,138]. With an FOV of ~20 mm (Figure 4.3b; Tx≤7.8 V) local tissue heating during endoscopy at the stated scan-rates was ≤0.5 °C, in accordance with prior studies showing no significant heating or thermal injury [50,100]. When the FOV was increased to ~30 mm by increasing B_1 amplitude (Tx=18.8 V), a local temperature rise of 3.5 °C was recorded after continuously streaming 600 images from a single location. However, heating at the higher power level is reduced with the endoscope unfixed and moving through a local perfused volume such as a blood vessel. The maximum temperature rise is localized in the immediate vicinity of the coil [50,100] and can also be monitored by high-resolution MRI thermometry performed using the endoscope [5,51].

In conclusion, high speed MRI endoscopy, unlocked from the scanner frame-of-reference, can be combined with undersampling and real-time image reconstruction technologies to match the speed of existing clinical catheterization and endoscopy procedures and could provide a useful complement to established minimally-invasive imaging modalities including X-ray fluoroscopy, IVUS, OCT and optical endoscopy [139]. It has the potential advantages of multifunctional imaging afforded by

MRI, including thermal imaging for monitoring trans-vascular [51] and perivascular ablation therapies [5], and parametric imaging for classifying vessel disease as demonstrated previously [10]. The main hurdles to the technology are primarily those associated with interventional MRI in general: its expense, the limited availability of scanners in interventional settings, and accessibility to patients, interventionalists, recovery facilities and expertise in interventional MRI.

Chapter 5: Ultrafast compartmentalized relaxation time mapping with linear algebraic modeling

5.1 Introduction

The image contrast afforded by tissue longitudinal (T_1) and transverse (T_2) relaxation times [140,141] is central to MRI's success in the clinic. The standard way of measuring MRI relaxation parameters is to acquire sets of images as a function of time as the NMR signal in each pixel returns towards equilibrium. However, the limited scan-time available for clinical studies often precludes the acquisition of such image data. Consequently, T_1- and T_2-weighted images are routinely used in clinical protocols whereas quantitative T_1 and T_2 maps are not.

Although more efficient methods than the standard inversion recovery (IR) and multi-echo spin echo (MESE) sequences for mapping T_1 and T_2 values abound [31,142–151], arguably, the IR and MESE sequences remain the gold standards for accurate T_1 and T_2 measurements and for validating newer faster methods. Nevertheless, in numerous applications, local average ROI measurements can suffice–as in T_2-based monitoring of treatment response in brain tumors [152], or the use of blood T_1 to quantify cerebral blood flow [153]. Indeed ROI-based analyses are ubiquitous in MRI [154–156]. However, averaging voxel values for ROI measurements post-acquisition comes at a cost to the SNR about equal to the square-root of the number of voxels being averaged, as compared to encoding the whole ROI directly [157]. In addition, much time is wasted in encoding fine resolution that ROI averaging abandons. The time spent encoding and the lost SNR could better be spent on reducing scan time by directly encoding ROIs that provide compartment-average relaxation measurements from the outset.

The SLAM method was recently proposed to directly encode ROI-average spectra from arbitrarily-shaped, user-defined compartments [53,157–159]. The method provided dramatic acceleration factors of 4 to 120-fold plus SNR efficiency gains as compared to fully-sampled scans acquired with conventional one-, two-, and three-dimensional (1D, 2D, 3D) encoded spectroscopy (MRS). However, SLAM need not be limited to MRS. It can directly map any ROI-average MRI signal or relaxation parameter derived therefrom in the set of compartments that include all of the ROIs and signal sources in an image. The minimum number of phase- and/or sensitivity-encoding steps required for the task is equal to the number of compartments.

Here, the SLAM method is applied to perform ultrafast T_1 and T_2 mapping in the phantom, abdominal and brain tumor studies using similar reconstruction formulae to those used for SLAM CEST [159]. SLAM is validated by omitting up to $15/16^{ths}$ (94%) of data acquired retroactively from IR and MESE sequences. We proactively apply it to accelerate abdominal and brain tumor T_1 and T_2 measurements by up to 16-fold in humans. Other than setting-up the MRI sequence parameters, implementing SLAM requires only the specification of the number of compartments and a scout image. Compartment segmentation is performed post-acquisition, so re-segmentation and 'trial' compartments can be implemented with the same accelerated data set. The localization properties of the two SLAM reconstruction algorithms [53,157] are evaluated using the discrete spatial response function (dSRF).

This research was led by Dr. Yi Zhang at Johns Hopkins and my role as second author primarily involved assistance with the phantom and in vivo studies and maintaining the SLAM processing pipeline and code.

5.2 Theory

5.2.1 The SLAM method

The central idea of SLAM [53,157–159] is to group voxels defined by scout MRI into compartments, and reduce the number of phase- or sensitivity-encoding gradient steps to a small subset of the original PE set. These are chosen from central image *k*-space to maximize SNR. A huge reduction in PE steps is possible because the number of unknowns is reduced from the number of image-space voxels (M; e.g., 256^2), to the number of compartments (C; e.g., 6-16). The compartmental segmentation information is built into an auxiliary matrix, $\boldsymbol{b}$ [157], which is incorporated into the standard FT reconstruction model [157], or the SENSE [20] reconstruction model [53,159]. After dimensional reduction, two algorithms have been used to reconstruct the compartmental signals, $\boldsymbol{\rho}_C^r$, involving the solution of:

$$\boldsymbol{\rho}_C^r = \left(\boldsymbol{E}_{M'*M} \times \boldsymbol{b}_{M*C}^r\right)^+ \times \boldsymbol{s}_{M'} \tag{5.1}$$

$$\text{or } \boldsymbol{\rho}_C^r = (\boldsymbol{b}_{M*C}^r)^+ \times \left(\boldsymbol{E}_{M'*M}\right)^+ \times \boldsymbol{s}_{M'} \tag{5.2}$$

where ' * ' adjoins matrix dimensions and ' × ' denotes matrix multiplication. We shall denote the two reconstructions as SLAM1 and SLAM2, respectively [53,157]. Here $\boldsymbol{E}$ is the combined phase, frequency, and sensitivity encoding matrix, $\boldsymbol{s}$ is the vectorized *k*-space raw data, + denotes Moore-Penrose pseudo-inverse, and M' is the number of known data points, equal to the product of the number of phase-encoding steps, number of frequency-encoding steps and number of receiver coil elements (N_c). Note that in the limit of $M' = \mathrm{MN_c}$, Equation (5.2) yields equivalent results to averaging the compartmental signals acquired from a fully-sampled FT (or SENSE) image. Further

details on SLAM reconstruction and the creation of the $\boldsymbol{b}$ matrix can be found in [53,157–159].

5.2.2 SLAM localization properties

The localization properties of SLAM could be analyzed using a continuous spatial response function, SRF [157,160,161]. However, when SENSE is involved, a continuous sensitivity map is required to calculate a continuous SRF [162]. Although one can be generated, for example by interpolating a discrete sensitivity map, this is not trivial and the results are prone to error [163]. Moreover, a continuous SRF typically requires a continuous underlying ground-truth signal that cannot be measured *in vivo*. Thus a discrete sensitivity map and dSRF has been used [53], which treats the spatially discrete signals reconstructed from the standard discrete FT and/or SENSE model, as ground truth. For the SLAM1 and SLAM2 algorithms, the corresponding dSRFs are respectively:

$$\mathbf{dSRF}_{C*M} = \left(\boldsymbol{E}_{M'*\mathrm{M}} \times \mathbf{b}^{\mathrm{r}}_{\mathrm{M}*\mathrm{C}}\right)^{+} \times \boldsymbol{E}_{M'*M} \tag{5.3}$$

$$\text{or } \mathbf{dSRF}_{C*M} = (\mathbf{b}^{r}_{M*C})^{+} \times \left(\boldsymbol{E}_{M'*\mathrm{M}}\right)^{+} \times \boldsymbol{E}_{M'*M} \tag{5.4}$$

The reconstructed SLAM compartment-average signal equals the product of the dSRF with the underlying pixel-by-pixel image signals from the standard FT and/or SENSE model. Thus, the dSRF characterizes the source of the signal contributions in image space.

5.3 Methods

The SLAM method requires anatomical scout images (with or without relaxation weighting) for segmenting compartments. The anatomical information is incorporated into the $\boldsymbol{b}$ matrix along with the raw *k*-space data and the coil sensitivity maps for

reconstruction, as above [53,157–159]. SLAM was validated retroactively by comparing the results from subsets of MRI data extracted from full *k*-space PE sets, with those obtained by averaging the signal from the same compartments segmented from full *k*-space images. SLAM was validated proactively by applying the accelerated, reduced-PE sequences, and comparing the results with compartment averages obtained from full *k*-space acquisitions that were acquired separately.

All MRI experiments were performed on a 3T dual-transmit *Philips Achieva* MRI scanner (*R5.1.7 software*; Best, Netherlands). All human studies were approved by the Johns Hopkins Institutional Review Board and written consent was obtained from each participant. Phantom and brain studies used a 32-channel receive head coil array. Abdominal studies used a 32-channel receive torso coil array with 16 channels in each of the anterior and posterior sets. All full *k*-space scans, SLAM and the anatomical images used for segmentation shared identical angulation parameters to facilitate image co-registration. All T_1 mapping studies employed a non-slice-selective adiabatic hyperbolic secant pulse [164] for initial IR inversion followed by a 30 ms crusher gradient. The 180^0 pulses used for readout in TSE [165] sequences were slice-selective 'sinc-center' pulses.

The raw *k*-space data for the SENSE reference scan [20] and the relaxation time mapping scans were saved for offline SLAM reconstruction with an in-house program written in *MATLAB* (*R2016a, MathWorks*, Natick, MA) on a personal (2.7 GHz) laptop computer. SLAM reconstruction took less than 2 min for all phantom, abdominal and brain studies described herein, after segmenting compartments and loading the *k*-space raw data into *MATLAB*.

5.3.1 Phantom Studies

Agarose and copper sulfate were mixed in deionized distilled water to concentrations ranging from 0 to 110 g/L, and from 0 to 1.9 g/L, respectively. The solutions were heated in a microwave oven, and poured into fifteen 3 cm-diameter, 11 cm-long tubes, to cool and gel. MRI scanning commenced with a vendor-preset SENSE reference scan [163] using the body and SENSE coils consecutively and a 3D GRE sequence [166] (FOV=450×300×300 mm; resolution=4.7×4.7×3 mm; TR=4 ms; TE=0.8 ms; FA=1°; number of averages [NSA]=3; scan duration=39 s). A single-slice scout MRI sequence was then run prior to relaxation time mapping, to localize a central transaxial plane through all tubes and to provide images for segmenting compartments for SLAM reconstruction (TSE readout; FOV=256×256 mm; resolution=1×1 mm; SL=2 mm; TR=3 s; TE=7 ms; turbo factor=16; SENSE factor=1; and scan duration=54 s).

T_1 mapping was performed using an IR sequence with eight inversion delay times (TI=50, 150, 300, 500, 800, 1300, 2000, and 4000 ms) and a 2D TSE readout (FOV=256×256 mm; resolution=1×1 mm; ST=2 mm; TR=5 s; TE=7 ms; turbo factor=16, wherein each excitation acquires 16 PE lines; SENSE factor=1; total duration=10.8 min). Two sets of proactive SLAM T_1 mapping scans were implemented using the same imaging parameters except that only 32 and 16 PE lines from the central *k*-space were acquired. This reduced the scan times to 80 s and 40 s, respectively, excluding two startup TRs for equilibration.

T_2 mapping used an MESE sequence with 32 TEs (7-224 ms; step size=7 ms), a 2D TSE readout (FOV=256×256 mm; resolution=1×1 mm; ST=2 mm; TR=800 ms;

turbo factor=32 wherein each excitation repeatedly acquired one PE line with 32 different TEs; SENSE factor=1; total duration=3.5 min). Two sets of proactive SLAM T_2 mapping scans were applied with the same parameters except that only 32 and 16 PE lines from central *k*-space were acquired. This reduced the scan times to 25.6 s and 12.8 s, respectively, excluding three startup repetitions for equilibration.

5.3.2 Abdominal Studies

Six healthy volunteers (ages, 25-36; all male) were recruited for abdominal relaxation time mapping. A RF transmit field (B_1) calibration sequence based on the actual flip-angle (AFI) method [167] with dual TRs (20 and 100 ms) was used to shim the two transmit channels for optimum B_1 homogeneity in the abdomen, followed by a 3D GRE SENSE reference scan (FOV=600×600×400 mm; resolution=5.4×7.3×4 mm; TR=4 ms; TE=0.8 ms; FA=1°; NSA=2; duration=33 s). A T_1-weighted single-shot IR-prepared GRE sequence [145] was applied to acquire sequential multiple 2D (multi-2D) images (FOV=375×298×198 mm; resolution=1.5×2×5 mm; ST=5 mm, slice gap [SG]=0.5 mm; TR=10 ms; TE=2.3 ms; FA=15°; TI=1.5 s; SENSE factor=2; duration=1.1 min). A T_2-weighted single-shot multi-2D TSE sequence was then applied (FOV=375×302×198 mm; resolution=1.3×1.6×5 mm; ST=5 mm; SG=0.5 mm; TR=805 ms; TE=80 ms; SENSE factor=2; duration=0.5 min).

T_1 mapping used an IR sequence with seven TIs (50, 150, 300, 500, 800, 1300, and 2000 ms), and a 2D TSE readout (FOV=256×384 mm; resolution=1×1.5 mm; ST=5 mm; TR=3 s; TE=7 ms; turbo factor=16; SENSE factor=1; and total duration=5.7 min) in the anterior-posterior direction to minimize artifacts from respiratory motion. T_2 mapping used an MESE sequence with 16 TEs (15-240 ms;

step size=15 ms), and a 2D TSE readout (FOV=256×384 mm; resolution=1×1.5 mm; SL=5 mm; TR=0.6 s; turbo factor=16; SENSE factor=1; total duration=2.6 min) also in the anterior-posterior direction.

Two trans-axial T_1-weighted and T_2-weighted scout images were acquired to target cross-sections of the liver and the kidney, and used to segment compartments for SLAM reconstruction. Two sets of proactive SLAM T_1 and T_2 mapping scans were then acquired from each of the targeted cross-sections, using only 32 and 16 PE lines collected from the central *k*-space of the same MRI sequences. For each of the two proactive SLAM T_1 acquisitions, the scan duration was 42 s and 21 s (excluding two startup TRs for equilibration); the SLAM T_2 acquisitions took 19.2 s and 9.6 s (excluding four startup TRs).

5.3.3 Brain Tumor Studies

Six patients with grade III astrocytomas or grade IV glioblastomas (range of ages, 34-76; three males) underwent a SENSE reference scan using identical parameters to those used for the phantom studies. Anatomical imaging sequences including FLAIR [168] with an interleaved multi-slice TSE readout (FOV=212×189×132 mm; resolution=0.83×1.04×2.2 mm; ST=2.2 mm; SG=0 mm; TR=11 s; TE=120 ms; TI=2.8 s; turbo factor=19; SENSE factor=1.5; duration=3.9 min), and MP-RAGE [169] (FOV=212×172×165 mm; resolution=1×1×1.1 mm; TR=8 ms; TE=3.7 ms; TI=805 ms; SENSE factor=2; duration=3.4 min) were performed. Because of the long time required for full *k*-space relaxation-time imaging, reference T_1 and T_2 mapping scans could not both be acquired from all patients due to tolerance and clinical management issues. Both T_1 and T_2 mapping scans were obtained from only 3 of the patients; T_1 data was acquired

from 4 patients, and T_2 data was acquired from 5. One patient had both reference T_1 and T_2 scans, as well as proactive SLAM scans.

T_1 mapping used an IR sequence with seven TI values (50, 150, 300, 500, 800, 1300, and 2000 ms), and a 2D TSE readout (FOV=224×224 mm; resolution=1×1 mm; ST=2 mm; TR=3 s; TE=7 ms; turbo factor=16; SENSE factor=1; total duration=5 min). T_2 mapping used an MESE sequence with 16 TE values (15-240 ms; step size=15 ms), and a 2D TSE readout (FOV, resolution, ST, turbo factor and SENSE factor same as for T_1 mapping; TR=0.5 s; total duration=1.9 min). Full *k*-space T_1 and/or T_2 mapping was implemented on trans-axial sections intersecting areas of the brain tumor. Proactive SLAM T_1 and T_2 mapping utilized only the 32 PE lines from central *k*-space, resulting in a 42 s T_1 scan (excluding two startup TRs) and a 16 s T_2 scan (excluding four startup TRs).

5.3.4 SLAM Reconstruction and Data Analysis

The SLAM reconstruction was implemented in the following steps:

First, to account for any size and FOV differences in the reference scout images used for segmentation, relaxation time images were co-registered to the nearest anatomical reference image based on the slice off-center locations from the image header files. The co-registered reference image was resampled and resized to match the acquisition FOV and resolution of the full *k*-space (unaccelerated) relaxation time images. Because MRIs typically undergo post-processing to correct for geometric warping due to gradient field nonlinearity [170] whereas the SLAM algorithms presently do not account for gradient nonlinearity, reference anatomical images were post-processed to obtain uncorrected images for segmentation.

Second, every voxel of the co-registered anatomical image was assigned to a compartment. For the phantom experiments, 16 compartments were defined: 15 tubes plus the background (Figure 5.1a). For the abdominal studies, 6 compartments were typically defined on T_1-weighted images with the T_2-weighted images also viewed, and included liver (avoiding major blood vessels) or kidney, spleen, muscle, fat, 'rest of the body', and background. For the brain tumor studies, typically 6 compartments were defined on FLAIR images with the T_1-weighted images also taken into consideration. These included tumor, contralateral normal-appearing white matter (CNAWM) [171], 'rest of the brain', ventricle, scalp, and background.

Third, subsets of PE lines corresponding to acceleration factors of $1 \leq R \leq 16$ were selected from the central *k*-space of the full *k*-space sequences for retroactive and proactive SLAM reconstruction. For example, the phantom experiment had 256 PE steps (from -128 to +127) for the full *k*-space T_1 and T_2 maps. Retroactive SLAM implementation with R=8 used the central PE steps from -16 to +15 taken from the full *k*-space data set. Proactive SLAM implementation with R=8 used the same PE steps from a separately acquired proactive 32-step SLAM acquisition. An exception was the proactive brain tumor study, where the central 28 PE steps from the 32-step SLAM data set were selected in order to match the R=8 used in the other studies.

Fourth, compartment-average image-space signals were reconstructed using the SLAM1 or SLAM2 algorithms, Equations (5.1) and (5.2), the selected or acquired PE lines, and the compartmental segmentation information. Compartment-average T_1 values were solved by fitting TI and absolute SLAM1 and SLAM2 $\boldsymbol{\rho}^r$ values to a 3-parameter exponential function, $\boldsymbol{\rho}^r = a - b * exp(-TI/T_1)$, with a, b and T_1 as unknowns to be

determined. Because the MRI signal magnitude was used, the inverted portion of the IR recovery curve was identified by negating either all of the $\boldsymbol{\rho}^r$ values that occurred before or which included, the minimal absolute value of $\boldsymbol{\rho}^r$ for the 3-parameter exponential fitting. The result that generated the smaller fitting residue was chosen for the final T_1 value. Compartment-average T_2 was determined by fitting TE and $\boldsymbol{\rho}^r$ values to a 2-parameter exponential function, $\boldsymbol{\rho}^r = c * exp(-TE/T_2)$, with c and T_2 as the unknowns.

The fully-sampled compartment-average T_1 and T_2 values were taken as reference standards for comparing retro- and pro-actively accelerated measurements. Pearson's correlation coefficient (r), and paired t-test or Wilcoxon signed rank test were used to test for differences between reference and accelerated values. Pooled relaxation values that passed the Shapiro-Wilk normality test underwent paired t-testing or otherwise Wilcoxon signed rank testing, with probability $p<0.05$ considered statistically significant. The percentage differences between reference and accelerated values were also calculated.

The dSRF was computed using Equations (5.3), (5.4) to compare the localization properties of SLAM with that of full *k*-space sampling. For display, compartmental average relaxation times were assigned to all pixels in each compartment and overlaid on the co-registered anatomical image.

5.4 Results

Figure 5.1 shows SLAM1 and SLAM2 T_1 reconstructions from the 15-tube phantom segmented into 16 compartments (Figure 5.1a). The full *k*-space sampling generated a perfect dSRF (Figure 5.1b) with values uniformly distributed within the target compartment that sum to 1.0 and are zero outside the compartment: the fully-sampled SLAM2 dSRF yields the same result. The SLAM2 dSRF at R=8 (Figure 5.1d) is very

similar, while the SLAM1 dSRF at R=8 (Figure 5.1c) shows some non-uniformity within the target. However, the final signal from SLAM1 and SLAM2 is not the dSRF, but the summation of the dSRF multiplied by the underlying complex image signal. The summation of the complex dSRF for SLAM1 is 1.0 over the compartment in Figure 5.1c. On the other hand, the complex dSRF of SLAM2 sums to 0.94 within the compartment in Figure 5.1d, resulting in a slightly broader profile than the perfect dSRF, despite its improved uniformity within the compartment [53]. Nevertheless, there is no difference between the full *k*-space (Figure 5.1e), SLAM2 (R=8, Figure 5.1f) and SLAM1 (data not shown) compartmental-average T_1 maps.

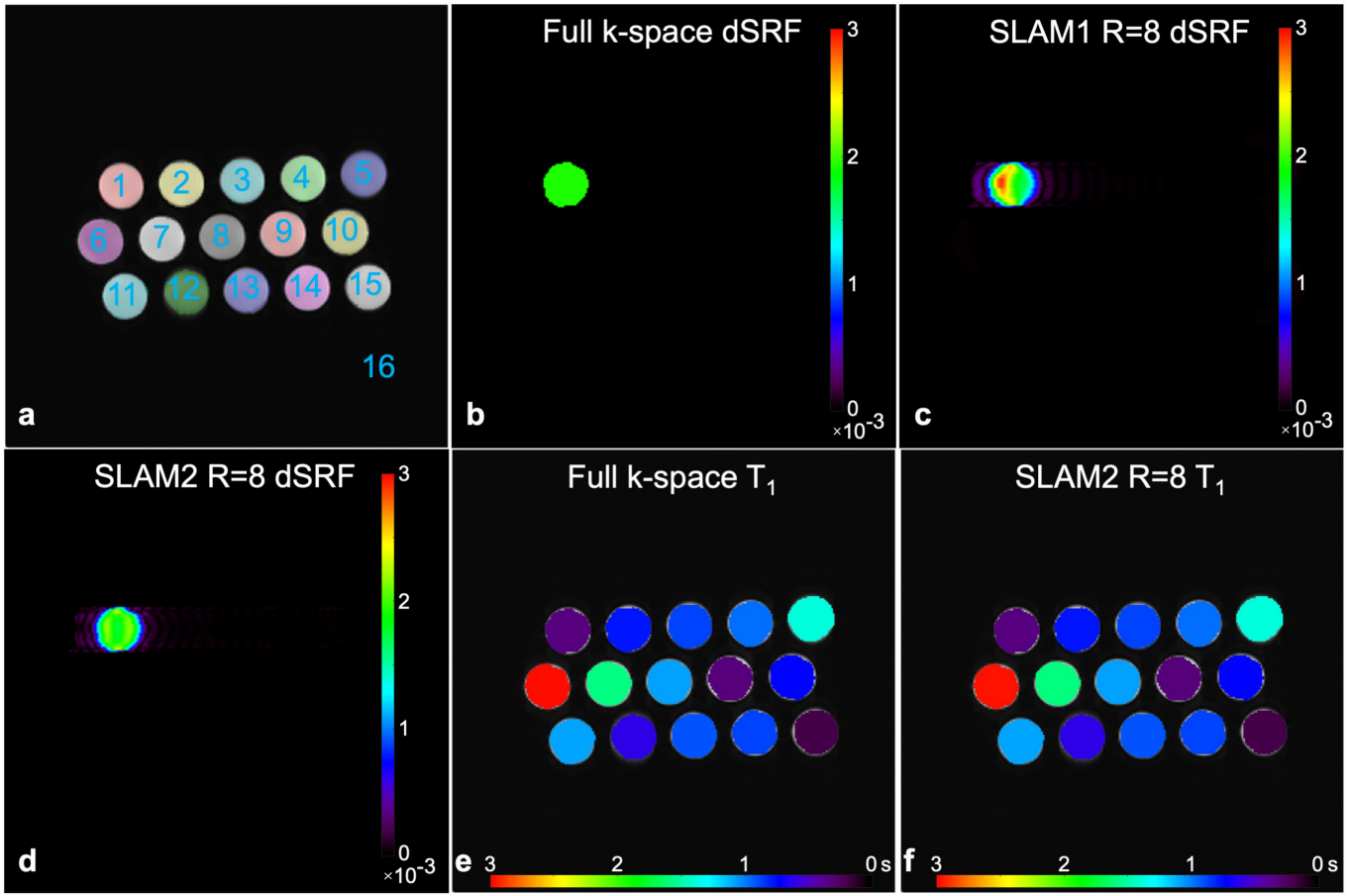

Figure 5.1 Compartmental segmentation, spatial localization properties, and compartmental T_1 maps for the phantom study. (a) Sixteen compartments (15 tubes plus background) segmented for SLAM reconstruction on a co-registered image. (b-d) Absolute dSRF for compartment 1 from a fully-sampled *k*-space (b), an 8-fold accelerated SLAM1 reconstruction (c), and an 8-fold accelerated SLAM2 reconstruction (d). Color-scale was in arbitrary units. (e-f) Color-coded compartmental T_1 maps (scale was in sec) for the standard full *k*-space (e), and 8-fold faster SLAM2 reconstructions (f).

The measured T_1 values of all tubes from the full *k*-space data sets ranged from 195–2980 ms, as shown in Figure 5.2a-d. T_1 values from both 8-fold and 16-fold accelerated SLAM1 and SLAM2 reconstructions did not differ significantly ($p \geq 0.08$) from the standard full *k*-space measurements in Figure 5.2(a-b, d), but the difference in Figure 5.2(c) is borderline significant ($p=0.04$). Figure 5.2(e-h) show that T_2 values reconstructed from both 8-fold and 16-fold accelerated SLAM1 and SLAM2 algorithms agree with the full *k*-space reference over the range T_2=12–1930 ms. In addition, there were no significant differences between SLAM1, SLAM2 and full *k*-space reconstruction ($p \geq 0.2$): mean percentage differences between the SLAM1, SLAM2, and full *k*-space reconstructions were ≤0.8%, with correlation coefficients $r \geq 0.998$ throughout. Standard deviations (SD) in mean differences were ≤3.5% for proactive and ≤0.7% for retroactive SLAM T_1 (Figure 5.3). For SLAM T_2 they were ≤4.0% for proactive and ≤4.5% for retroactive implementations (Figure 5.4).

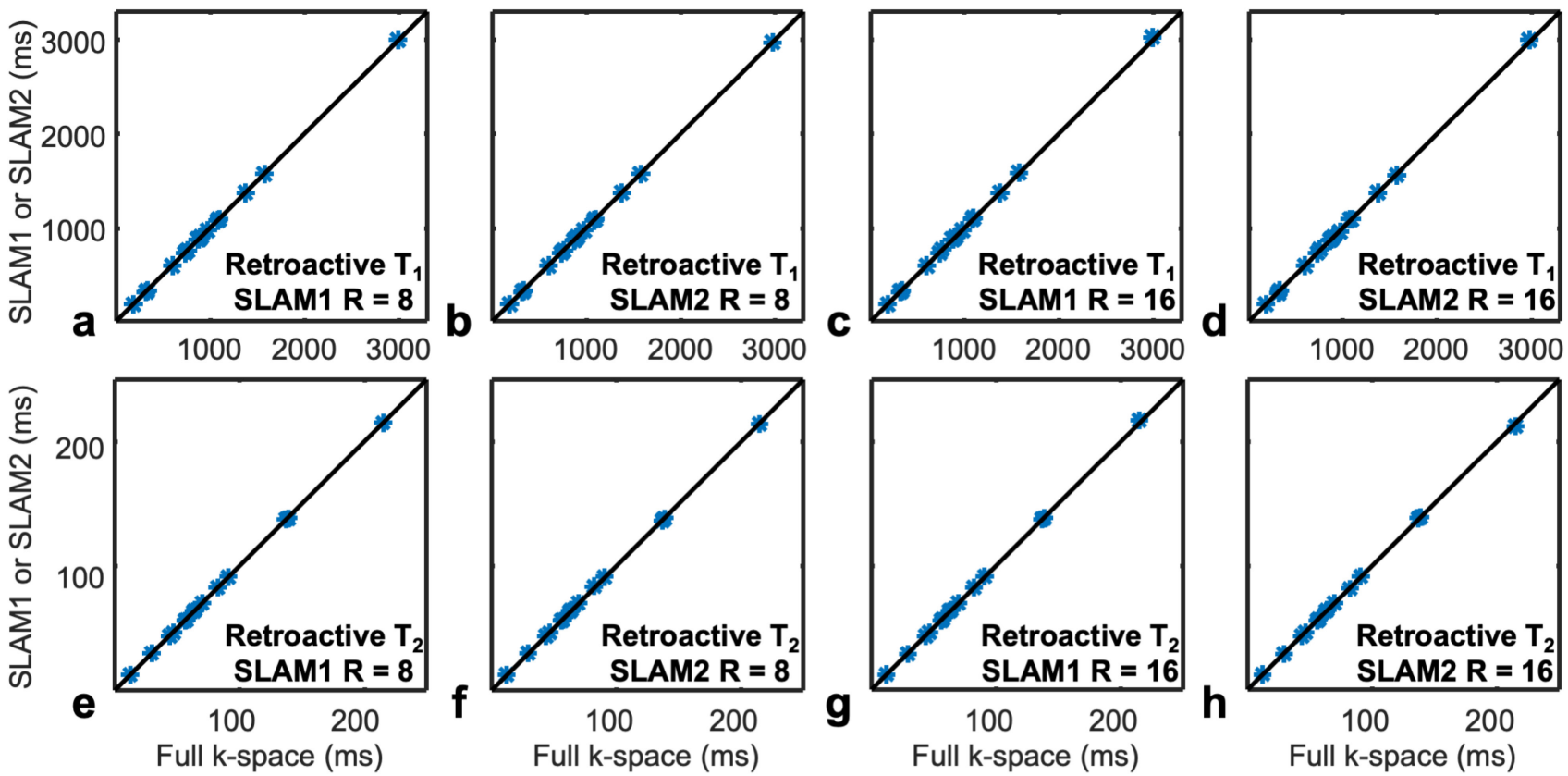

Figure 5.2 Retroactive SLAM1 and SLAM2 compartmental average T_1 (a-d) and T_2 (e-h) values as compared to the full *k*-space results for the 15 tube compartments in Figure 5.1. SLAM acceleration factors were R=8 (a, b; e, f) and R=16 (c, d; g, h). Points from the T_2=1930ms tube fell on the identity lines and were included in all quantitative analyses but omitted from the graphs to facilitate display.

Figure 5.3 and Figure 5.5 present additional data on the performance of the SLAM1 and SLAM2 algorithms for measuring T_1 in phantoms (Figure 5.3); T_2 in phantoms (Figure 5.4); and SLAM T_1 and T_2 measurements in fine gray matter structures in the human brain using SLAM2 applied retro-and pro-actively, with acceleration factors of 8- and 16-fold.

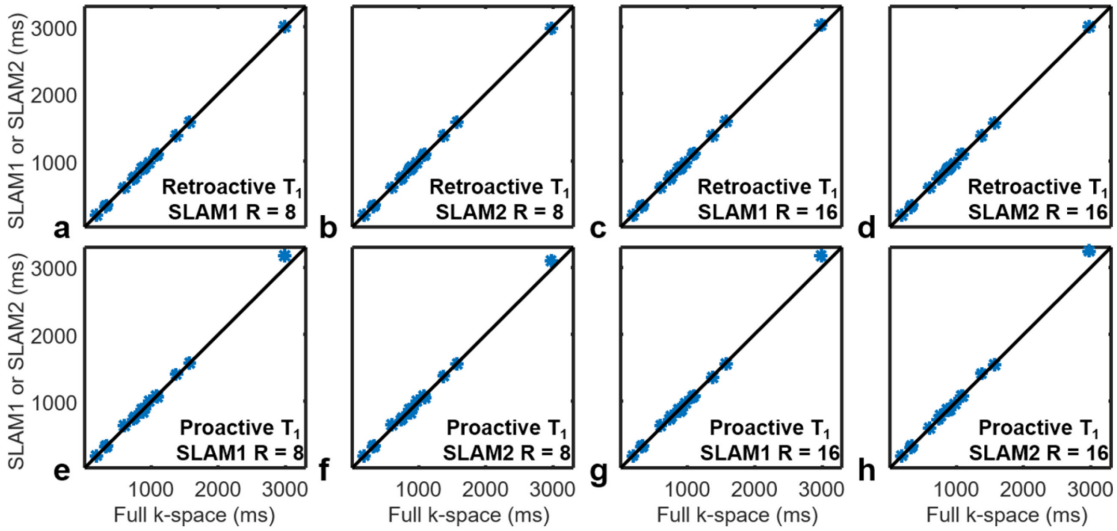

Figure 5.3 Retroactive (a-d) and proactive (e-h) SLAM1 and SLAM2 compartmental average T_1 values as compared to the full *k*-space results for the 15 tube compartments in Figure 5.1. SLAM acceleration factors were R=8 (a, b; e, f) and R=16 (c, d; g, h).

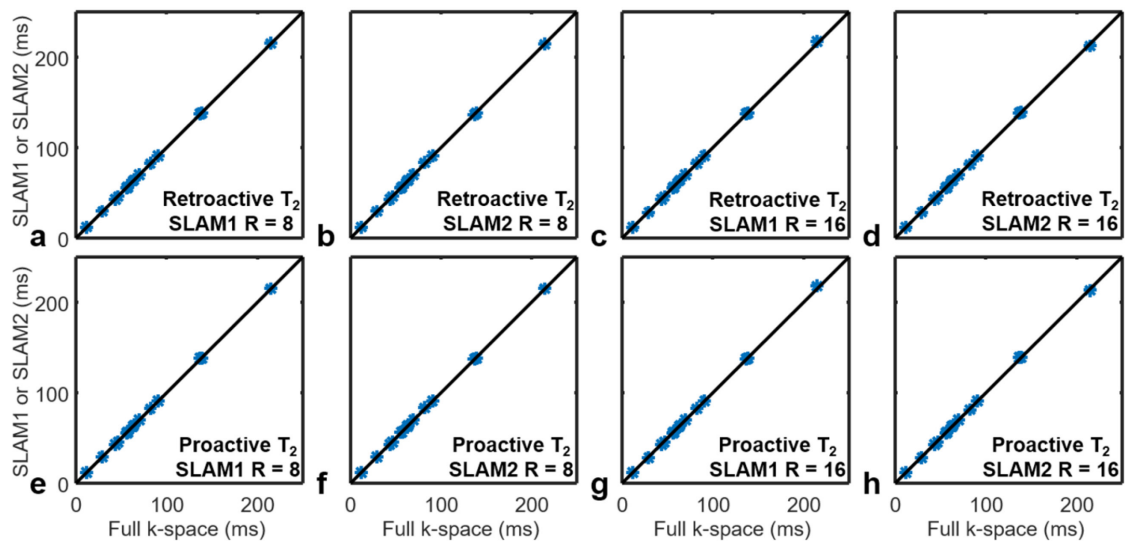

Figure 5.4 Retroactive (a-d) and proactive (e-h) SLAM1 and SLAM2 T_2 values as compared to the full *k*-space results. SLAM acceleration factors were R=8 (a, b; e, f) and R=16 (c, d; g, h). Points from the T_2=1930ms tube fell on the identity lines and were included in all quantitative analyses but omitted from the graphs to facilitate display.

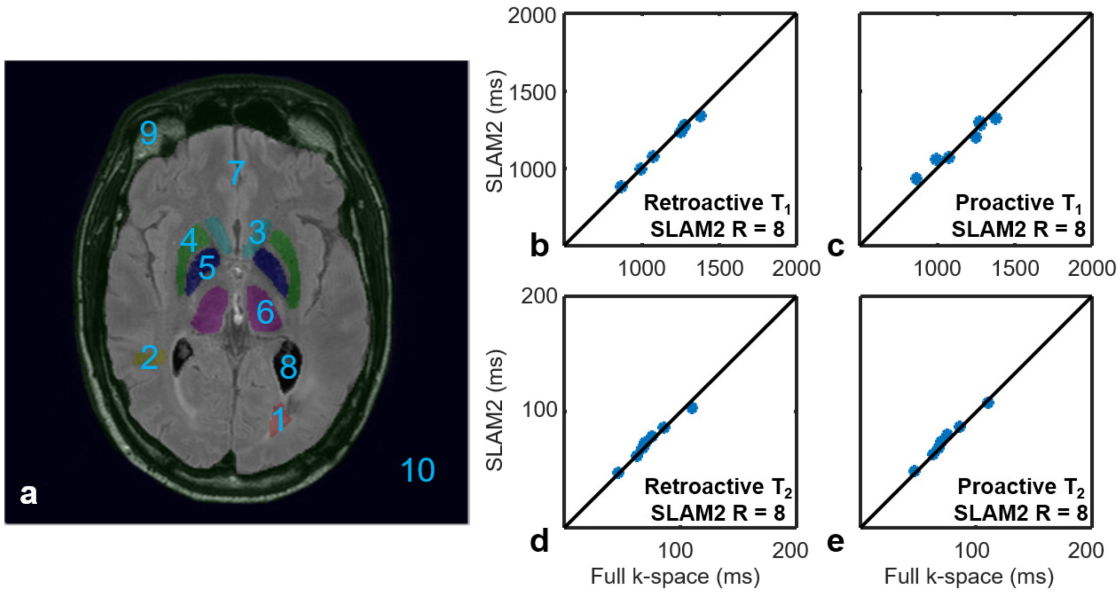

Figure 5.5 A brain tumor patient with deep gray matter regions segmented for compartmental T_1 and T_2 values. (a) Ten compartments (1: tumor or edema; 2: contralateral normal-appearing white matter; 3: caudate; 4: putamen; 5: globus pallidus; 6: thalamus; 7: rest of the brain; 8: ventricle; 9: scalp; and 10: background) segmented for SLAM reconstruction on a co-registered FLAIR image. Retroactive (b, d) and proactive (c, e) SLAM2 T_1 (b, c) and T_2 (d, e) values, as compared to full *k*-space measurements from the first seven compartments. SLAM acceleration factors were R=8 (b-e). Full *k*-space T_1 values were 1275, 1249, 993 and 1073 ms in caudate, putamen, globus pallidus, and thalamus, respectively. Accordingly, the T_2 values were 75, 63, 47 and 68 ms, respectively. These values were in good agreement with previous values reported in Lu et al. J Magn Reson Imaging 2005;22(1):13-22.

Figure 5.6 shows the reduction in motion artifact achieved by applying the readout gradient in the anterior/posterior direction, which is the primary direction of physiological motion (breathing, in this case).

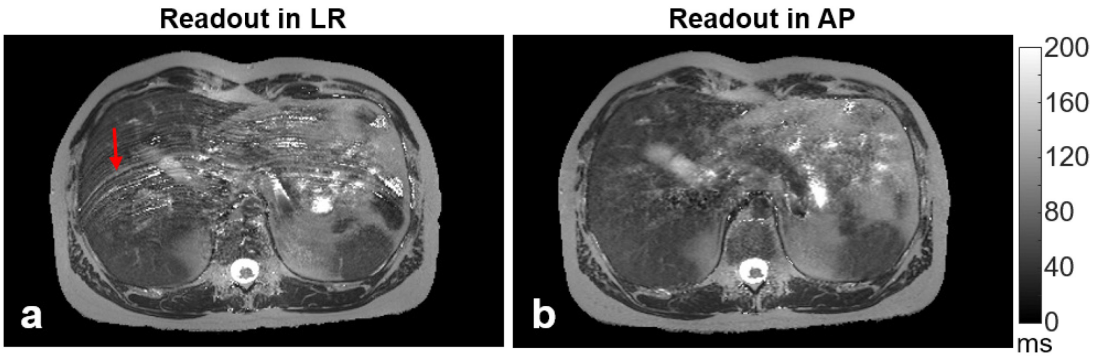

Figure 5.6 Full *k*-space T_2 maps acquired with the readout gradient in the left-right (a) and in the anterior-posterior (b) directions, respectively. Significant respiratory motion artifacts arose (red arrow) with the readout gradient in the left-right direction.

Figure 5.7 shows the application of SLAM to the measurement of relaxation times in the abdomen. The dSRF of the spleen compartment obtained from full *k*-space (Figure 5.7b), and 8-fold accelerated SLAM2 reconstruction (Figure 5.7d) are nearly identical, with the complex dSRF summing to 0.94. As in Figure 5.1, the SLAM1 result is less uniform (Figure 5.7c) even though the dSRF sums to 1. Moreover, there is little difference between the color-coded compartmental T_1 maps obtained with the full *k*-space data (Figure 5.7e), SLAM1 or SLAM2 (R=8, Figure 5.7f).

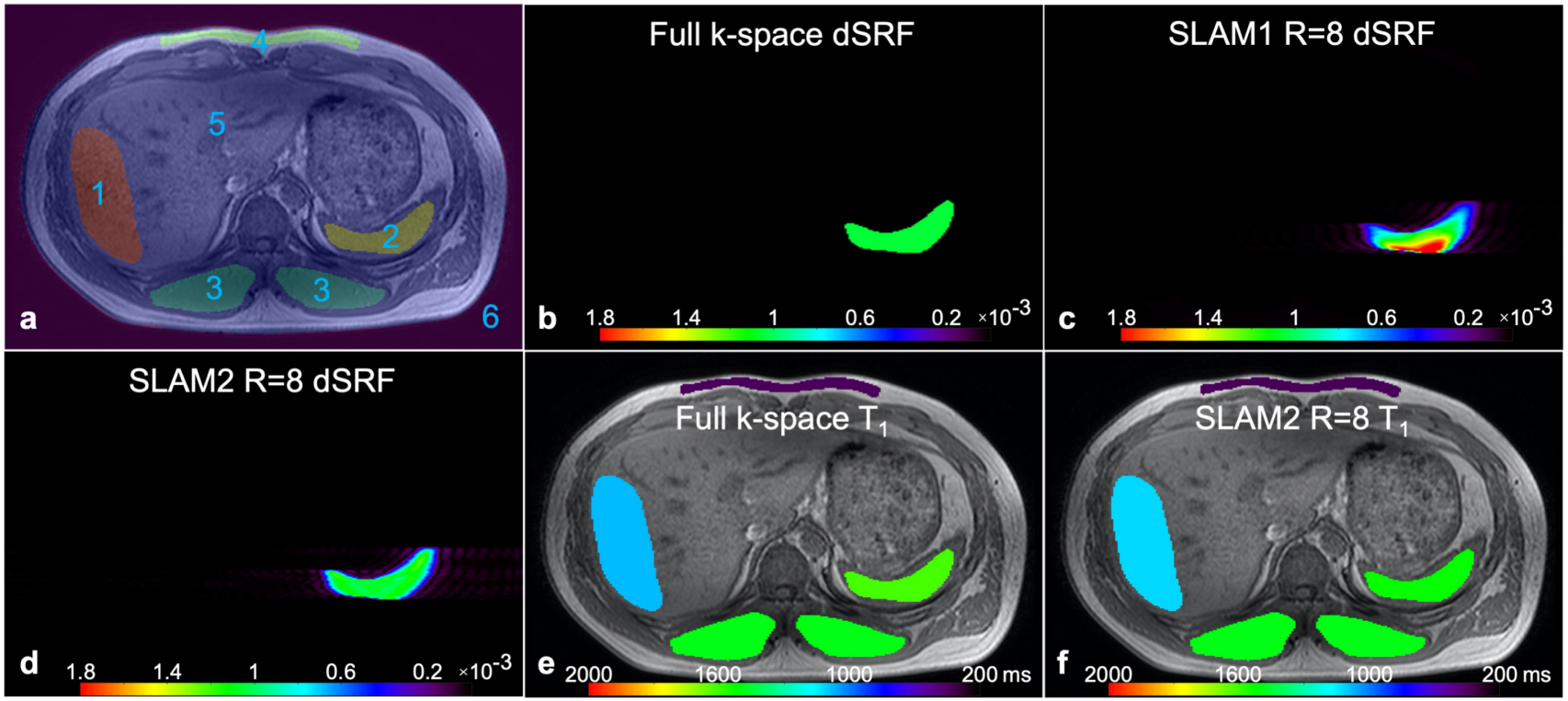

Figure 5.7 Compartmental segmentation, spatial localization properties, and compartmental T_1 maps for an abdominal study. (a) Six compartments (1: liver; 2: spleen; 3: muscle; 4: fat; 5: rest of the body; and 6: background) segmented for SLAM reconstruction on the co-registered T_1-weighted image. (b-d) Absolute dSRF for the spleen compartment reconstructed from the standard full *k*-space (b), SLAM1 with R=8 (c), and SLAM2 with R=8 (d). Color-scale was in arbitrary units. (e-f) Color-coded compartmental T_1 maps reconstructed from the standard full *k*-space data set (e), and from SLAM2 with R=8 (f).

Figure 5.8 compares the T_1 values from full *k*-space, SLAM1, and SLAM2 reconstructions pooled from abdominal compartments in all normal volunteers. The measured T_1 values (mean ± SD, ms) from the full *k*-space data sets were 836±59, 1372±91, 1547±217, 1321±33, and 377±23 for liver, spleen, kidney, muscle and fat, respectively. These agree with literature values at 3T of 809 [172] in liver; 1328 [172] in spleen; 1142-1545 [172] in kidney; 898 [172] and 1420 [173] in muscle; and 382 [172] and 371 ms [173] in fat, respectively. There were no significant differences between SLAM1, SLAM2 and the full *k*-space T_1 values ($p \geq 0.2$; $r \geq 0.90$). The percentage differences (mean ± SD) between SLAM1, SLAM2 and full *k*-space values were ≤1.4%±10.1% for retroactive (Figure 5.8a-d) and ≤1.7%±24.8% for proactive implementations (Figure 5.8e-h).

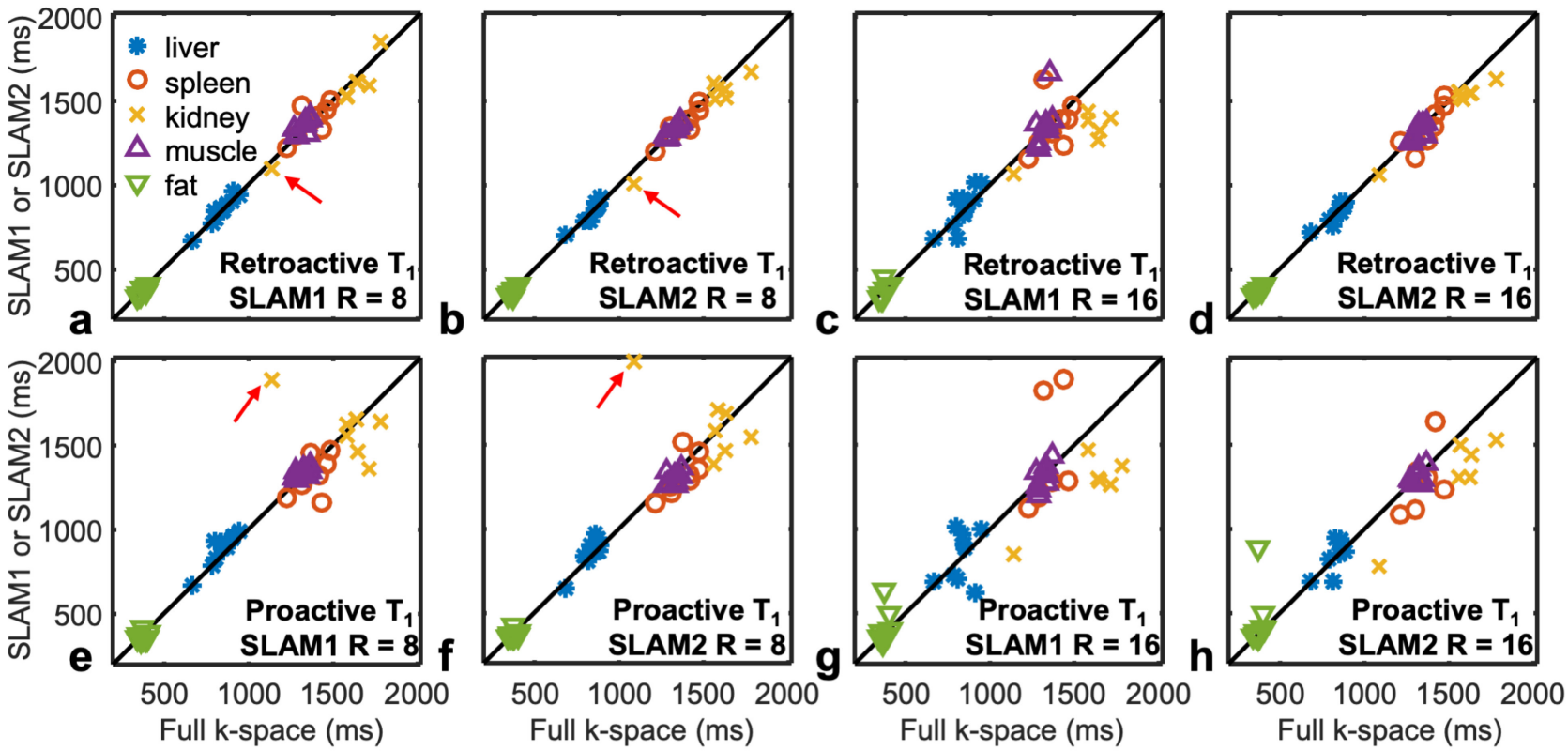

Figure 5.8 Retroactive (a-d) and proactive (e-h) SLAM1 and SLAM2 abdominal T_1 values as compared to the full *k*-space measurements. SLAM acceleration factors were R=8 (a, b; e, f) and R=16 (c, d; g, h). Red arrows indicate an outlier in the proactive SLAM1 and SLAM2 implementation (e, f) attributable to motion (see discussion) not present in the retroactive implementation (a, b).

Figure 5.9 compares abdominal T_2 values from SLAM1, SLAM2 and full *k*-space acquisitions in the same compartments and subjects. The measured T_2 values from the full k-space data sets were 43±6, 68±9, 97±4, 36±6, and 103±6 ms for liver, spleen, kidney, muscle and fat, respectively. Corresponding literature values are 34 [172] and 52 [174] for liver; 61 [172] and 91 [174] for spleen; 76-81 [172] and 127 [174] for kidney; 29 [172] and 32 [173] for muscle; and 68 [172], 133 [173], and 103-143 ms in fat [175]. There were no significant differences between SLAM and the full *k*-space results in Figure 5.9(a-d, f or h; $p \geq 0.07$), although differences were observed in Figure 5.9(e, g; $p=0.006$ and $p=0.004$, respectively). However, the percentage differences between SLAM1, SLAM2 and the full *k*-space measurements were ≤3.2%±13% and ≤4.4%±14% for retroactive (Figure 5.9a-d) and proactive (Figure 5.9e-h) implementations, respectively ($r>0.98$).

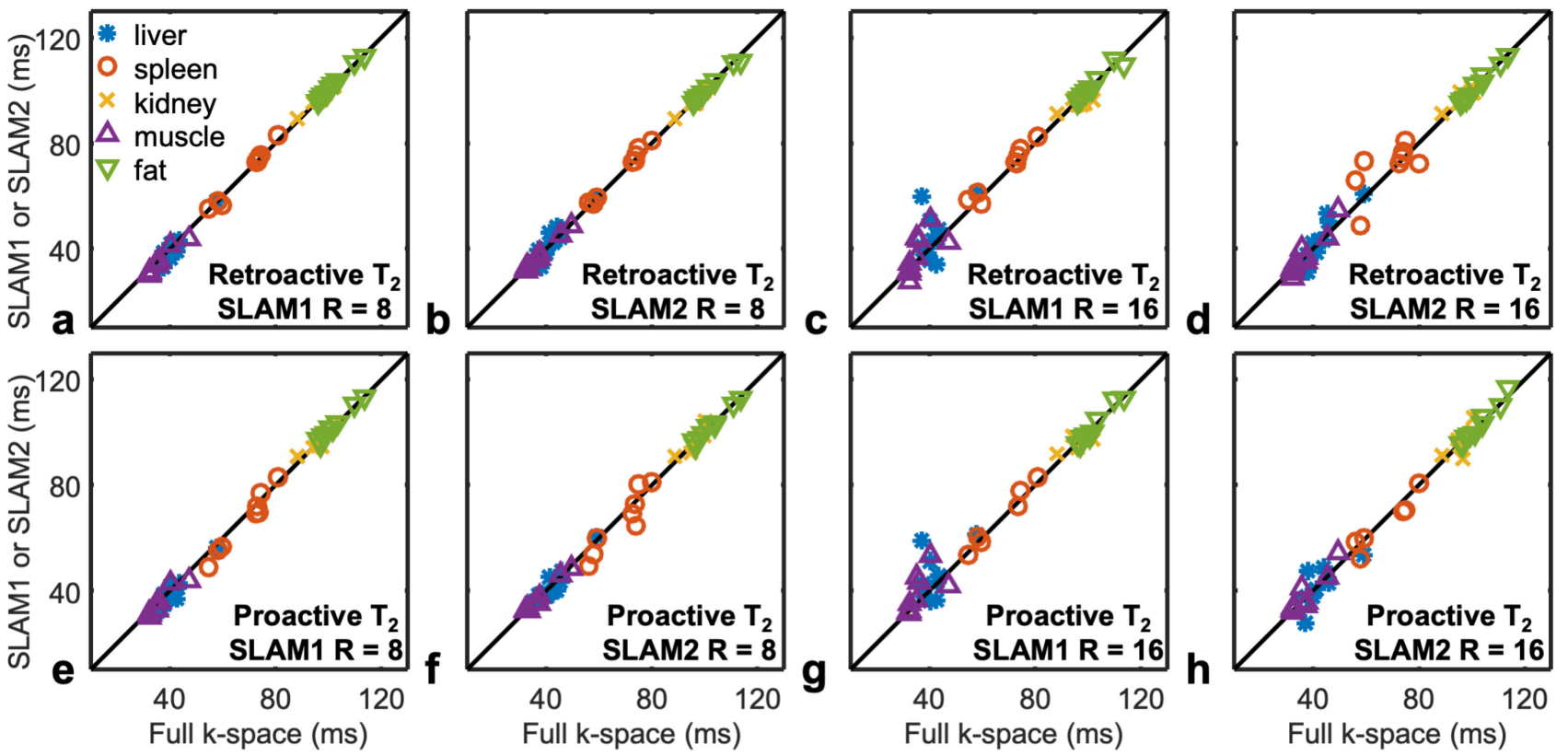

Figure 5.9 Retroactive (a-d) and proactive (e-h) SLAM1 and SLAM2 abdominal T_2 values as compared to the full *k*-space measurements. SLAM acceleration factors were R=8 (a, b; e, f) and R=16 (c, d; g, h).

Figure 5.10 plots the absolute dSRF of the tumor compartment from full *k*-space (Figure 5.10b), SLAM1 (R=8; Figure 5.10c) and SLAM2 (R=8; Figure 5.10d) reconstructions. As in Figure 5.1 and Figure 5.7, the SLAM2 algorithm generates a more uniform dSRF than the SLAM1 algorithm, but the sums of the complex dSRFs within the tumor compartment are 0.84 and 1, respectively. Importantly, there is no difference between the full *k*-space (Figure 5.10e) and SLAM2 (R=8, Figure 5.10f) or SLAM1 compartmental T_1 values.

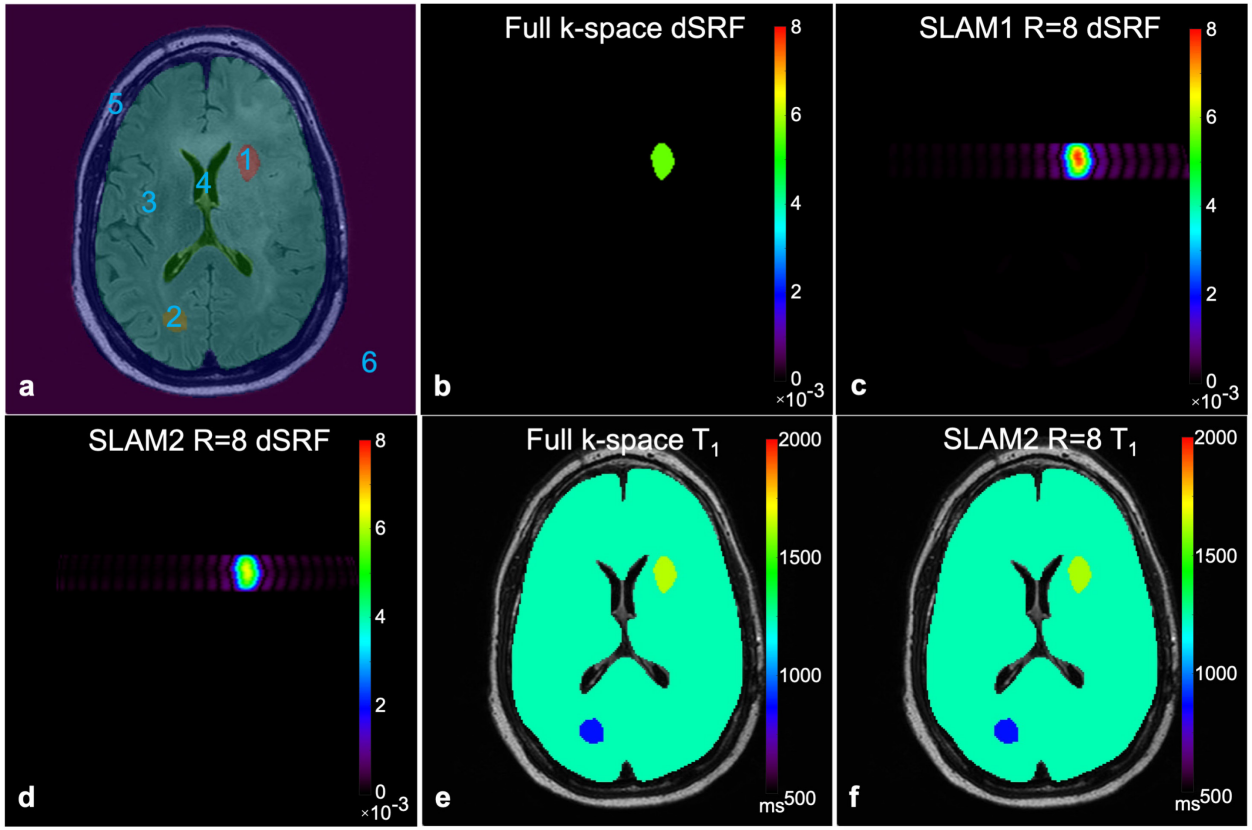

Figure 5.10 Compartmental segmentation, spatial localization properties, and compartmental T_1 maps for a brain tumor patient with glioblastoma. (a) Six compartments (1: tumor; 2: contralateral normal-appearing white matter; 3: rest of the brain; 4: ventricle; 5: scalp; and 6: background) segmented for SLAM reconstruction on a co-registered FLAIR image. (b-d) Absolute dSRF for the tumor compartment from the standard full *k*-space sampling (b), a SLAM1 reconstruction with R=8 (c), and a SLAM2 reconstruction with R=8 (d). Color-scale was in arbitrary units. (e-f) Color-coded compartmental T_1 maps (scale in ms) from the standard full *k*-space data set (e), and from SLAM2 with R=8 (f).

Figure 5.11 shows that the compartmental T_1 and T_2 relaxation data acquired in these SLAM studies are adequately fitted by mono-exponential relaxation curves.

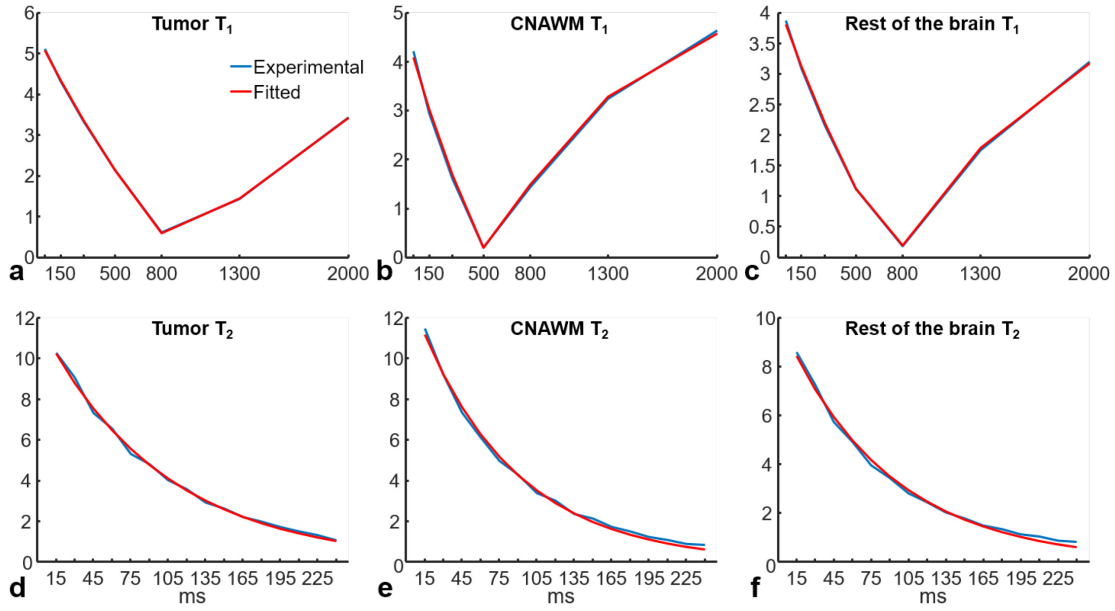

Figure 5.11 Experimental and mono-exponentially fitted T_1 (a-c) and T_2 (d-f) relaxation curves for the tumor (a, d), contralateral normal-appearing white matter (b, e), and rest of the brain (c, f) compartments from the brain tumor patient shown in Figure 5.10 (signal intensity in arbitrary units).

Figure 5.12 compares T_1 values from full *k*-space, SLAM1 and SLAM2 reconstructions in brain compartments from all tumor patients. Measured T_1 values from the full *k*-space data sets were 1518±223, 862±18, and 1201±86 ms in tumor, white matter, and 'rest of the brain' compartments, respectively. The white matter values agree with literature 3T values of 832 [176], 758 [177], and 859-865ms [147]. There were no significant differences between SLAM and full *k*-space measures in Figure 5.12a-d ($p>0.3$; $r\geq0.97$). The percentage differences between SLAM1, SLAM2 and the full *k*-space results were ≤2.7%±6.9% and ≤1.4%±6.0% for retroactive (Figure 5.12a-d) and proactive (Figure 5.12e-f) implementations, respectively.

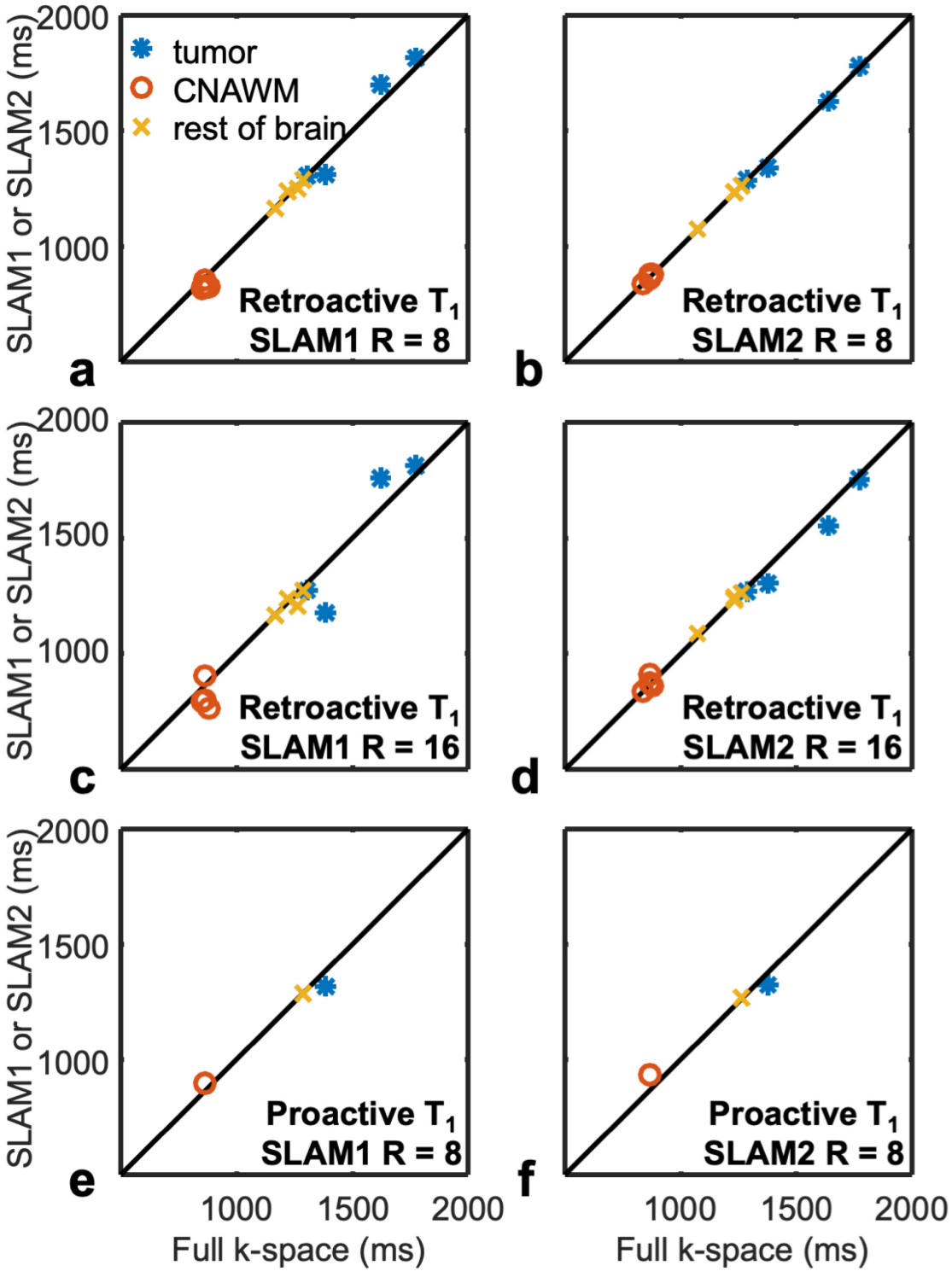

Figure 5.12 Retroactive (a-d) and proactive (e, f) SLAM1 and SLAM2 T_1 values, as compared to full *k*-space measurements from brain tumor patients. SLAM acceleration factors were R=8 (a, b; e, f) and R=16 (c, d).

Figure 5.13 compares T_2 values from full *k*-space with SLAM1 and SLAM2 in all tumor patients. The measured T_2 values from the full *k*-space data sets were 156±104, 77±9 and 85±4 for tumor, white matter, and 'rest of the brain', respectively. Values of T_2 for white matter were 80 [176], 81 [177] and 65 [147] ms in previous reports. There were no significant differences between SLAM and the full *k*-space results in Figure 5.13a-d ($p \geq 0.49$; $r \geq 0.996$). The percentage differences between SLAM1, SLAM2 and the full *k*-space results were ≤0.4%±6.2% and ≤1.6%±4.2% for retroactive (Figure 5.13a-d) and proactive (Figure 5.13e-f) implementations, respectively.

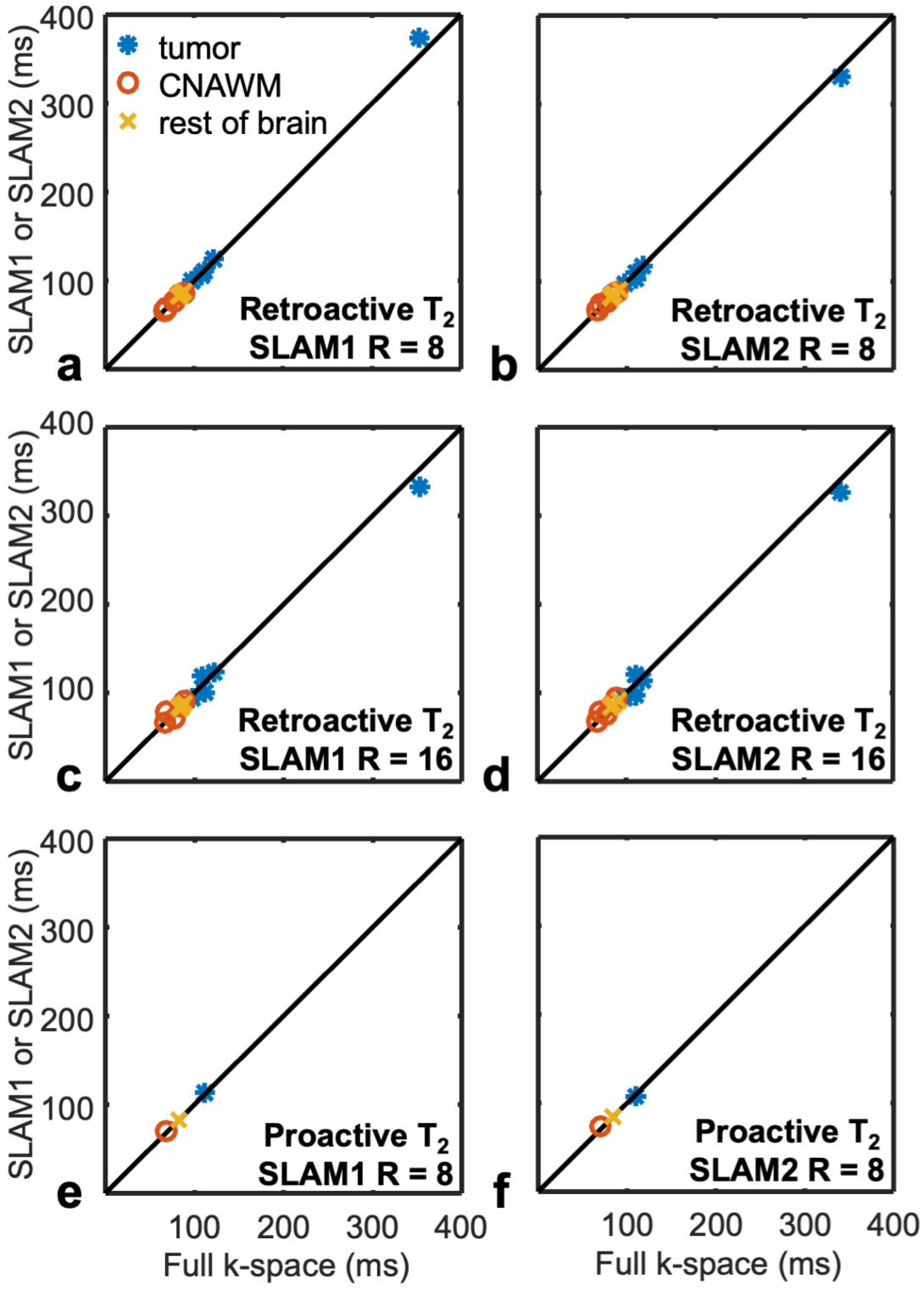

Figure 5.13 Retroactive (a-d) and proactive (e, f) SLAM1 and SLAM2 T_2 values as compared to the full *k*-space measurements from brain tumor patients. SLAM acceleration factors were R=8 (a, b; e, f) and R=16 (c, d).

Figure 5.14 summarizes the performance of retroactive SLAM1 and SLAM2 compared to full *k*-space reconstruction in the three sets of studies. SLAM2 (black dots and lines) generally outperformed SLAM1 (blue dots and lines). SLAM performed best in phantoms, and least well in the abdomen. SLAM2 with R=16 generated a percentage difference of 0.0%±0.7%, 1.4%±3.4%, and 0.5%±2.9%, for phantom, abdominal, and brain T_1 measurements, respectively. The corresponding differences for T_2 were 0.2%±1.9%, 0.9%±7.9%, and 0.4%±5.8%. T_1 differences for the SLAM1 algorithm in phantom, abdominal and brain studies were 0.1%±0.5%, 0.9%±10.1% and 2.7%±6.9%. The SLAM1 T_2 differences were 0.8%±4.5%, 3.2%±12.8% and 0.4%±6.2%, respectively.

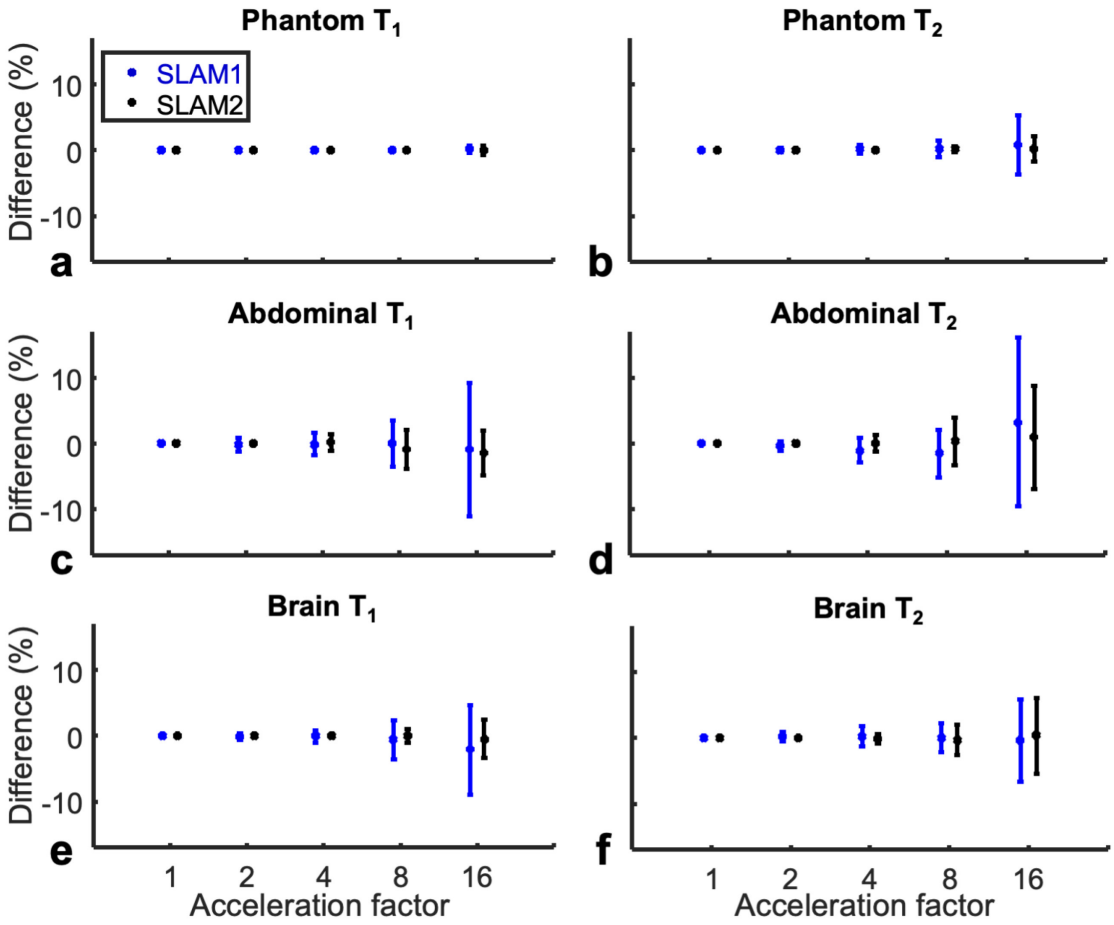

Figure 5.14 Percentage difference between SLAM1 (blue) and SLAM2 (black) relaxation times and the standard full *k*-space values in phantom (a, b), abdominal (c, d), and brain tumor (e, f) studies as a function of acceleration factors (R≤16). Values were means ± standard deviation.

5.5 Discussion

Although developed for MRS [53,157–159], SLAM is a general localization method that can be applied to derive any compartment-average MR parameter, as illustrated here for the first time with T_1 and T_2. By directly encoding whole compartments, the spatial encoding set can potentially be reduced to as few as the number of compartments [53,157–159]. Typically this is ≤10, as compared to the number of PE steps required for regular MRI, say ~256. The upshot is huge acceleration factors

that could enable acquisition of new study data that would otherwise be precluded by scan-time limitations in the clinic. Furthermore, by always choosing the phase-encodes from central *k*-space, the SNR of SLAM approximates the maximum SNR achievable from the compartment. This can provide an SNR gain by a factor of up to ($\sqrt{\text{compartment size/pixel size}}$)-fold[157] to offset the ($\sqrt{\text{scan-time}}$)-fold loss in SNR due to the reduced scan-time, as compared to the reference MRI. Because the phase-encoding steps and number of compartments are typically fixed for a given protocol, and because the segmentation and reconstruction are performed post-acquisition, the same truncated SLAM sequence can be applied as an add-on to regular protocols, and the results reconstructed from any desired set of segmented compartments post-exam.

Numerous methods have been proposed to measure *in vivo* T_1 and T_2 more efficiently than IR and MESE, but the latter remain reference standards for validation, as used here. Compared to the full *k*-space compartment-average results from phantoms (Figure 5.1 and Figure 5.2), the abdomen (Figure 5.7-Figure 5.9) and brain tumor patients (Figure 5.10-Figure 5.13), SLAM values deviated less than 13% from compartment-average values obtained from full *k*-space data sets, 8 or 16 times faster (Figure 5.14), in both proactive and retroactive implementations (Figure 5.2, Figure 5.8, Figure 5.9, Figure 5.12, Figure 5.13). SLAM relaxation times also agreed with previous published reports at 3T. Note that as a localization vehicle, SLAM is not bound to standard IR and SE sequences, and could just as well provide such acceleration on top of the efficiencies afforded by newer relaxometry approaches, when compartmental-average measures can suffice. The achievable acceleration generally depends on the size of the compartment and number of receive coil elements, but not the number of TE or TI time points.

Although the present study was limited to 2D relaxometry, SLAM is readily extended to 3D to provide even higher acceleration factors, as was demonstrated with 3D MRS [53].

That SLAM performed better in brain tumor studies than in abdominal studies (Figure 5.14) is likely due to the higher physiological motion in the torso. This, along with stochastic variations from the underlying SNR, also explains a slightly worse agreement for the proactive studies, which are affected by scan-to-scan variations as compared to retroactive implementations that use the same source data (Figure 5.8, arrows). The smaller errors for proactive abdominal T_2 mapping, may be due to the averaging effect of an echo-train compared to the single shot T_1 mapping sequence. In general, since the compartment typically comprises tens of voxels, SLAM reconstruction can mitigate motion artifacts between the scout image and relaxation time scans via the implicit signal averaging effect.

SLAM reconstruction follows a top-down approach, that starts with the standard reconstruction model (discrete FT with/without SENSE) upon which *a priori* compartmental information and the assumption of uniform compartments are imposed to reduce the dimension of the encoding matrices to create an accelerated PE set. The image compartment signals are then reconstructed by matrix inversion. Prior methods for compartmentalized MRS [178–181] not contemplated for MRI, have used a bottom-up continuous approach that while theoretically avoiding the truncation artifacts from discrete FT [180], cannot be practically validated from non-continuous *in vivo* data [53]. Here, the localization properties of each compartment in SLAM are completely determined by the multiplication of the dSRF with the image signal acquired from the standard discrete reconstruction model. Each compartment signal is the summation of this

product over the sample volume. Because Equation (5.1) is exact [53,157–159], the complex dSRF for the SLAM1 algorithm must sum to 1.0 within each compartment. Thus, the summed dSRF•signal product for SLAM1 will agree with that from full *k*-space to the extent that the underlying signals are uniform, or at least that their fluctuations cancel when summed. In practice, the SLAM2 algorithm tends to outperform the SLAM1 algorithm (Figure 5.14) due to its more uniform dSRF (Figure 5.1, Figure 5.7, Figure 5.10) and robustness to intra-compartmental signal inhomogeneity [53], even though its summed dSRF is <1.0. For a given study protocol, computation of the SLAM dSRFs from a few full *k*-space data sets can guide the choice of a suitable acceleration factor that can provide adequate localization of the range of compartments likely to be encountered in the larger study population.

The phase-encoding gradient set used in SLAM are determined by the standard reconstruction model, which in turn is determined by the prescribed FOV. The standard reconstruction model does not have to be a full *k*-space model, and can include SENSE-acceleration as noted above [53,159]. However, choosing a SENSE-accelerated model increases the PE gradient step-size for SLAM in proportion to the SENSE acceleration factor, which in turn can produce expansive side-lobes in the dSRF of the SLAM1 algorithm as exemplified in Fig. 13d of Ref [53]. This was not seen here with the full *k*-space reconstruction model (Figure 5.1, Figure 5.7, Figure 5.10). In any case, as a further refinement, the PE gradient set can be chosen to optimize the dSRF for a given compartment using the fractional SLAM (fSLAM) method [157].

Recently, multiple methods of accelerating relaxation time mapping with compressed sensing and/or model-based approaches have been proposed [182–188]. The

advantage of these methods compared to SLAM is that they can generate pixel-by-pixel relaxation time maps. Disadvantages include the complexity and uncertainty associated with nonlinear reconstruction, and/or the assumption of a relaxation model for reconstruction, which is usually mono-exponential [184]. SLAM can potentially be combined with model-based approaches [183,188], albeit at the expense of an explicit characterization of signal localization with the dSRF. View-sharing methods have also been used to accelerate relaxation time mapping [189–192], which can sacrifice high-frequency information and introduce errors at object edges [184,190]. In contrast, SLAM does not re-use *k*-space data from the scout image *per se*, only binary compartment masks that are created from a scout image. The scout image can be acquired from a completely different sequence than a T_1 or T_2 sequence, such as one acquired earlier as part of the clinical protocol. SLAM sacrifices intra-compartment resolution but preserves boundary information by incorporating compartmental definition into the reconstruction process.

In conclusion when compartment-average relaxation time parameters can suffice, SLAM can provide accurate, highly-accelerated and SNR-efficient measurements of relaxation times that quantitatively agree with standard values that may not otherwise be possible due to study-time constraints. The method might also be adopted to generate highly efficient compartment-average measures of diffusion, perfusion, and fMRI indices, etc.

Chapter 6: Towards automated image contrast optimization in MRI

A critical step in developing and applying MRI sequences in research and clinical practice is to tune the operating parameters to achieve a desirable contrast of the property-of-interest. Presently, scan parameters are chosen *a priori* to achieve contrast based on prior experience that may not be optimum for the scan being done. Here, dynamic contrast prediction systems are proposed that learn the signal pattern without the explicit physics modeling which requires tissue parameters that are often unknown or change rapidly as in dynamic MRI for screening, perfusion, intervention, or MRI endoscopy. The software architecture of the system provides interactive data collection and analyses with a calibration-prediction-acquisition workflow wherein the prediction sampling strategy is framed as a feature-selection problem. Three methods for automatic feature selection and contrast signal reconstruction are evaluated: (i) a baseline nearest-neighbor in parameter space method employing no *a priori* knowledge; (ii) a linear pattern synthesis method; and (iii) a light-weight feature-selective synthesizer neural network (FSSNet). The methods were implemented in phantom and human studies in which predicted contrast synthesis results are compared to real acquired images using image similarity metrics. Compared with the baseline method, both the FSSNet and the linear methods predicted image contrast behavior significantly better ($p<10^{-6}$), with the results of FSSNet proving most accurate (similarity ≥99%) overall. This work shows the feasibility of efficient parameterized contrast synthesis based on calibration data for on-the-fly MRI sequence development and optimization.

6.1 Introduction

The final stage of development of many a new system often involves tuning multiple parameters to achieve a desired performance. This also applies to developing new MRI pulse sequences or applying an established MRI sequence to new patient populations or diseases. In practice for a given application, the pulse sequence operating parameters are initially tuned by trial-and-error to achieve a desired contrast from a "weighted" combination of physical MRI properties or the physical property itself. This, subject to the imperative of maximizing the signal-to-noise ratio (SNR). The best combinations of operating parameters are then standardized in protocols to serve a specific application or diagnostic objective. Clinical MRI operations can ill-afford the time and effort required for iterative, case-by-case contrast optimization.

Speed is also a focus of recent developments in MRI. While sub-second "cine" MRI has existed for decades [193], continuous whole-body scanning wherein the body moves through the scan plane during acquisition [194,195] is available on many commercial MRI systems; and now there is multi-channel MRI at up to 100 frames(fr)/s [196] and MRI endoscopy at 10 fr/s [8]. The added value of high-speed MRI in each of these applications is the ability to rapidly monitor changes in scenery: whether it be moving organs in cardiac MRI [197]; therapy delivery in interventional MRI [198]; whole-body scanning; or MRI endoscopy [8] to identify pathology "on the fly". In such studies, a single "one-size-fits-all" acquisition parameter-set is invariably deployed. This acquisition set cannot be said to be optimum for all frames or all locations at all times: the legs, liver and brain in the whole body scan, or the vessel in transit during endoscopy, for example. High-speed MRI could enable MRI pulse sequence optimization

in real-time, but the technology for MRI contrast optimization has not kept up with the speed of MRI.

Indeed, it is desirable to have a method that can automatically tune the set of MRI sequence parameters–fast–to facilitate the introduction of a new MRI sequence or a new application and/or to optimize MRI "on the fly". Acquiring images using every combination of parameters and selecting one with the desired contrast, inefficient and impractical when the parameter space is large. A more efficient two-step process is to first predict image contrast under different parameter settings based on a small data sample. We call this process parameterized contrast synthesis (PCS). Second, the optimal parameter set is chosen from the PCS results in an image quality assessment (IQA) step. IQA can include reference-based, no-reference, subjective, objective, or mixed evaluation criteria [130,199–201]. The present paper focuses on PCS.

A classic model-driven method for PCS would use Bloch equation simulations of the MR signal evolution. While Bloch simulations can include all of the known physical dependencies [202–205], accurate scanner-side image contrast synthesis would require *a priori* physics modeling and the acquisition and mapping of both the sample properties by quantitative MRI (qMRI), as well as instrumental "spoiler" factors such as RF and main (B_0) field inhomogeneity. In simple cases, analytical equations like that prescribed by the Ernst angle can be used, but in general there is no simple analytical solution, and initiating time-consuming simulations for local tissue areas or pixels at the scanner to predict a contrast is all but impractical.

Alternative non-Bloch, data-driven methods could simply repeat the process of acquiring an image, recording the contrast, and changing the sequence parameter set,

until a desirable result is achieved. This process, too, is impractical without intelligent design to ensure rapid convergence, but machine learning approaches are well-suited to such tasks. As with its application to regular MRI [206,207], applying machine learning to PCS requires training on prior experimental contrast data to characterize the MRI protocol and/or its application. While the most commonly used unsupervised machine learning method–principal component analysis (PCA) [208–211]–is limited to finding linearly related components, advances in the use of nonlinear manifolds for analyzing high-dimensional MRI signals [212–214] could address the inherently nonlinear dependence of MRI contrast on the sequence parameter set.

Here we present a general (sequence-independent) PCS methodology for the purpose of automating MRI parameter selection for image contrast optimization. PCS is treated as a feature selection problem to most-efficiently sample the parameter space, and methods of learning the parametric dependence of steady-state image contrast are investigated using calibration data. We tested a PCS approach that creates a pattern library from training data by synthesizing coefficients using PCA and linear error regression in the parametric space, and a new method inspired by recent advances in feature selection using deep learning [215]. A naïve nearest-neighbor PCS approach that assumes no *a priori* knowledge of training data is also tested as a baseline for comparison. We designed and implemented software and a user-interface to communicate with a commercial 3T clinical MRI scanner in real-time, for fast-prototyping and testing of sequence contrast optimization algorithms, and implemented and tested the methods on phantoms and healthy human subjects.

6.2 Methods

6.2.1 Workflow

The overall workflow for automatically tuning the operating parameters of a general MRI sequence is divided into three stages: calibration, prediction, and acquisition. The calibration stage happens beforehand and offline, wherein parameters are varied in the target sequence and wherein image projection or whole image data are sampled over the potential range of parameter space. The data are used in the learning phase to characterize the contrast response to the sequence. They form a library which is used to develop a contrast model for the subsequent online stages of prediction and acquisition. At the prediction stage, with the study object of interest in the scanner, a small set of data is collected and fed into the model to predict the image contrast over the whole parameter space. At the acquisition stage, the predicted contrasts are used in combination with user-supplied evaluation criteria, to guide the optimal parameter choice, whereupon confirmational or working acquisitions are performed.

6.2.2 Software design

A block diagram of the software architecture called "*SchemeServer"* its interactivity with a clinical 3T whole-body MRI scanner (*Prisma*, Siemens Healthineers AG, Munich, Germany) is shown in Figure 6.1. *SchemeServer* is deployed from a personal computer connected to the scanner console via socket programming, wherein a "*SchemeOperator"* object is introduced as a sheer intermediate control layer. When a scan starts, instead of executing a precompiled parameter list with limited flexibility from the user interface at the scanner console, the *SchemeOperator* sends requests to the *SchemeServer* for executing commands that bear sequence parameter and looping

information assembled by the *SchemeServer*. The resulting data which are sent to the scanner's regular reconstruction pipeline, are intercepted to feed the data socket of the *SchemeServer* where they are processed in its data-handling thread. At the core of the *SchemeServer* is the "*SchemeNarrator"* module, which contains the most complex logic and is responsible for analyzing data received in real-time, and managing the parameter scheme including the prescription of new scanning commands. The *SchemeNarrator* has a uniform interface and is implemented as an embedded *Python* module inside an overall *C++* software infrastructure, which makes it possible for researchers to fast-prototype custom analysis algorithms and pulse sequences.

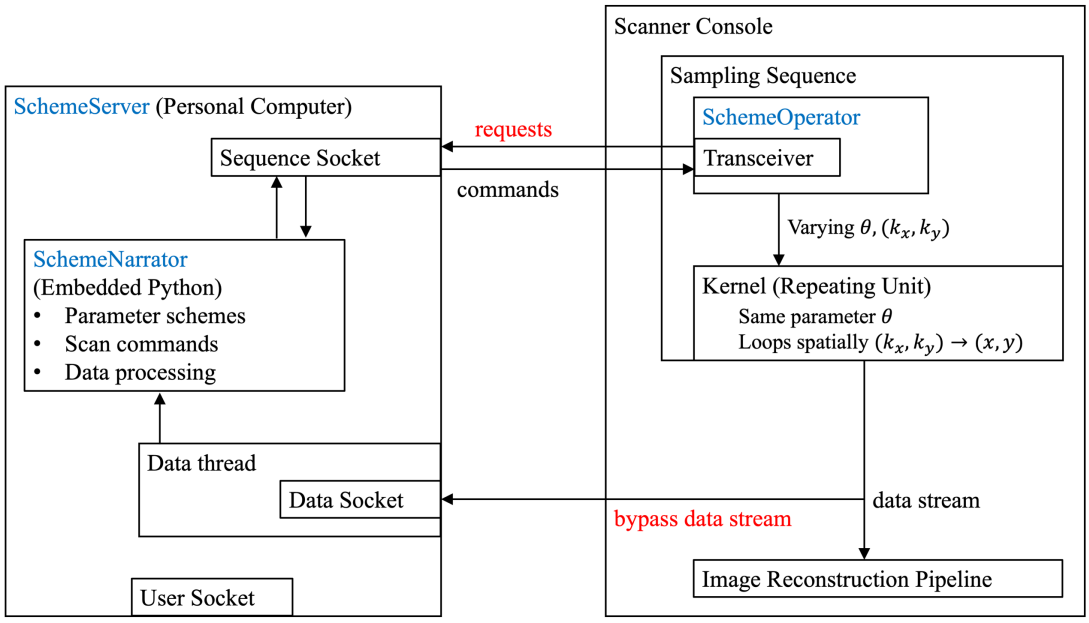

Figure 6.1 Software architecture of *SchemeServer* (left) deployed on an external computer communicating with an MRI scanner console (right). *SchemeOperator* is introduced into the original sequence program to execute parameter schemes prescribed by the core module *SchemeNarrator*. Acquired data are intercepted by *SchemeServer* for analysis. Communication between *SchemeServer* and the scanner is via system sockets. A user socket is used to accept imperative inputs from a human operator.

6.2.3 Sequence and Parameter Space Example

A conventional turbo spin-echo sequence is chosen to exemplify the methodology because it offers a broad parameter space to accommodate a large range of contrasts. We limit exploration to five dimensions: excitation flip angle, FA_{exc}; refocusing flip angle, FA_{refoc}; repetition time, TR; echo spacing ESP; and the effective echo-time TE. Two sets of parameter combinations are used in this study, *ParamSpace1* and *ParamSpace2*, as listed in Table 6.1.

Table 6.1 Example parameter setting spaces used in studies

Name	FA_{exc}(°)	FA_{refoc}(°)	TR(ms)	ESP(ms)	TE(ms)	Number of total settings
ParamSpace1	90, 45	180, 120	3000, 500	10, 20	ESP, 4×ESP	$2^5 = 32$
ParamSpace2	90	180, 120	3000, 2000, 1000, 500	10, 20	ESP, 4×ESP	2×4×2×2 = 32

6.2.4 Feature Selection and Contrast Synthesis

In the calibration stage we acquire an image of the calibration sample at each grid-point of the parameter space to form a signal library to learn the contrast pattern. At the prediction stage, images of a subset of the grid-points are acquired, from which contrasts are predicted for the whole parameter space. The selection of the prediction subset can be random or viewed as a feature-selection problem wherein the most effective features are sampled to obtain the maximum information.

More formally, we denote the whole data matrix of all images over the parameter setting grid by $\boldsymbol{X} \in R^{n\times m}$, where n is the number of pixels per image and m is the number of parameter settings. If $\boldsymbol{x}_p \in R^{n\times 1}$ is the p^{th} column of $\boldsymbol{X}$, the selected set of

parameter settings for the subset of prediction images can be represented as $S = \{p \mid \boldsymbol{x}_p \text{ is acquired}\}$, and the acquired image set is:

$$\boldsymbol{X}_S = \mathcal{F}(\boldsymbol{X}; S) \in R^{n \times m_s} \tag{6.1}$$

where $\mathcal{F}$ is the selection function and $m_s = |S|$ is the cardinality of the selected set. The prediction or contrast synthesizing process is represented as $\widehat{\boldsymbol{X}} = \mathcal{G}(\boldsymbol{X}_S; \theta)$, where $\mathcal{G}$ is the synthesizer function and θ are trainable parameters of the model. Prediction results are evaluated with a similarity metric $\mathcal{R}(\widehat{\boldsymbol{X}}, \boldsymbol{X})$ which compares the synthesized dataset $\widehat{\boldsymbol{X}}$ with the whole ground truth dataset, $\boldsymbol{X}$. Based on this description, the process of optimizing contrast prediction involves searching for the most effective set of selected acquisition parameters S^*, and the most effective synthesizing model as represented by parameters θ^*. That is:

$$S^*, \theta^* = \underset{S,\theta}{\operatorname{argmax}}\, \mathcal{R}(\widehat{\boldsymbol{X}}, \boldsymbol{X}) = \underset{S,\theta}{\operatorname{argmax}}\, \mathcal{R}(\mathcal{G}(\boldsymbol{X}_S; \theta), \boldsymbol{X}) \tag{6.2}$$

We start with a nearest-neighbor method that provides a baseline for predicting performance in the absence of a priori knowledge. As a first advance on this method, we use a linear pattern synthesis approach employing PCA and minimum mean square error (MMSE) linear regression. As a further advance, we introduce a feature-selective synthesizer employing a neural network for the dual purpose of parameter selection and contrast synthesis.

Baseline Nearest-neighbor Method

When no prior information is utilized, the most basic PCS method is to assign data to non-acquired parameter grid-points, using image content acquired from their nearest neighbors in the parameter space. Because there is no information regarding the

relationship among parameter grid-points, the acquired grids are selected randomly. More formally, if S is a randomly selected set from parameter grid-points,

$$\hat{\boldsymbol{x}}_i = \boldsymbol{x}_p \quad \text{subject to} \quad p = \underset{j \in S}{argmin} \, |\phi_i - \phi_j| \tag{6.3}$$

where ϕ_i is the pulse sequence parameter corresponding to image $\boldsymbol{x}_p$. In practice, the parameter space is normalized so that values in each dimension vary between $[0,1]$.

Linear (PCA) Pattern Synthesis

The idea of the linear pattern synthesis method is to create a pattern library from training data, and infer the synthesizing coefficients from least-squares solutions in the selected dimensions, S, of the patterns. Then the synthesizing coefficients are applied to patterns for all dimensions to predict all contrasts. More specifically, singular value decomposition (SVD) is performed on a dataset $\boldsymbol{X} \in R^{n \times m}$,

$$\mathbf{X} = \mathbf{U}\mathbf{D}\mathbf{V}^{\mathrm{H}} \tag{6.4}$$

where $\mathbf{D} \in \mathrm{R}^{\mathrm{n} \times \mathrm{m}}$ is the diagonal matrix of singular values in descending order, and $\mathbf{U} \in \mathrm{R}^{\mathrm{n} \times \mathrm{n}}$ and $\mathbf{V} \in \mathrm{R}^{\mathrm{m} \times \mathrm{m}}$ are unitary matrices whose columns are orthonormal bases. The pattern library is formed by selecting the most significant $K \leq m$ principal components weighted by corresponding singular values to accommodate the variability they represent in the whole dataset, that is:

$$\mathbf{Y} = \mathbf{D}_{\mathrm{r}}\mathbf{V}_{\mathrm{r}}^{\mathrm{H}} \tag{6.5}$$

where $\mathbf{D}_{\mathrm{r}} \in R^{K \times K}$ is the diagonal matrix of the largest K singular values, and $\mathbf{V}_{\mathrm{r}} \in R^{K \times m}$ is formed by selecting the first K columns of $\boldsymbol{V}$. $\mathbf{Y} \in \mathrm{R}^{\mathrm{K} \times \mathrm{m}}$ is called the generative matrix. Like Equation (6.1), $\mathbf{Y}_{\mathrm{s}}$ is the pattern library in the selected dimensions,

$$\mathbf{Y}_s = \mathcal{F}(\mathbf{Y}; S) \in R^{K \times m_s} \tag{6.6}$$

To achieve $\widehat{\boldsymbol{X}}$ for a set of measured images $\boldsymbol{X}_s$, the generative coefficients $\boldsymbol{\alpha} \in R^{n\times K}$ are acquired as the least-squares solution to

$$\boldsymbol{X}_s = \alpha \boldsymbol{Y}_s \tag{6.7}$$

and multiplied by the generative matrix $\mathbf{Y}$, that is,

$$\widehat{\boldsymbol{X}} = \boldsymbol{\alpha}\mathbf{Y} \tag{6.8}$$

At the feature selection stage, the above process is performed on the training dataset with S being all combinations of the m_s features from the m parameter settings (or a subset thereof, depending on feasibility). S^* is selected as the one resulting in optimal reconstruction similarity or minimal residual from $\mathcal{R}(\widehat{\boldsymbol{X}}, \boldsymbol{X})$. $\mathbf{Y}$ and S^* are then saved and can be used to acquire sampling data and predict contrast for incoming unknown samples.

Neural Network based Feature-selective Synthesis

The architecture of the feature-selective synthesizer neural network (FSSNet) shown in Figure 6.2, performs as an atypical autoencoder whose input and output are signal patterns from each pixel over the whole parameter space. The encoding feature-selection layer is based on a method that assigns the largest weights to selected features after training with proper constraints [215]. The decoding synthesizer part is inspired by Ref. [216], with the difference that we do not explicitly encode for the relaxometry parameters but rather, synthesize the contrasts directly from the input signals. After training with known calibration data, the feature selection part is discarded and the synthesizer is used to infer response based on the sub-set of data acquired during the prediction stage.

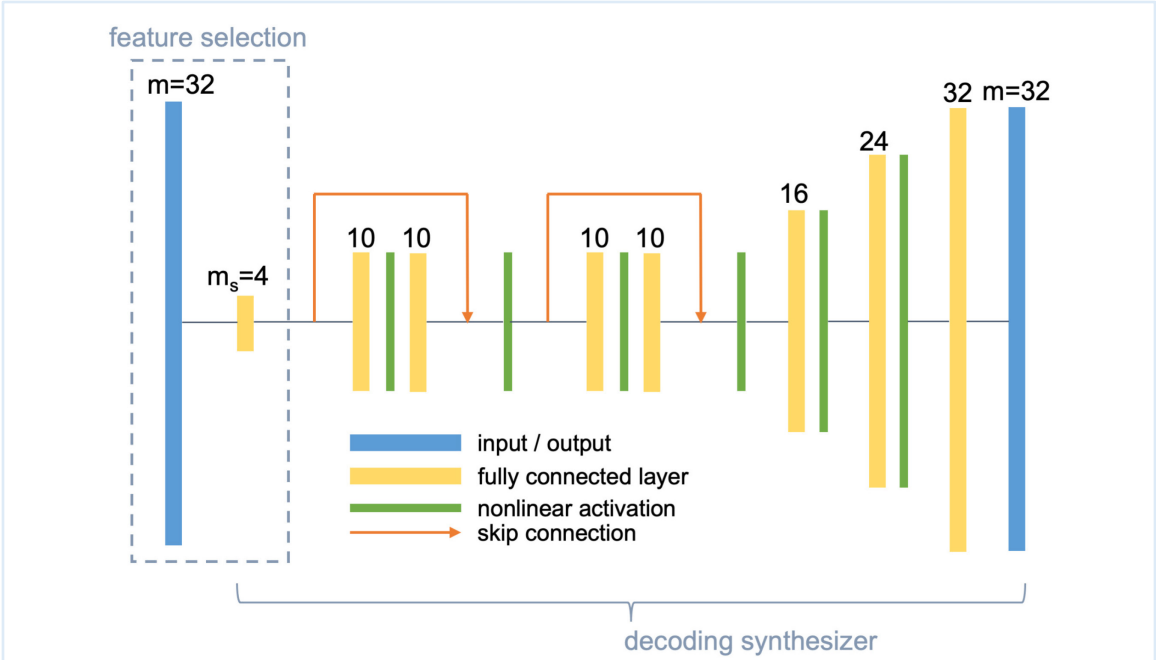

Figure 6.2 The architecture of the feature-selective synthesizer neural network, FSSNet, comprises a feature selection layer which assigns the largest weights to auto-selected features and a synthesizer to synthesize contrast over the whole range of parameter settings. It is trained as an autoencoder using contrast signals from each pixel as input or output. Only the synthesizer part is used at the prediction stage.

To train the feature selection layer in accordance with Ref. [215], each column of the training dataset $\boldsymbol{X}$ is standardized with zero mean and a variance equal to one. The loss function used for training the neural network is

$$L(\theta) = l(\theta) + \lambda_1 \Omega_1(\boldsymbol{W}) + \lambda_2 \Omega_2(\boldsymbol{W}) \tag{6.9}$$

where θ represents parameters of the model; $\boldsymbol{W} \in R^{m \times m_s}$ are the weights of the feature selection layer; $l(\cdot)$ is the reconstruction loss of the autoencoder; and the $\lambda_{1,2}$ are regulation coefficients. The two regulation functions $\Omega_{1,2}(\cdot)$ have the form

$$\Omega_1(\boldsymbol{W}) = \sum_{k=1}^{m_s} max\left(0, \sum_{j=1}^{m} |w_{jk}| - 1\right) \tag{6.10}$$

and

$$\Omega_2(\boldsymbol{W}) = \sum_{k=1}^{m_s} max\big(0,1 - \mathrm{Var}(\mathbf{A}_\mathrm{k})\big) \tag{6.11}$$

where the w_{jk} are the elements of $\boldsymbol{W}$, and $\boldsymbol{A}_k$ is the k^{th} activation of the selection layer, i.e.,

$$\boldsymbol{A}_k = \sum_{j=1}^{m} w_{jk}\, \boldsymbol{X}_j, \text{ for } k = 1, \dots, m_s \tag{6.12}$$

$\mathrm{Var}(\mathbf{A}_\mathrm{k})$ is the variance of each activation value over the input dataset, which tends to decrease below one when the selection layer selects more than one low-correlated feature. It was demonstrated in Ref. [215] that Ω_1 and Ω_2 work antagonistically to achieve sparse weights of selection layers that correspond to relevant features.

Here, the input datasets are MR images acquired with different parameters that can be highly correlated with each other. At each of the m_s activations of the selection layer, one or more highly correlated feature(s) may be selected instead of a single relevant feature, because their effect on the training constraints (Equations (6.10) and (6.11)) are nearly equivalent. We introduce a margin value of $\Delta \approx 0.05$ for training constraints to enhance sparsity and to compensate for marginal errors introduced during separation of the dataset for training and validation/testing purposes. Equations (6.10) and (6.11) then become:

$$\Omega_1(\boldsymbol{W}) = \sum_{k=1}^{m_s} max\left(0, \sum_{j=1}^{m} \left|w_{jk}\right| - (1 - \Delta)\right) \tag{6.13}$$

$$\Omega_2(\boldsymbol{W}) = \sum_{k=1}^{m_s} max\big(0, (1+\Delta) - \mathrm{Var}(\mathbf{A}_\mathrm{k})\big) \tag{6.14}$$

During training, the weights of the selection layer are updated at every epoch, via

$$w_{jk} \leftarrow \frac{|w_{jk}|w_{jk}}{\sum_{j=1}^{m}|w_{jk}|^2} \tag{6.15}$$

to select the most salient features while keeping the reconstruction error low. After the feature selection training stage, the relevant parameters are selected as:

$$\widehat{S^*} = \{\underset{j}{\mathrm{argmax}}|w_{jk}| \text{ for } k = 1, \dots, m_s\} \tag{6.16}$$

whereupon the selection layer is discarded. The rest of the neural network is fine-tuned by further training with the selected contrasts as input to reconstruct whole contrast datasets as output.

6.2.5 MRI Experiments

MRI experiments are performed according to the workflow described above on the clinical 3T MRI scanner (Figure 6.1). *SchemeServer* is installed on a personal laptop (*MacBook Pro 2019*, macOS Catalina, 2.3 GHz 8-core Intel Core i9, 16 GB memory, Apple Inc., CA, USA). During scanning, images and central k-space line projections at each grid of *ParamSpace1* or *ParamSpace2* are collected under the control of *SchemeServer*, and are standardized (with mean=0, variance=1). Datasets serve two purposes: (i) as reference training data to create the signal pattern library; and (ii) as testing data to predict a target contrast response. To evaluate the capability of contrast synthesis for an unknown study object learned from an arbitrary reference dataset, we employ an approach of cross prediction. This selects a subset of parameter settings S^* and a synthesis model θ^* trained with one object (phantom or human), to apply to other

objects whose datasets are acquired within the same whole set of parameter settings (*ParamSpace1 or 2*) as ground truth. For a new object being studied, a subset $\boldsymbol{X}_{S^*}$ of its whole dataset $\boldsymbol{X}$ is selected as prediction sampling data according to selection choice S^*, as determined from the reference dataset. Then, based on the prediction sampling data $\boldsymbol{X}_{S^*}$ and the synthesis model trained with reference dataset θ^*, the whole dataset of the new test object is predicted as $\widehat{\boldsymbol{X}} = \mathcal{G}(\boldsymbol{X}_{S^*}; \theta^*)$. We use the Pearson correlation coefficient as the similarity metric $\mathcal{R}(\widehat{\boldsymbol{X}}, \boldsymbol{X})$ between the predicted contrast $\widehat{\boldsymbol{X}}$ and the actual acquired contrast $\boldsymbol{X}$, to evaluate the accuracy of synthesis. The prediction sampling data, $\boldsymbol{X}_{S^*}$, are omitted from the evaluation because they are considered known information. All the computations for training and prediction were performed on the *MacBook* laptop.

Phantom Studies

Phantom studies are performed on 3cm-diameter by 11cm-long sample tubes of agarose gel doped with $CuSO_4$ to exhibit different spin-lattice (T_1) and spin-spin (T_2) relaxation parameters. Although not an intended nor needed output of the present work, the T_1 and T_2 values which are the source of image contrast, ranged from 195 to 2980 ms and 12 to 1930 ms, respectively [9]. The tubes are rotated and shuffled to form different structures to simulate different samples as shown in (Figure 6.3). Images of upright and oblique structures (Figure 6.3) are acquired at each five-parameter dimensional coordinate of *ParamSpace1* and *ParamSpace2*, as listed in Table 6.1. To implement the cross-prediction approach described above for each of the parameter settings (*ParamSpace1 or 2*), a dataset of one phantom structure (upright or oblique) is used for training each of the nearest-neighbor PCS, the linear PCA and the FSSNet PCS methods.

These methods are then applied to the other phantom structures. The performance for each training-prediction pair is evaluated using the similarity metric $\mathcal{R}(\widehat{\boldsymbol{X}}, \boldsymbol{X})$.

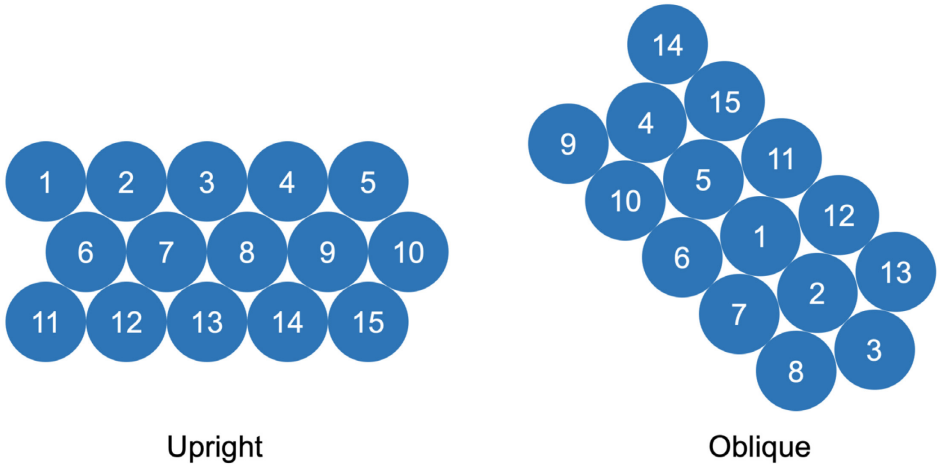

Figure 6.3 Tubes with different relaxometry parameters are switched and rotated to simulate different samples to test for cross reference prediction.

Human Subject Studies

We recruited 7 healthy subjects who gave informed consent for this study approved by our Institutional Review Board. Brain scans were acquired from 3 of the subjects using the *ParamSpace1* parameter settings, and from the other 4 subjects using the *ParamSpace2* settings from Table 6.1. For the cross-prediction approach, the dataset for each subject is used to train the nearest-neighbor, the linear PCA and the FSSNet PCS methods. The training provides a subset of predicted parameter sets to sample in accordance with the synthesis model. These are applied to images from other subjects within the group to create predicted images (excluding those in the prediction subset) that are evaluated against the true acquired images. The cross-prediction approach generates a total of $3 \times 2 + 4 \times 3 = 18$ training-prediction pairs. Prediction performance is compared among the three PCS methods using ANOVA and pairwise t-tests.

Neural Network Training

The FSSNet is implemented with PyTorch [217]. For each training dataset from a phantom or human, the network is trained for 2880 epochs during the feature selection stage. λ_1 and λ_2 are varied between $[10^{-4}, 0.002]$ and $[0.001,\ 0.02]$, respectively. L_1 and L_2 regularizations are applied on weights of the decoder with coefficients 10^{-4}. The "*Adam*" optimization algorithm is used with a learning rate of 0.01 [218]. The selection merging in Equation (6.15) is applied for every 100 epochs after epoch 2160. After the feature selection stage, the most dominant features are selected and the decoder is trained for 2000 more epochs without L_1 and L_2 regularization.

6.3 Results

6.3.1 Feature Selection

An example of the training process of the FSSNet feature selection layer is shown in Figure 6.4 . In Figure 6.4(a1-a3), the weights of the feature layer become more and more sparse to select the most relevant parameters for each feature. As noted above, because images acquired with different parameters are highly correlated, each feature selects a highly-correlated cluster rather than a single parameter. Figure 6.4(b1-b3) shows the corresponding correlation matrix with clusters annotated with red dashed boxes. Figure 6.4(a4) shows the effect of interval-feature merging (Equation (6.15)) at the last stage of training to select a single most relevant parameter for each contrast feature while maintaining reconstruction accuracy.

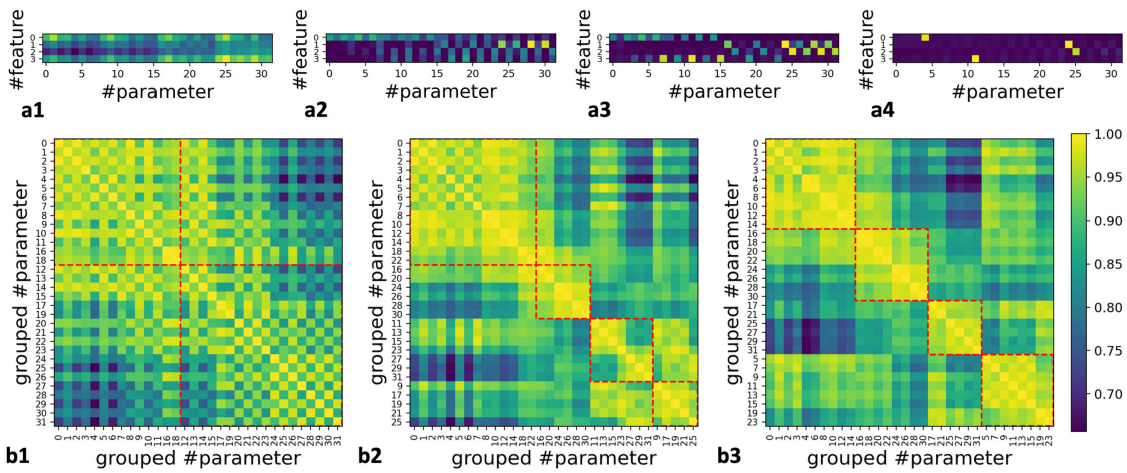

Figure 6.4 An example training process for feature selection. a1-a4: weights of feature selection layer at training epoch 50, 300, 2150, 2880. b1-b3: correlation among training images at different parameters, with parameters grouped according to clustering from the feature selection layer at training epoch 50, 300, 2150. Clusters are marked as the red dashed boxes.

6.3.2 Phantom Studies

Acquisition of the training dataset from the phantoms took 22.4 min and 20.8 min for *ParamSpace1* and *ParamSpace2*, respectively. Offline training took 2.8 min for the linear method and 7 min for the FSSNet on the laptop computer. The nearest-neighbor method did not need training. Synthesis for all the predicted contrasts took 2 ms, 19 ms, and 12 ms for the nearest-neighbor, the linear and the FSSNet methods, respectively.

The average similarity measure $\mathcal{R}$ from each setting is shown in Table 6.2. Some cross-prediction synthesis results are exemplified in Figure 6.5. The nearest neighbor method did not predict contrasts successfully in general, and its average similarity metrics were much lower than those from the linear pattern method and the FSSNet method (Table 6.2). For each 5-dimensional datapoint in parameter space, FSSNet synthesis outperformed the linear pattern synthesis.

Table 6.2 Average Similarity Measure $\mathcal{R}$ of Contrast Synthesis

Study	Parameter Settings	Average Synthesis $\mathcal{R}$ (%)		
		Nearest neighbor	Linear	FSSNet
Phantom	ParamSpace1	95.10	99.73	99.83
	ParamSpace2	94.49	99.80	99.87
Subject	ParamSpace1	92.80±1.81*	98.76±0.57*	98.81±0.63*
	ParamSpace2	93.21±0.92†	98.90±0.38†	99.10±0.33†

* $\mathcal{R}_{NN} < \mathcal{R}_{Linear}$ (p<0.001), $\mathcal{R}_{NN} < \mathcal{R}_{FSSNet}$ (p<0.001).
† $\mathcal{R}_{NN} < \mathcal{R}_{Linear}$ (p<0.001), $\mathcal{R}_{NN} < \mathcal{R}_{FSSNet}$ (p<0.001), $\mathcal{R}_{Linear} < \mathcal{R}_{FSSNet}$ (p<0.001).

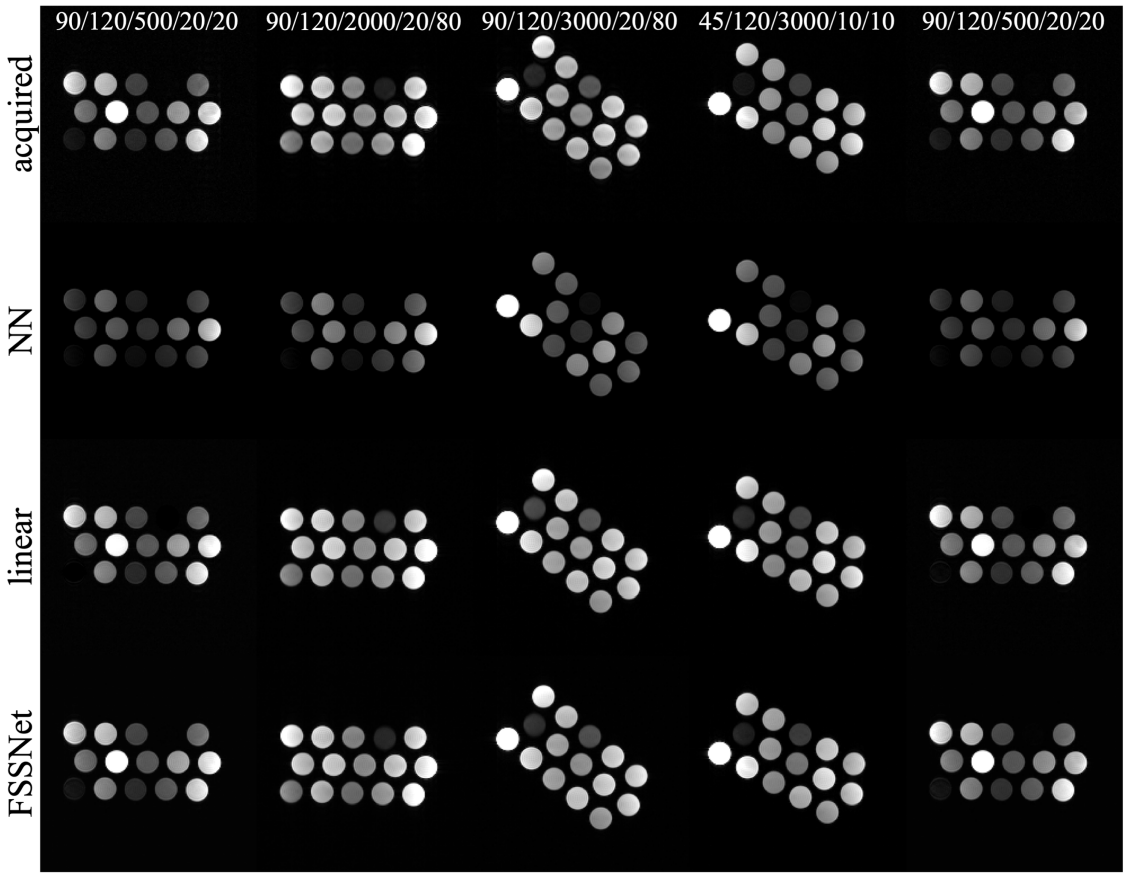

Figure 6.5 Contrast synthesis results of the phantom. Column 1-5: images at different sampling parameters, indicated at the top in format (FA_{exc}/FA_{refoc}/TR/ESP/TE). Units are the same as in Table 6.1. Row 1: acquired reference images; Row 2: corresponding synthesized images using nearest-neighbor method; Row 2: synthesized images using linear method; Row 4: synthesized images using FSSNet.

6.3.3 Human Subject Studies

Acquisition of the training dataset for the human studies took 29.9 min and 27.7 min for *ParamSpace1* and *ParamSpace2*, respectively. Offline training took 8min for linear method and 13min for FSSNet on the laptop. The nearest-neighbor method did not need training. Synthesis for all the predicted contrasts took 4 ms, 40 ms, and 22 ms for the nearest-neighbor, the linear and the FSSNet methods respectively.

The average correlation coefficients from each settings and methods are also listed in Table 6.2. Some of the cross prediction synthesis results are exemplified in Figure 6.6. As in the phantom study, the nearest neighbor method was not a good predictor of contrasts in general. ANOVA confirmed significant differences between the image similarity metrics associated with the three methods ($p<10^{-6}$ for both *ParamSpace1* and *ParamSpace2*). Pairwise t-testing showed that the similarities of the nearest neighbor method were significantly lower than the those of the other two methods ($p<0.001$ for both *ParamSpace1* and *ParamSpace2*). The average similarities of FSSNet method were higher than those of the linear pattern method, although the difference was only significant for *ParamSpace2* ($p<0.001$).

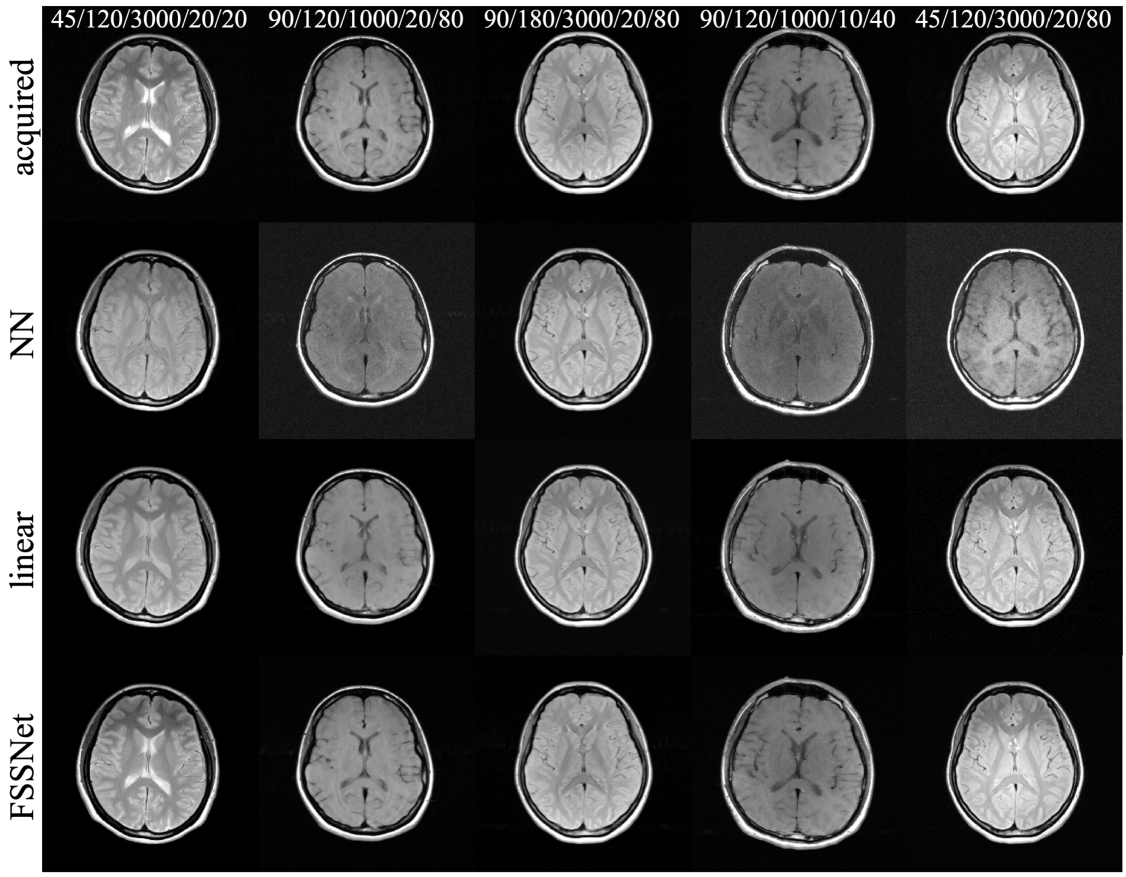

Figure 6.6 Contrast synthesis results of the subjects. Column 1-5: images at different sampling parameters, indicated at the top in format (FA_{exc}/FA_{refoc}/TR/ESP/TE). Units are the same as in Table 6.1. Row 1: acquired reference images; Row 2: synthesized images using nearest-neighbor method; Row 3: synthesized images using linear method; Row 4: synthesized images using FSSNet.

6.4 Discussion

In this work we proposed for the first time a methodology that learns an MR image contrast pattern solely from calibration data spanning an acquisition parameter space, without explicit physics modeling. We introduced a practical software structure employing new algorithms for contrast prediction based on a small subset of image samples and a paradigm for evaluating prediction performance. Compared to the baseline nearest-neighbor method which is arguably the best guess without knowledge of the sequence *a priori*, the linear PCA-based pattern characterization and the neural network

FSSNet methods selected effective image contrast features and more accurately predicted image contrast. The FSSNet method performed best overall. The methodology offers not only the potential for contrast-based optimization of MRI pulse sequences in real-time with high-speed MRI, but also provides an efficient approach to parametric optimization of new MRI pulse sequences in general.

The functionality of the *SchemeServer* module (Figure 6.1) can potentially prescribe arbitrary sampling patterns for sequence optimization. In the current highly-regulated scanner software environment, this tool leverages much of the existing program logic, injecting only a *wrapper*-layer that controls execution of the sequence. Data acquired in real-time are sent to the external computer to be processed by the *SchemeServer* module which sends parameter adjustment commands back to the scanner according to pre-defined sampling plans or based on real-time analysis of the image stream. Core processing tasks are handled by the *Python*-based *SchemeNarrator* module for quick prototyping of custom processing algorithms and access to the latest signal processing and machine learning software packages. The real-time feedback on image sampling and parameter adjustment, is well-suited to applications in interventional MRI [5,8], as well as those high-speed imaging settings in which contrast characteristics changes from one view to the next.

It is worth noting that although the time spent on acquisition of the training data and the training process takes longer than a few minutes, this is only a one-time offline task. The synthesis times of linear method and FSSNet are all of the order of tens of milliseconds on a standard personal computer, which is already close to the frame rate of

real-time MRI (10ms per frame). This computation time can be further decreased up to 2-4 times on a GPU-based system [126].

The regulation functions in Equations (6.10) and (6.11) used for training the feature selection layer are based on the assumption that mixtures of different features reduce the total variance [215]. Here, the separation of datasets into training and evaluation sets, introduces a small error that causes the variance of each variable in the training set to differ (slightly) from one. We addressed this by adding an error term (Δ) to keep the two regulation functions working antagonistically for selecting features that most effectively predict contrast. The selection layer only optimizes the selection of separate sets of correlated features or clusters (Figure 6.4) that contain arguably-similar information. Enforcing updated weights in the selection layer (Equation (6.15)) at a relatively large interval of epochs allows a singular variable for each feature selection to emerge without significantly degrading the prediction accuracy.

For all of the phantom and subject studies, the observation that the prediction accuracy of the linear pattern and the FFSNet methods were higher than the nearest neighbor method is, perhaps, unsurprising given the added value of the prior knowledge derived from the reference training data. In theory, MRI contrast is not linearly related to the parametric field and the neural network can accommodate such nonlinearities. Although the FSSNet method was significantly better than the linear method only in *ParamSpace2*, it did not underperform in *ParamSpace1* either (Table 6.2). Moreover, it may prove advantageous in higher-dimensional parameter spaces, where an exhaustive search of predicted contrast space presents a greater computational burden using linear approaches. Note also that we did explore other synthesis parameters and methods,

including the use of different K values in Equation (6.6), dictionary searching, and standardized vs. raw datasets. However, these approaches did not come close to the two methods presented in terms of prediction accuracy. In addition, the calibration datasets used for training were sampled from whole image slices, which might be overkill vs. sampling smaller "regions-of-interest" for some applications. The undersampling of acquisition and reconstruction methods such as is afforded by compressed sensing methods commonly used in real-time MRI, does enable the acceleration of calibration studies and facilitates the exploration of larger parameter ranges and/or dimensions including, for example, bandwidth and spatial resolution.

In summary, we demonstrated the feasibility of predicting parameterized contrast behavior for MRI with patterns learned from calibration datasets and minimal data sampling. To this end, we presented a practical design, data sampling and processing algorithms. The methodology could support deployment of novel research MRI sequences, patient-specific *in situ* tuning of high-speed as well as conventional MRI sequences, and facilitate the development of new, interactive and interventional MRI applications.

Chapter 7: Conclusions

7.1 Summary

The goal of bringing interventional intravascular MRI into clinical practice, is interaction, which requires that decisions and operations can be performed based on real-time feedback. These will naturally emerge when a diagnosis/treatment session proceeds, given the known unknowns and variables of interventional procedures. Around this general concept, this dissertation explores multiple aspects that could advance IVMRI further towards realistic, including diagnostic imaging, therapeutic monitoring, adaptively optimized sequence deployment, and accelerated parametric measurements. This effort has resulted in multiple conference presentations and journal papers.

First, devices and software for IVMRI guided IVHIFU have been developed for perivascular tissue ablation. The suitability, feasibility and MRI-compatibility are demonstrated with prototype catheters. Catheter design and workflow optimization, especially the introduction of circulation cooling system and the revelation of the key effects of combined ablation time and coolant temperature, results in successful vessel-preservation during perivascular ablation. The systematic in-scanner experiments further verify the performance of the proposed procedure, and demonstrate the coordination of systems and team operations in a close-to-clinical environment with *in vivo* studies. These works have generated multiple conference presentations and a journal publication [1–5].

Second, real-time interventional diagnostic imaging with MRI has been brought to reality for the first time, by accelerating the speed of MRI endoscopy by 5-fold up to 10 frames per second and integrating with a real-time communication and display system,

comparable to that employed in clinical X-ray fluoroscopy. Dedicated MRI endoscope catheters and internal software components are designed to ease the optimization of the system. Image analysis has been performed on such internal MRI streams where no precedence exists, and trade-off between image quality and speed are discussed with practical application needs in mind. This work fills the missing role of MRI in the field of intravascular imaging, and has also generated several conference presentations and a journal publication [6–8].

An early work of using minimal-acquisition linear algebraic modeling for ultrafast compartmentalized relaxation times mapping is included. The SLAM method originally proposed for MR spectroscopy has been extended for relaxation mapping. As only an extremely reduced dataset is required for sampling, it enables acquisition of information that would otherwise be inapplicable for clinical imaging in terms of time. This work also in concept connects loosely with the acceleration method of real-time MRI endoscopy, and the data sampling strategy parameter-based contrast synthesis.

The above works have specifically explored the therapeutic and diagnostic potential of IVMRI, and opened the topic of speed and contrast for not only IVMRI, but regular MRI. During these developments, the need for more powerful software and analysis tools to support interactive MRI intervention became evident. To address this need, a framework is proposed to allow parameter-based interactive MRI image contrast synthesis that can be used with many MRI sequences that requires minimal training data and modeling knowledge. The interaction-enabling software is based on real-time communication to facilitate arbitrary data sampling patterns and flexibility in online analysis component. The contrast synthesis process is framed as a feature selection

problem that can be efficiently solved by machine learning methods such as the PCA method and the DNN based method. This work opens the potentiality to automatically tune and enhance contrast for existing clinical and new research sequences, and has resulted in a conference presentation and a journal publication in preparation [11].

Interventional MRI is a comprehensive research topic that transcends many disciplines, including MR physics, the medical physics of intervention and dosage, catheter materials science and engineering, signal processing and software, RF hardware, etc. In my opinion, the critical point for successful studies often involves the rapid acquisition of precision, actionable visual feedback from the working end of the interventional probe. At present, dedicated software components developed and presented herein, handle this feedback for each application. For future work, a flexible, unified, and interaction-driven software framework will be at the crux of new interventional MRI applications.

7.2 Future Directions

The current design of IVMRI HIFU catheter (Table 2.1, catheter #3) has 4 channels of ablation transducers targeting at different directions. It still relies on mechanical rotation for beam control of finer granularity. For future work, it is desirable to integrate more channels to enable beam targeting completely through electrical interface. To make the workflow more seamlessly, it would be critical to integrate the ablation control unit with thermal monitoring interface. Studies with animal disease models and patients are needed to further understand the efficacy of thermal therapy. Though the size and flexibility of the current integrated catheter is suitable for major

vessels which we were targeting at the proposal of this project, further miniaturization is desirable to broaden its applications at various body regions.

MRI endoscopy shares some of the remaining exploration directions as IVMRI HIFU such as catheter miniaturization and disease model studies. Besides these, computer-aided steady retraction might help improve its usability and imaging quality to the next level, which also requires integration of the MRI feedback interface with a mechanical control unit. Temperature mapping using real-time MRI endoscopy has never been explored, and is an interesting topic as it could incorporate the IVMRI HIFU system to bring a fully endoscopic multifunctional device that can perform diagnosis and therapy in a single, unified workflow. Preliminary studies have shown that the artifacts of real-time MRI endoscopy image frames have a common pattern resulted from the extreme undersampling. Plenty of training data is available for this kind of problem as real-time MRI endoscopy studies generate a large number of image frames. This indicate that the image quality could potentially be further improved through denoising deep neural networks.

The linear and nonlinear PCS methods are able to predict sequence contrast behavior at different operation parameters, laying the basis towards automatic operation parameter optimization. It is, yet an open question as which objective function to choose for such optimization. Formally, the objective function is represented by $Q(\widehat{x_p})$, where p is the selection of operation parameter and $Q(\cdot)$ is a quality function of the input image (or ROI patch) under evaluation. The implementation of function $Q(\cdot)$ has many possibilities, including quantitative approaches such as histogram assessment and feature-based quality evaluation methods, as well as subjective approaches, where a user

interface displays the parameterized synthesis results for human users to select the optimal operation parameter. These approaches can be combined or used interchangeably, as they can be inserted into the *SchemeNarrator* framework as customizable modules. The optimization framework proposed in this work should be further studied with diseased models and multiple pulse sequences. Preliminary work has shown its applicability in IVMRI, and it is interesting to study its added value in real-time MRI endoscopy. Furthermore, IVMRI HIFU, MRI endoscopy and PCS all relies on real-time communication loop with MRI console, the *SchemeNarrator* framework can be potentially generalized to unify the underlying infrastructure that is utilized by intravascular or interventional MRI applications. This will to the largest extent save duplicate work, expedite development process and facilitate studies of IVMRI.

Appendix A: MRI Endoscopy Videos

The corresponding videos of the MRI endoscopy images shown in Figure 4.7, Figure 4.8 and Figure 4.9 are provided online (download *Supplementary Materials* at https://doi.org/10.34133/2021/6185616). Real-time endoscopy at 6fps, 10fps and conventional MRI endoscopy at 0.3fps are displayed at the true display speed as visualized on the scanner console.

Video S1 6 fps real-time endoscopy of porcine vessel *ex vivo* in Figure 4.7 (row a).

Video S2 10 fps real-time endoscopy of porcine vessel *ex vivo* in Figure 4.7 (row b).

Video S3 0.3 fps fully-sampled "conventional" endoscopy of porcine vessel *ex vivo* in Figure 4.7 (row c).

Video S4 6 fps real-time endoscopy of diseased human vessel *ex vivo* in Figure 4.8 (row a).

Video S5 10 fps real-time endoscopy of diseased human vessel *ex vivo* in Figure 4.8 (row b).

Video S6 0.3 fps fully-sampled "conventional" endoscopy of diseased human vessel *ex vivo* in Figure 4.8 (row c).

Video S7 6 fps real-time endoscopy of porcine vessel *in vivo* in Figure 4.9 (row 1).

Video S8 10 fps real-time endoscopy of porcine vessel *in vivo* in Figure 4.9 (row 2).

Video S9 0.3 fps fully-sampled "conventional" endoscopy of porcine vessel *in vivo* in Figure 4.9 (row 3).

Video S10 Comparison of 6 fps real-time endoscopy of diseased human vessel *ex vivo* in Figure 4.8 (row a) before and after preprocessing filter correction.

Video S11 Comparison of 10 fps real-time endoscopy of porcine vessel *in vivo* in Figure 4.9 (row 2) before and after preprocessing filter correction.

Bibliography

[1] Xiaoyang Liu, Nicholas Ellens, Parag Karmarkar, Paul Bottomley. Multifunctional Intravascular MRI-Ultrasound Ablation/Imaging/Thermometry System, Baltimore, MD: 2016.

[2] Liu X, Ellens N, Williams E, Burdette EC, Karmarkar P, Bottomley P. A Combined Intravascular MRI Endoscope and Intravascular Ultrasound (IVUS) Transducer for High-Resolution Image-Guided Ablation. Proc Int Soc Magn Reson Med Sci Meet Exhib Int Soc Magn Reson Med Sci Meet Exhib 2017;25:1178.

[3] Xiaoyang Liu, Nicholas Ellens, Emery Williams, Clif Burdette, Parag Karmarkar, Paul Bottomley. Intra-vascular, MRI-Guided, perivascular ultrasound ablation with thermometric monitoring of therapy delivery. Proc. Intl. Soc. Mag. Reson. Med. 26 (2018), Paris, France: 2018, p. 1194.

[4] Xiaoyang Liu, Nicholas Ellens, Emery Williams, Clif Burdette, Parag Karmarkar, Clifford R Weiss, et al. Intravascular MRI Guided Perivascular Ultrasound Ablation, Boston, MA: 2018.

[5] Liu X, Ellens N, Williams E, Burdette EC, Karmarkar P, Weiss CR, et al. High-resolution intravascular MRI-guided perivascular ultrasound ablation. Magnetic Resonance in Medicine 2020;83:240–53. https://doi.org/10.1002/mrm.27932.

[6] Xiaoyang Liu, Parag Karmarkar, Dirk Voit, Jens Frahm, Paul Bottomley. Real-time MRI endoscopy at up to 10 frames/sec. Proc. Intl. Soc. Mag. Reson. Med. 26 (2018), Paris, France: 2018, p. 0603.

[7] Paul Bottomley, Xiaoyang Liu, Parag Karmarkar, Dirk Voit, Jens Frahm, Dara Kraitchman. Real-time MRI Endoscopy, Boston, MA: 2018.

[8] Liu X, Karmarkar P, Voit D, Frahm J, Weiss CR, Kraitchman DL, et al. Real-Time High-Resolution MRI Endoscopy at up to 10 Frames per Second. BME Frontiers 2021;2021. https://doi.org/10.34133/2021/6185616.

[9] Zhang Y, Liu X, Zhou J, Bottomley PA. Ultrafast compartmentalized relaxation time mapping with linear algebraic modeling. Magnetic Resonance in Medicine 2018;79:286–97. https://doi.org/10.1002/mrm.26675.

[10] Wang G, Zhang Y, Hegde SS, Bottomley PA. High-resolution and accelerated multi-parametric mapping with automated characterization of vessel disease using intravascular MRI. Journal of Cardiovascular Magnetic Resonance 2017;19:89. https://doi.org/10.1186/s12968-017-0399-6.

[11] Liu X, Bottomley P. Empirically-Trained Image Contrast Synthesis for Intravascular MRI Endoscopy. Proc. Intl. Soc. Mag. Reson. Med. 28 (2020), 2020, p. 3538.

[12] Lauterbur PC. Image Formation by Induced Local Interactions: Examples Employing Nuclear Magnetic Resonance. Nature 1973;242:190–1. https://doi.org/10.1038/242190a0.

[13] Edelstein WA, Hutchison JMS, Johnson G, Redpath T. Spin warp NMR imaging and applications to human whole-body imaging. Phys Med Biol 1980;25:751–6. https://doi.org/10.1088/0031-9155/25/4/017.

[14] Macovski A. Volumetric NMR imaging with time-varying gradients. Magnetic Resonance in Medicine 1985;2:29–40. https://doi.org/10.1002/mrm.1910020105.

[15] Mansfield P. Multi-planar image formation using NMR spin echoes. J Phys C: Solid State Phys 1977;10:L55–8. https://doi.org/10.1088/0022-3719/10/3/004.

[16] Pipe JG. Motion correction with PROPELLER MRI: Application to head motion and free-breathing cardiac imaging. Magnetic Resonance in Medicine 1999;42:963–9. https://doi.org/10.1002/(SICI)1522-2594(199911)42:5<963::AID-MRM17>3.0.CO;2-L.
[17] Pauly J. Non-Cartesian Reconstruction n.d.:16.
[18] Prince JL, Links JM. Medical imaging signals and systems. 2nd ed. Boston: Pearson; 2015.
[19] Park J, Lee J, Lee J, Lee S-K, Park J-Y. Strategies for rapid reconstruction in 3D MRI with radial data acquisition: 3D fast Fourier transform vs two-step 2D filtered back-projection. Sci Rep 2020;10:13813. https://doi.org/10.1038/s41598-020-70698-4.
[20] Pruessmann KP, Weiger M, Scheidegger MB, Boesiger P. SENSE: Sensitivity encoding for fast MRI. Magnetic Resonance in Medicine 1999;42:952–62. https://doi.org/10.1002/(SICI)1522-2594(199911)42:5<952::AID-MRM16>3.0.CO;2-S.
[21] Griswold MA, Jakob PM, Heidemann RM, Nittka M, Jellus V, Wang J, et al. Generalized autocalibrating partially parallel acquisitions (GRAPPA). Magnetic Resonance in Medicine 2002;47:1202–10. https://doi.org/10.1002/mrm.10171.
[22] Uecker M, Lai P, Murphy MJ, Virtue P, Elad M, Pauly JM, et al. ESPIRiT—an eigenvalue approach to autocalibrating parallel MRI: Where SENSE meets GRAPPA. Magnetic Resonance in Medicine 2014;71:990–1001. https://doi.org/10.1002/mrm.24751.
[23] Wang X, Tan Z, Scholand N, Roeloffs V, Uecker M. Physics-based reconstruction methods for magnetic resonance imaging. Philosophical Transactions of the Royal Society A: Mathematical, Physical and Engineering Sciences 2021;379:20200196. https://doi.org/10.1098/rsta.2020.0196.
[24] Lustig M, Donoho D, Pauly JM. Sparse MRI: The application of compressed sensing for rapid MR imaging. Magnetic Resonance in Medicine 2007;58:1182–95. https://doi.org/10.1002/mrm.21391.
[25] Hammernik K, Klatzer T, Kobler E, Recht MP, Sodickson DK, Pock T, et al. Learning a variational network for reconstruction of accelerated MRI data. Magnetic Resonance in Medicine 2018;79:3055–71. https://doi.org/10.1002/mrm.26977.
[26] Yang Y, Sun J, Li H, Xu Z. Deep ADMM-Net for Compressive Sensing MRI. Advances in Neural Information Processing Systems 2016;29.
[27] Chen JE, Glover GH. Functional Magnetic Resonance Imaging Methods. Neuropsychol Rev 2015;25:289–313. https://doi.org/10.1007/s11065-015-9294-9.
[28] Hagmann P, Jonasson L, Maeder P, Thiran J-P, Wedeen VJ, Meuli R. Understanding Diffusion MR Imaging Techniques: From Scalar Diffusion-weighted Imaging to Diffusion Tensor Imaging and Beyond. RadioGraphics 2006;26:S205–23. https://doi.org/10.1148/rg.26si065510.
[29] Lu H. Physiological MRI of the brain: Emerging techniques and clinical applications. NeuroImage 2019;187:1–2. https://doi.org/10.1016/j.neuroimage.2018.08.047.

[30] van Zijl PCM, Yadav NN. Chemical exchange saturation transfer (CEST): What is in a name and what isn't? Magnetic Resonance in Medicine 2011;65:927–48. https://doi.org/10.1002/mrm.22761.
[31] Deoni SCL, Rutt BK, Peters TM. Rapid combined T1 and T2 mapping using gradient recalled acquisition in the steady state. Magnetic Resonance in Medicine 2003;49:515–26. https://doi.org/10.1002/mrm.10407.
[32] Rieke V, Butts Pauly K. MR thermometry. Journal of Magnetic Resonance Imaging 2008;27:376–90. https://doi.org/10.1002/jmri.21265.
[33] Winter L, Oberacker E, Paul K, Ji Y, Oezerdem C, Ghadjar P, et al. Magnetic resonance thermometry: Methodology, pitfalls and practical solutions. International Journal of Hyperthermia 2016;32:63–75. https://doi.org/10.3109/02656736.2015.1108462.
[34] McDannold N. Quantitative MRI-based temperature mapping based on the proton resonant frequency shift: Review of validation studies. International Journal of Hyperthermia 2005;21:533–46. https://doi.org/10.1080/02656730500096073.
[35] Mintz GS, Guagliumi G. Intravascular imaging in coronary artery disease. The Lancet 2017;390:793–809. https://doi.org/10.1016/S0140-6736(17)31957-8.
[36] Foster FS, Pavlin CJ, Harasiewicz KA, Christopher DA, Turnbull DH. Advances in ultrasound biomicroscopy. Ultrasound in Medicine & Biology 2000;26:1–27. https://doi.org/10.1016/S0301-5629(99)00096-4.
[37] Peng C, Wu H, Kim S, Dai X, Jiang X. Recent Advances in Transducers for Intravascular Ultrasound (IVUS) Imaging. Sensors 2021;21:3540. https://doi.org/10.3390/s21103540.
[38] Fercher AF, Drexler W, Hitzenberger CK, Lasser T. Optical coherence tomography - principles and applications. Rep Prog Phys 2003;66:239–303. https://doi.org/10.1088/0034-4885/66/2/204.
[39] Tearney GJ, Regar E, Akasaka T, Adriaenssens T, Barlis P, Bezerra HG, et al. Consensus standards for acquisition, measurement, and reporting of intravascular optical coherence tomography studies: a report from the International Working Group for Intravascular Optical Coherence Tomography Standardization and Validation. J Am Coll Cardiol 2012;59:1058–72. https://doi.org/10.1016/j.jacc.2011.09.079.
[40] Atalar E, Bottomley PA, Ocali O, Correia LCL, Kelemen MD, Lima JAC, et al. High resolution intravascular MRI and MRS by using a catheter receiver coil. Magnetic Resonance in Medicine 1996;36:596–605. https://doi.org/10.1002/mrm.1910360415.
[41] Ocali O, Atalar E. Intravascular magnetic resonance imaging using a loopless catheter antenna. Magnetic Resonance in Medicine 1997;37:112–8. https://doi.org/10.1002/mrm.1910370116.
[42] Sathyanarayana S, Schär M, Kraitchman DL, Bottomley PA. Towards Real-Time Intravascular Endoscopic Magnetic Resonance Imaging. JACC: Cardiovascular Imaging 2010;3:1158–65. https://doi.org/10.1016/j.jcmg.2010.08.014.
[43] Erturk MA, El-Sharkawy A-MM, Moore J, Bottomley PA. 7 Tesla MRI with a transmit/receive loopless antenna and B1-insensitive selective excitation. Magnetic Resonance in Medicine 2014;72:220–6. https://doi.org/10.1002/mrm.24910.

[44] Hoult DI, Lauterbur PC. The sensitivity of the zeugmatographic experiment involving human samples. Journal of Magnetic Resonance (1969) 1979;34:425–33. https://doi.org/10.1016/0022-2364(79)90019-2.
[45] Edelstein WA, Glover GH, Hardy CJ, Redington RW. The intrinsic signal-to-noise ratio in NMR imaging. Magnetic Resonance in Medicine 1986;3:604–18. https://doi.org/10.1002/mrm.1910030413.
[46] Ocali O, Atalar E. Ultimate intrinsic signal-to-noise ratio in MRI. Magnetic Resonance in Medicine 1998;39:462–73. https://doi.org/10.1002/mrm.1910390317.
[47] Çelik H, Eryaman Y, Altıntaş A, Abdel-Hafez I a., Atalar E. Evaluation of internal MRI coils using ultimate intrinsic SNR. Magnetic Resonance in Medicine 2004;52:640–9. https://doi.org/10.1002/mrm.20200.
[48] Martin AJ, Plewes DB, Henkelman RM. MR imaging of blood vessels with an intravascular coil. Journal of Magnetic Resonance Imaging 1992;2:421–9. https://doi.org/10.1002/jmri.1880020411.
[49] El-Sharkawy A-MM, Qian D, Bottomley PA. The performance of interventional loopless MRI antennae at higher magnetic field strengths. Medical Physics 2008;35:1995–2006. https://doi.org/10.1118/1.2905027.
[50] Sathyanarayana S, Bottomley PA. MRI endoscopy using intrinsically localized probes. Medical Physics 2009;36:908–19. https://doi.org/10.1118/1.3077125.
[51] Ertürk MA, Sathyanarayana Hegde S, Bottomley PA. Radiofrequency Ablation, MR Thermometry, and High-Spatial-Resolution MR Parametric Imaging with a Single, Minimally Invasive Device. Radiology 2016;281:927–32. https://doi.org/10.1148/radiol.2016151447.
[52] Hegde SS, Zhang Y, Bottomley PA. Acceleration and motion-correction techniques for high-resolution intravascular MRI. Magnetic Resonance in Medicine 2015;74:452–61. https://doi.org/10.1002/mrm.25436.
[53] Zhang Y, Gabr RE, Zhou J, Weiss RG, Bottomley PA. Highly-accelerated quantitative 2D and 3D localized spectroscopy with linear algebraic modeling (SLAM) and sensitivity encoding. Journal of Magnetic Resonance 2013;237:125–38. https://doi.org/10.1016/j.jmr.2013.09.018.
[54] Ni Y, Mulier S, Miao Y, Michel L, Marchal G. A review of the general aspects of radiofrequency ablation. Abdom Imaging 2005;30:381–400. https://doi.org/10.1007/s00261-004-0253-9.
[55] Yen Ho S, Sanchez-Quintana D, Cabrera JA, Anderson RH. Anatomy of the Left Atrium: Journal of Cardiovascular Electrophysiology 1999;10:1525–33. https://doi.org/10.1111/j.1540-8167.1999.tb00211.x.
[56] Vuylsteke ME, Mordon SR. Endovenous Laser Ablation: A Review of Mechanisms of Action. Annals of Vascular Surgery 2012;26:424–33. https://doi.org/10.1016/j.avsg.2011.05.037.
[57] Tatli S, Tapan Ü, Morrison PR, Silverman SG. Radiofrequency ablation: technique and clinical applications. Diagnostic and Interventional Radiology 2012;18:508–16. http://dx.doi.org/10.4261/1305-3825.DIR.5168-11.1.
[58] Simon CJ, Dupuy DE, Mayo-Smith WW. Microwave Ablation: Principles and Applications. RadioGraphics 2005;25:S69–83. https://doi.org/10.1148/rg.25si055501.

[59] ter Haar >Gail, Coussios C. High intensity focused ultrasound: Physical principles and devices. International Journal of Hyperthermia 2007;23:89–104. https://doi.org/10.1080/02656730601186138.
[60] Erinjeri JP, Clark TWI. Cryoablation: Mechanism of Action and Devices. Journal of Vascular and Interventional Radiology 2010;21:S187–91. https://doi.org/10.1016/j.jvir.2009.12.403.
[61] Rossi M, Orgera G, Hatzidakis A, Krokidis M. Minimally Invasive Ablation Treatment for Locally Advanced Pancreatic Adenocarcinoma. Cardiovasc Intervent Radiol 2014;37:586–91. https://doi.org/10.1007/s00270-013-0724-x.
[62] Sapareto SA, Dewey WC. Thermal dose determination in cancer therapy. International Journal of Radiation Oncology*Biology*Physics 1984;10:787–800. https://doi.org/10.1016/0360-3016(84)90379-1.
[63] Graham SJ, Chen L, Leitch M, Peters RD, Bronskill MJ, Foster FS, et al. Quantifying tissue damage due to focused ultrasound heating observed by MRI. Magnetic Resonance in Medicine 1999;41:321–8. https://doi.org/10.1002/(SICI)1522-2594(199902)41:2<321::AID-MRM16>3.0.CO;2-9.
[64] Chang IA. Considerations for Thermal Injury Analysis for RF Ablation Devices. Open Biomed Eng J 2010;4:3–12. https://doi.org/10.2174/1874120701004020003.
[65] Davalos RV, Mir LM, Rubinsky B. Tissue Ablation with Irreversible Electroporation. Ann Biomed Eng 2005;33:223. https://doi.org/10.1007/s10439-005-8981-8.
[66] Rubinsky B. Irreversible Electroporation in Medicine: Technology in Cancer Research & Treatment 2016. https://doi.org/10.1177/153303460700600401.
[67] Dougherty TJ, Gomer CJ, Henderson BW, Jori G, Kessel D, Korbelik M, et al. Photodynamic Therapy. JNCI: Journal of the National Cancer Institute 1998;90:889–905. https://doi.org/10.1093/jnci/90.12.889.
[68] Dolmans DEJGJ, Fukumura D, Jain RK. Photodynamic therapy for cancer. Nat Rev Cancer 2003;3:380–7. https://doi.org/10.1038/nrc1071.
[69] Clark TWI. Chemical Ablation of Liver Cancer. Techniques in Vascular and Interventional Radiology 2007;10:58–63. https://doi.org/10.1053/j.tvir.2007.08.004.
[70] Pancreatic Cancer - Cancer Stat Facts. SEER n.d. https://seer.cancer.gov/statfacts/html/pancreas.html (accessed March 13, 2019).
[71] Al-Hawary MM, Francis IR, Chari ST, Fishman EK, Hough DM, Lu DS, et al. Pancreatic Ductal Adenocarcinoma Radiology Reporting Template: Consensus Statement of the Society of Abdominal Radiology and the American Pancreatic Association1. Gastroenterology 2014;146:291-304.e1. https://doi.org/10.1053/j.gastro.2013.11.004.
[72] Buchs NC, Chilcott M, Poletti P-A, Buhler LH, Morel P. Vascular invasion in pancreatic cancer: Imaging modalities, preoperative diagnosis and surgical management. World J Gastroenterol 2010;16:818–31. https://doi.org/10.3748/wjg.v16.i7.818.
[73] Petrou A, Moris D, Paul Tabet P, David Wensley Richards B, Kourounis G. Ablation of the locally advanced pancreatic cancer: An introduction and brief summary of techniques. J BUON 2016;21:650–8.

[74] Cancer Facts & Figures 2019 | American Cancer Society n.d. https://www.cancer.org/research/cancer-facts-statistics/all-cancer-facts-figures/cancer-facts-figures-2019.html (accessed March 13, 2019).
[75] Tabrizian P, Roayaie S, Schwartz ME. Current management of hepatocellular carcinoma. World J Gastroenterol 2014;20:10223–37. https://doi.org/10.3748/wjg.v20.i30.10223.
[76] Maloney E, Hwang JH. Emerging HIFU applications in cancer therapy. Int J Hyperthermia 2015;31:302–9. https://doi.org/10.3109/02656736.2014.969789.
[77] Shiina S, Sato K, Tateishi R, Shimizu M, Ohama H, Hatanaka T, et al. Percutaneous Ablation for Hepatocellular Carcinoma: Comparison of Various Ablation Techniques and Surgery. Canadian Journal of Gastroenterology and Hepatology 2018. https://doi.org/10.1155/2018/4756147.
[78] D'Onofrio M, Ciaravino V, De Robertis R, Barbi E, Salvia R, Girelli R, et al. Percutaneous ablation of pancreatic cancer. World J Gastroenterol 2016;22:9661–73. https://doi.org/10.3748/wjg.v22.i44.9661.
[79] Ahmed M, Brace CL, Lee FT, Goldberg SN. Principles of and Advances in Percutaneous Ablation. Radiology 2011;258:351–69. https://doi.org/10.1148/radiol.10081634.
[80] Linecker M, Pfammatter T, Kambakamba P, DeOliveira ML. Ablation Strategies for Locally Advanced Pancreatic Cancer. Dig Surg 2016;33:351–9. https://doi.org/10.1159/000445021.
[81] Anzidei M, Marincola B, Bezzi M, Brachetti G, Nudo F, Cortesi E, et al. Magnetic Resonance–Guided High-Intensity Focused Ultrasound Treatment of Locally Advanced Pancreatic Adenocarcinoma. Investigative Radiology 2014;49:759–65. https://doi.org/10.1097/RLI.0000000000000080.
[82] Li T, Khokhlova T, Maloney E, Wang Y-N, D'Andrea S, Starr F, et al. Endoscopic high-intensity focused US: technical aspects and studies in an in vivo porcine model (with video). Gastrointestinal Endoscopy 2015;81:1243–50. https://doi.org/10.1016/j.gie.2014.12.019.
[83] Zhou Y. High-Intensity Focused Ultrasound Treatment for Advanced Pancreatic Cancer. Gastroenterology Research and Practice 2014. https://doi.org/10.1155/2014/205325.
[84] Nishimura DG. Principles of magnetic resonance imaging. Ed. 1.1. [Place of Publication Not Identified]: D. Nishimura; 2010.
[85] Rieke V, Pauly KB. MR Thermometry. J Magn Reson Imaging 2008;27:376–90. https://doi.org/10.1002/jmri.21265.
[86] Köhler MO, Mougenot C, Quesson B, Enholm J, Bail BL, Laurent C, et al. Volumetric HIFU ablation under 3D guidance of rapid MRI thermometry. Medical Physics 2009;36:3521–35. https://doi.org/10.1118/1.3152112.
[87] Zhu M, Sun Z, Ng CK. Image-guided thermal ablation with MR-based thermometry. Quant Imaging Med Surg 2017;7:356–68. https://doi.org/10.21037/qims.2017.06.06.
[88] Qian D, Bottomley PA. High-resolution intravascular magnetic resonance quantification of atherosclerotic plaque at 3T. Journal of Cardiovascular Magnetic Resonance 2012;14:20. https://doi.org/10.1186/1532-429X-14-20.

[89] Diederich CJ, Nau WH, Stauffer PR. Ultrasound applicators for interstitial thermal coagulation. IEEE Transactions on Ultrasonics, Ferroelectrics, and Frequency Control 1999;46:1218–28. https://doi.org/10.1109/58.796127.
[90] Prakash P, Salgaonkar VA, Burdette EC, Diederich CJ. Multiple applicator hepatic ablation with interstitial ultrasound devices: Theoretical and experimental investigation. Medical Physics 2012;39:7338–49. https://doi.org/10.1118/1.4765459.
[91] Sinelnikov YD, Fjield T, Sapozhnikov OA. THE MECHANISM OF LESION FORMATION BY FOCUSED ULTRASOUND ABLATION CATHETER FOR TREATMENT OF ATRIAL FIBRILLATION. Acoust Phys 2009;55:647–56. https://doi.org/10.1134/S1063771009040216.
[92] Ghoshal G, Salgaonkar V, Wooton J, Williams E, Neubauer P, Frith L, et al. Ex-vivo and simulation comparison of multi-angular ablation patterns using catheter-based ultrasound transducers. Energy-based Treatment of Tissue and Assessment VII, vol. 8584, International Society for Optics and Photonics; 2013, p. 85840Y. https://doi.org/10.1117/12.2008255.
[93] Ellens N, Partanen A, Ghoshal G, Burdette E, Farahani K. SU-E-J-04: Integration of Interstitial High Intensity Therapeutic Ultrasound Applicators On a Clinical MRI-Guided High Intensity Focused Ultrasound Treatment Planning Software Platform. Medical Physics 2015;42:3264–3264. https://doi.org/10.1118/1.4924092.
[94] Zaporzan B, Waspe AC, Looi T, Mougenot C, Partanen A, Pichardo S. MatMRI and MatHIFU: software toolboxes for real-time monitoring and control of MR-guided HIFU. Journal of Therapeutic Ultrasound 2013;1:7. https://doi.org/10.1186/2050-5736-1-7.
[95] Jouke Smink, Marko Hkkinen, Ronald Holthuizen, Sascha Krueger, Mario Ries, Yasmina Berber, et al. eXTernal Control (XTC): A Flexible, Real-Time, Low-Latency, Bi-Directional Scanner Interface. Proc. Intl. Soc. Mag. Reson. Med. 19, Montréal: 2011, p. 1755.
[96] McDannold NJ, King RL, Jolesz FA, Hynynen KH. Usefulness of MR Imaging-Derived Thermometry and Dosimetry in Determining the Threshold for Tissue Damage Induced by Thermal Surgery in Rabbits. Radiology 2000;216:517–23. https://doi.org/10.1148/radiology.216.2.r00au42517.
[97] Schanda J. Colorimetry: Understanding the CIE System. John Wiley & Sons; 2007.
[98] Caselles V, Kimmel R, Sapiro G. Geodesic Active Contours. International Journal of Computer Vision 1997;22:61–79. https://doi.org/10.1023/A:1007979827043.
[99] Ratnayaka K, Faranesh AZ, Hansen MS, Stine AM, Halabi M, Barbash IM, et al. Real-time MRI-guided right heart catheterization in adults using passive catheters. Eur Heart J 2013;34:380–9. https://doi.org/10.1093/eurheartj/ehs189.
[100] Sathyanarayana S, Schär M, Kraitchman DL, Bottomley PA. Towards Real-Time Intravascular Endoscopic Magnetic Resonance Imaging. JACC Cardiovasc Imaging 2010;3:1158–65. https://doi.org/10.1016/j.jcmg.2010.08.014.
[101] Ishihara Y, Calderon A, Watanabe H, Okamoto K, Suzuki Y, Kuroda K, et al. A precise and fast temperature mapping using water proton chemical shift. Magnetic Resonance in Medicine 1995;34:814–23. https://doi.org/10.1002/mrm.1910340606.
[102] Poorter JD, Wagter CD, Deene YD, Thomsen C, Ståhlberg F, Achten E. Noninvasive MRI Thermometry with the Proton Resonance Frequency (PRF)

Method: In Vivo Results in Human Muscle. Magnetic Resonance in Medicine 1995;33:74–81. https://doi.org/10.1002/mrm.1910330111.
[103] Bing C, Staruch RM, Tillander M, Köhler MO, Mougenot C, Ylihautala M, et al. Drift correction for accurate PRF-shift MR thermometry during mild hyperthermia treatments with MR-HIFU. International Journal of Hyperthermia 2016;32:673–87. https://doi.org/10.1080/02656736.2016.1179799.
[104] Ellens N, Hynynen K. Frequency considerations for deep ablation with high-intensity focused ultrasound: A simulation study. Medical Physics 2015;42:4896–910. https://doi.org/10.1118/1.4927060.
[105] Lee JM, Kim SW, Kim CS, Mun WS. MR Imaging-Histopathologic Correlation of Radiofrequency Thermal Ablation Lesion in a Rabbit Liver Model: Observation during Acute and Chronic Stages. Korean J Radiol 2001;2:151–8. https://doi.org/10.3348/kjr.2001.2.3.151.
[106] Lewin JS, Nour SG, Connell CF, Sulman A, Duerk JL, Resnick MI, et al. Phase II Clinical Trial of Interactive MR Imaging–guided Interstitial Radiofrequency Thermal Ablation of Primary Kidney Tumors: Initial Experience. Radiology 2004;232:835–45. https://doi.org/10.1148/radiol.2323021351.
[107] Lazebnik RS, Breen MS, Fitzmaurice M, Nour SG, Lewin JS, Wilson DL. Radio-frequency-induced thermal lesions: Subacute magnetic resonance appearance and histological correlation. Journal of Magnetic Resonance Imaging 2003;18:487–95. https://doi.org/10.1002/jmri.10382.
[108] Lazebnik RS, Weinberg BD, Breen MS, Lewin JS, Wilson DL. Sub-acute changes in lesion conspicuity and geometry following MR-guided radiofrequency ablation. Journal of Magnetic Resonance Imaging 2003;18:353–9. https://doi.org/10.1002/jmri.10352.
[109] Bergheanu SC, Bodde MC, Jukema JW. Pathophysiology and treatment of atherosclerosis. Neth Heart J 2017;25:231–42. https://doi.org/10.1007/s12471-017-0959-2.
[110] Malakar AK, Choudhury D, Halder B, Paul P, Uddin A, Chakraborty S. A review on coronary artery disease, its risk factors, and therapeutics. J Cell Physiol 2019. https://doi.org/10.1002/jcp.28350.
[111] Nabel EG, Braunwald EE. A tale of coronary artery disease and myocardial infarction. The New England Journal of Medicine 2012;366:54–63. https://doi.org/10.1056/NEJMra1112570.
[112] Calvert PA, Obaid DR, O'Sullivan M, Shapiro LM, McNab D, Densem CG, et al. Association Between IVUS Findings and Adverse Outcomes in Patients With Coronary Artery Disease: The VIVA (VH-IVUS in Vulnerable Atherosclerosis) Study. JACC: Cardiovascular Imaging 2011;4:894–901. https://doi.org/10.1016/j.jcmg.2011.05.005.
[113] Yun KH, Mintz GS, Farhat N, Marso SP, Taglieri N, Verheye S, et al. Relation Between Angiographic Lesion Severity, Vulnerable Plaque Morphology and Future Adverse Cardiac Events (from the Providing Regional Observations to Study Predictors of Events in the Coronary Tree Study). American Journal of Cardiology 2012;110:471–7. https://doi.org/10.1016/j.amjcard.2012.04.018.
[114] Cheng JM, Garcia-Garcia HM, de Boer SPM, Kardys I, Heo JH, Akkerhuis KM, et al. In vivo detection of high-risk coronary plaques by radiofrequency

intravascular ultrasound and cardiovascular outcome: results of the ATHEROREMO-IVUS study. Eur Heart J 2014;35:639–47. https://doi.org/10.1093/eurheartj/eht484.
[115] Stary Herbert C., Chandler A. Bleakley, Dinsmore Robert E., Fuster Valentin, Glagov Seymour, Insull William, et al. A Definition of Advanced Types of Atherosclerotic Lesions and a Histological Classification of Atherosclerosis. Circulation 1995;92:1355–74. https://doi.org/10.1161/01.CIR.92.5.1355.
[116] Fuster V, Moreno PR, Fayad ZA, Corti R, Badimon JJ. Atherothrombosis and High-Risk Plaque: Part I: Evolving Concepts. Journal of the American College of Cardiology 2005;46:937–54. https://doi.org/10.1016/j.jacc.2005.03.074.
[117] Ochijewicz D, Tomaniak M, Koltowski L, Rdzanek A, Pietrasik A, Kochman J. Intravascular imaging of coronary artery disease: recent progress and future directions. Journal of Cardiovascular Medicine 2017;18:733. https://doi.org/10.2459/JCM.0000000000000552.
[118] Matthews SD, Frishman WH. A Review of the Clinical Utility of Intravascular Ultrasound and Optical Coherence Tomography in the Assessment and Treatment of Coronary Artery Disease. [Review]. Cardiology in Review 2017;25:68–76. https://doi.org/10.1097/CRD.0000000000000128.
[119] Meissner OA, Rieger J, Rieber J, Klauss V, Siebert U, Tató F, et al. High-resolution MR Imaging of Human Atherosclerotic Femoral Arteries In Vivo: Validation with Intravascular Ultrasound. Journal of Vascular and Interventional Radiology 2003;14:227–31. https://doi.org/10.1097/01.RVI.0000058325.82956.63.
[120] Devuyst Gérald, Ruchat Patrick, Karapanayiotides Theodoros, Jonasson Lisa, Cuisinaire Olivier, Lobrinus Johannes-Alexander, et al. Ultrasound Measurement of the Fibrous Cap in Symptomatic and Asymptomatic Atheromatous Carotid Plaques. Circulation 2005;111:2776–82. https://doi.org/10.1161/CIRCULATIONAHA.104.483024.
[121] Kume T, Akasaka T, Kawamoto T, Watanabe N, Toyota E, Neishi Y, et al. Assessment of Coronary Intima - Media Thickness by Optical Coherence Tomography. Circ J 2005;69:903–7. https://doi.org/10.1253/circj.69.903.
[122] Uecker M, Zhang S, Voit D, Karaus A, Merboldt K-D, Frahm J. Real-time MRI at a resolution of 20 ms. NMR Biomed 2010;23:986–94. https://doi.org/10.1002/nbm.1585.
[123] Uecker M, Zhang S, Frahm J. Nonlinear inverse reconstruction for real-time MRI of the human heart using undersampled radial FLASH. Magnetic Resonance in Medicine 2010;63:1456–62. https://doi.org/10.1002/mrm.22453.
[124] Uecker M, Hohage T, Block KT, Frahm J. Image reconstruction by regularized nonlinear inversion—Joint estimation of coil sensitivities and image content. Magnetic Resonance in Medicine 2008;60:674–82. https://doi.org/10.1002/mrm.21691.
[125] Garwood M, Ke Y. Symmetric pulses to induce arbitrary flip angles with compensation for rf inhomogeneity and resonance offsets. Journal of Magnetic Resonance (1969) 1991;94:511–25. https://doi.org/10.1016/0022-2364(91)90137-I.
[126] Schaetz S, Uecker M. A multi-GPU Programming Library for Real-time Applications. Proceedings of the 12th International Conference on Algorithms and

Architectures for Parallel Processing - Volume Part I, Berlin, Heidelberg: Springer-Verlag; 2012, p. 114–28. https://doi.org/10.1007/978-3-642-33078-0_9.
[127] Frahm J, Haase A, Matthaei D. Rapid NMR imaging of dynamic processes using the FLASII technique. Magnetic Resonance in Medicine 1986;3:321–7. https://doi.org/10.1002/mrm.1910030217.
[128] Bottomley PA, Ouwerkerk R. BIRP, an Improved Implementation of Low-Angle Adiabatic (BIR-4) Excitation Pulses. Journal of Magnetic Resonance, Series A 1993;103:242–4. https://doi.org/10.1006/jmra.1993.1162.
[129] Maes F, Vandermeulen D, Suetens P. Medical image registration using mutual information. Proceedings of the IEEE 2003;91:1699–722. https://doi.org/10.1109/JPROC.2003.817864.
[130] Zhou Wang, Bovik AC, Sheikh HR, Simoncelli EP. Image quality assessment: from error visibility to structural similarity. IEEE Transactions on Image Processing 2004;13:600–12. https://doi.org/10.1109/TIP.2003.819861.
[131] Li C, Bovik AC. Content-weighted video quality assessment using a three-component image model. JEI 2010;19:011003. https://doi.org/10.1117/1.3267087.
[132] Lee J, Kim J, Kim M, Hwang J, Hwang Y, Kang J-W, et al. Extremely low-frame-rate digital fluoroscopy in catheter ablation of atrial fibrillation: A comparison of 2 versus 4 frame rate. Medicine 2017;96. https://doi.org/10.1097/MD.0000000000007200.
[133] Ignacio Fernandez-Urien CC, Nez PM, N JN. Capsule endoscopy capture rate: Has 4 frames-per-second any impact over 2 frames-per-second? World Journal of Gastroenterology 2014;20:14472–8. https://doi.org/10.3748/wjg.v20.i39.14472.
[134] Mitselos IV, Christodoulou DK. What defines quality in small bowel capsule endoscopy. Annals of Translational Medicine 2018;6. https://doi.org/10.21037/19681.
[135] Katsura M, Sato J, Akahane M, Kunimatsu A, Abe O. Current and Novel Techniques for Metal Artifact Reduction at CT: Practical Guide for Radiologists. RadioGraphics 2018;38:450–61. https://doi.org/10.1148/rg.2018170102.
[136] Boas FE, Fleischmann D. CT artifacts: causes and reduction techniques. Imaging in Medicine 2012;4:229–40. http://dx.doi.org/10.2217/iim.12.13.
[137] Bottomley PA. Turning Up the Heat on MRI. J Am Coll Radiol 2008;5:853–5. https://doi.org/10.1016/j.jacr.2008.04.003.
[138] Bottomley PA, Kumar A, Edelstein WA, Allen JM, Karmarkar PV. Designing passive MRI-safe implantable conducting leads with electrodes. Medical Physics 2010;37:3828–43. https://doi.org/10.1118/1.3439590.
[139] Hegde SS, Weiss CR, Erturk MA, Bottomley PA. 3T intravascular MRI, IVUS and OCT: A study in contrast. Proc Int Soc Magn Reson Med Sci Meet Exhib Int Soc Magn Reson Med Sci Meet Exhib 2013;21:1833.
[140] Bottomley PA, Foster TH, Argersinger RE, Pfeifer LM. A review of normal tissue hydrogen NMR relaxation times and relaxation mechanisms from 1–100 MHz: Dependence on tissue type, NMR frequency, temperature, species, excision, and age. Medical Physics 1984;11:425–48. https://doi.org/10.1118/1.595535.

[141] Bottomley PA, Hardy CJ, Argersinger RE, Allen-Moore G. A review of 1H nuclear magnetic resonance relaxation in pathology: Are T1 and T2 diagnostic? Medical Physics 1987;14:1–37. https://doi.org/10.1118/1.596111.
[142] Schmitt P, Griswold MA, Jakob PM, Kotas M, Gulani V, Flentje M, et al. Inversion recovery TrueFISP: Quantification of T1, T2, and spin density. Magnetic Resonance in Medicine 2004;51:661–7. https://doi.org/10.1002/mrm.20058.
[143] Look DC, Locker DR. Time Saving in Measurement of NMR and EPR Relaxation Times. Review of Scientific Instruments 1970;41:250–1. https://doi.org/10.1063/1.1684482.
[144] Henderson E, McKinnon G, Lee T-Y, Rutt BK. A fast 3D Look-Locker method for volumetric T1 mapping. Magnetic Resonance Imaging 1999;17:1163–71. https://doi.org/10.1016/S0730-725X(99)00025-9.
[145] Haase A. Snapshot flash mri. applications to t1, t2, and chemical-shift imaging. Magnetic Resonance in Medicine 1990;13:77–89. https://doi.org/10.1002/mrm.1910130109.
[146] Wang G, El-Sharkawy AM, Edelstein WA, Schär M, Bottomley PA. Measuring T2 and T1, and imaging T2 without spin echoes. Journal of Magnetic Resonance 2012;214:273–80. https://doi.org/10.1016/j.jmr.2011.11.016.
[147] Wang G, El-Sharkawy A-MM, Bottomley PA. Minimum acquisition methods for simultaneously imaging T1, T2, and proton density with B1 correction and no spin-echoes. Journal of Magnetic Resonance 2014;242:243–55. https://doi.org/10.1016/j.jmr.2014.02.010.
[148] Ma D, Gulani V, Seiberlich N, Liu K, Sunshine JL, Duerk JL, et al. Magnetic resonance fingerprinting. Nature 2013;495:187–92. https://doi.org/10.1038/nature11971.
[149] Messroghli DR, Radjenovic A, Kozerke S, Higgins DM, Sivananthan MU, Ridgway JP. Modified Look-Locker inversion recovery (MOLLI) for high-resolution T1 mapping of the heart. Magnetic Resonance in Medicine 2004;52:141–6. https://doi.org/10.1002/mrm.20110.
[150] Chow K, Flewitt JA, Green JD, Pagano JJ, Friedrich MG, Thompson RB. Saturation recovery single-shot acquisition (SASHA) for myocardial T1 mapping. Magnetic Resonance in Medicine 2014;71:2082–95. https://doi.org/10.1002/mrm.24878.
[151] Brix G, Schad LR, Deimling M, Lorenz WJ. Fast and precise T1 imaging using a TOMROP sequence. Magnetic Resonance Imaging 1990;8:351–6. https://doi.org/10.1016/0730-725X(90)90041-Y.
[152] Hattingen E, Jurcoane A, Daneshvar K, Pilatus U, Mittelbronn M, Steinbach JP, et al. Quantitative T2 mapping of recurrent glioblastoma under bevacizumab improves monitoring for non-enhancing tumor progression and predicts overall survival. Neuro-Oncology 2013;15:1395–404. https://doi.org/10.1093/neuonc/not105.
[153] Li W, Liu P, Lu H, Strouse JJ, van Zijl PCM, Qin Q. Fast measurement of blood T1 in the human carotid artery at 3T: Accuracy, precision, and reproducibility. Magnetic Resonance in Medicine 2017;77:2296–302. https://doi.org/10.1002/mrm.26325.

[154] Heo H-Y, Zhang Y, Jiang S, Lee D-H, Zhou J. Quantitative assessment of amide proton transfer (APT) and nuclear overhauser enhancement (NOE) imaging with extrapolated semisolid magnetization transfer reference (EMR) signals: II. Comparison of three EMR models and application to human brain glioma at 3 Tesla. Magnetic Resonance in Medicine 2016;75:1630–9. https://doi.org/10.1002/mrm.25795.
[155] Heo H-Y, Zhang Y, Lee D-H, Hong X, Zhou J. Quantitative assessment of amide proton transfer (APT) and nuclear overhauser enhancement (NOE) imaging with extrapolated semi-solid magnetization transfer reference (EMR) signals: Application to a rat glioma model at 4.7 tesla. Magnetic Resonance in Medicine 2016;75:137–49. https://doi.org/10.1002/mrm.25581.
[156] Zhou J, Zhu H, Lim M, Blair L, Quinones-Hinojosa A, Messina SA, et al. Three-dimensional amide proton transfer MR imaging of gliomas: Initial experience and comparison with gadolinium enhancement. Journal of Magnetic Resonance Imaging 2013;38:1119–28. https://doi.org/10.1002/jmri.24067.
[157] Zhang Y, Gabr RE, Schär M, Weiss RG, Bottomley PA. Magnetic resonance Spectroscopy with Linear Algebraic Modeling (SLAM) for higher speed and sensitivity. Journal of Magnetic Resonance 2012;218:66–76. https://doi.org/10.1016/j.jmr.2012.03.008.
[158] Bottomley PA, Zhang Y. Accelerated Spatially Encoded Spectroscopy of Arbitrarily Shaped Compartments Using Prior Knowledge and Linear Algebraic Modeling. eMagRes, John Wiley & Sons, Ltd; 2015, p. 89–104. https://doi.org/10.1002/9780470034590.emrstm1438.
[159] Zhang Y, Heo H-Y, Jiang S, Lee D-H, Bottomley PA, Zhou J. Highly accelerated chemical exchange saturation transfer (CEST) measurements with linear algebraic modeling. Magnetic Resonance in Medicine 2016;76:136–44. https://doi.org/10.1002/mrm.25873.
[160] Zhang Y, Zhou J, Bottomley PA. Minimizing lipid signal bleed in brain 1H chemical shift imaging by post-acquisition grid shifting. Magnetic Resonance in Medicine 2015;74:320–9. https://doi.org/10.1002/mrm.25438.
[161] Brooker HR, Mareci TH, Mao J. Selective fourier transform localization. Magnetic Resonance in Medicine 1987;5:417–33. https://doi.org/10.1002/mrm.1910050503.
[162] Dydak U, Weiger M, Pruessmann KP, Meier D, Boesiger P. Sensitivity-encoded spectroscopic imaging. Magnetic Resonance in Medicine 2001;46:713–22. https://doi.org/10.1002/mrm.1250.
[163] Zhang Y, Heo H-Y, Lee D-H, Jiang S, Zhao X, Bottomley PA, et al. Chemical exchange saturation transfer (CEST) imaging with fast variably-accelerated sensitivity encoding (vSENSE). Magnetic Resonance in Medicine 2017;77:2225–38. https://doi.org/10.1002/mrm.26307.
[164] Silver MS, Joseph RI, Hoult DI. Highly selective π2 and π pulse generation. Journal of Magnetic Resonance (1969) 1984;59:347–51. https://doi.org/10.1016/0022-2364(84)90181-1.
[165] Hennig J, Nauerth A, Friedburg H. RARE imaging: A fast imaging method for clinical MR. Magnetic Resonance in Medicine 1986;3:823–33. https://doi.org/10.1002/mrm.1910030602.

[166] Haase A, Frahm J, Matthaei D, Hanicke W, Merboldt K-D. FLASH imaging. Rapid NMR imaging using low flip-angle pulses. Journal of Magnetic Resonance (1969) 1986;67:258–66. https://doi.org/10.1016/0022-2364(86)90433-6.
[167] Yarnykh VL. Actual flip-angle imaging in the pulsed steady state: A method for rapid three-dimensional mapping of the transmitted radiofrequency field. Magnetic Resonance in Medicine 2007;57:192–200. https://doi.org/10.1002/mrm.21120.
[168] Hajnal JV, Bryant DJ, Kasuboski L, Pattany PM, Coene BD, Lewis PD, et al. Use of Fluid Attenuated Inversion Recovery (FLAIR) Pulse Sequences in MRI of the Brain. Journal of Computer Assisted Tomography 1992;16:841–4.
[169] Mugler III JP, Brookeman JR. Three-dimensional magnetization-prepared rapid gradient-echo imaging (3D MP RAGE). Magnetic Resonance in Medicine 1990;15:152–7. https://doi.org/10.1002/mrm.1910150117.
[170] Wang D, Doddrell DM, Cowin G. A novel phantom and method for comprehensive 3-dimensional measurement and correction of geometric distortion in magnetic resonance imaging. Magnetic Resonance Imaging 2004;22:529–42. https://doi.org/10.1016/j.mri.2004.01.008.
[171] Zhou J, Blakeley JO, Hua J, Kim M, Laterra J, Pomper MG, et al. Practical data acquisition method for human brain tumor amide proton transfer (APT) imaging. Magnetic Resonance in Medicine 2008;60:842–9. https://doi.org/10.1002/mrm.21712.
[172] de Bazelaire CMJ, Duhamel GD, Rofsky NM, Alsop DC. MR Imaging Relaxation Times of Abdominal and Pelvic Tissues Measured in Vivo at 3.0 T: Preliminary Results. Radiology 2004;230:652–9. https://doi.org/10.1148/radiol.2303021331.
[173] Gold GE, Han E, Stainsby J, Wright G, Brittain J, Beaulieu C. Musculoskeletal MRI at 3.0 T: Relaxation Times and Image Contrast. American Journal of Roentgenology 2004;183:343–51. https://doi.org/10.2214/ajr.183.2.1830343.
[174] Deng J, Larson AC. Modified PROPELLER approach for T2-mapping of the abdomen. Magnetic Resonance in Medicine 2009;61:1269–78. https://doi.org/10.1002/mrm.21989.
[175] Pai A, Li X, Majumdar S. A comparative study at 3 T of sequence dependence of T2 quantitation in the knee. Magnetic Resonance Imaging 2008;26:1215–20. https://doi.org/10.1016/j.mri.2008.02.017.
[176] Wansapura JP, Holland SK, Dunn RS, Ball Jr. WS. NMR relaxation times in the human brain at 3.0 tesla. Journal of Magnetic Resonance Imaging 1999;9:531–8. https://doi.org/10.1002/(SICI)1522-2586(199904)9:4<531::AID-JMRI4>3.0.CO;2-L.
[177] Lu H, Nagae-Poetscher LM, Golay X, Lin D, Pomper M, van Zijl PCM. Routine clinical brain MRI sequences for use at 3.0 Tesla. Journal of Magnetic Resonance Imaging 2005;22:13–22. https://doi.org/10.1002/jmri.20356.
[178] Hu X, Levin DN, Lauterbur PC, Spraggins T. SLIM: Spectral localization by imaging. Magnetic Resonance in Medicine 1988;8:314–22. https://doi.org/10.1002/mrm.1910080308.
[179] Liang Z-P, Lauterbur PC. A generalized series approach to MR spectroscopic imaging. IEEE Transactions on Medical Imaging 1991;10:132–7. https://doi.org/10.1109/42.79470.

[180] von Kienlin M, Mejia R. Spectral localization with optimal pointspread function. Journal of Magnetic Resonance (1969) 1991;94:268–87. https://doi.org/10.1016/0022-2364(91)90106-4.
[181] Khalidov I, Van De Ville D, Jacob M, Lazeyras F, Unser M. BSLIM: Spectral Localization by Imaging With Explicit $_0$ Field Inhomogeneity Compensation. IEEE Transactions on Medical Imaging 2007;26:990–1000. https://doi.org/10.1109/TMI.2007.897385.
[182] Doneva M, Börnert P, Eggers H, Stehning C, Sénégas J, Mertins A. Compressed sensing reconstruction for magnetic resonance parameter mapping. Magnetic Resonance in Medicine 2010;64:1114–20. https://doi.org/10.1002/mrm.22483.
[183] Sumpf TJ, Uecker M, Boretius S, Frahm J. Model-based nonlinear inverse reconstruction for T2 mapping using highly undersampled spin-echo MRI. Journal of Magnetic Resonance Imaging 2011;34:420–8. https://doi.org/10.1002/jmri.22634.
[184] Huang C, Graff CG, Clarkson EW, Bilgin A, Altbach MI. T2 mapping from highly undersampled data by reconstruction of principal component coefficient maps using compressed sensing. Magnetic Resonance in Medicine 2012;67:1355–66. https://doi.org/10.1002/mrm.23128.
[185] Zhao B, Lu W, Hitchens TK, Lam F, Ho C, Liang Z-P. Accelerated MR parameter mapping with low-rank and sparsity constraints. Magnetic Resonance in Medicine 2015;74:489–98. https://doi.org/10.1002/mrm.25421.
[186] Zhang T, Pauly JM, Levesque IR. Accelerating parameter mapping with a locally low rank constraint. Magnetic Resonance in Medicine 2015;73:655–61. https://doi.org/10.1002/mrm.25161.
[187] Velikina JV, Alexander AL, Samsonov A. Accelerating MR parameter mapping using sparsity-promoting regularization in parametric dimension. Magnetic Resonance in Medicine 2013;70:1263–73. https://doi.org/10.1002/mrm.24577.
[188] Block KT, Uecker M, Frahm J. Model-Based Iterative Reconstruction for Radial Fast Spin-Echo MRI. IEEE Transactions on Medical Imaging 2009;28:1759–69. https://doi.org/10.1109/TMI.2009.2023119.
[189] Song HK, Dougherty L. k-Space weighted image contrast (KWIC) for contrast manipulation in projection reconstruction MRI. Magnetic Resonance in Medicine 2000;44:825–32. https://doi.org/10.1002/1522-2594(200012)44:6<825::AID-MRM2>3.0.CO;2-D.
[190] Altbach MI, Bilgin A, Li Z, Clarkson EW, Trouard TP, Gmitro AF. Processing of radial fast spin-echo data for obtaining T2 estimates from a single k-space data set. Magnetic Resonance in Medicine 2005;54:549–59. https://doi.org/10.1002/mrm.20611.
[191] Van Vaals JJ, Brummer ME, Thomas Dixon W, Tuithof HH, Engels H, Nelson RC, et al. “Keyhole” method for accelerating imaging of contrast agent uptake. Journal of Magnetic Resonance Imaging 1993;3:671–5. https://doi.org/10.1002/jmri.1880030419.
[192] Wheaton AJ, Borthakur A, Reddy R. Application of the keyhole technique to T1ρ relaxation mapping. Journal of Magnetic Resonance Imaging 2003;18:745–9. https://doi.org/10.1002/jmri.10412.

[193] Atkinson DJ, Edelman RR. Cineangiography of the heart in a single breath hold with a segmented turboFLASH sequence. Radiology 1991;178:357–60. https://doi.org/10.1148/radiology.178.2.1987592.
[194] Leung DG, Carrino JA, Wagner KR, Jacobs MA. Whole-body magnetic resonance imaging evaluation of facioscapulohumeral muscular dystrophy. Muscle & Nerve 2015;52:512–20. https://doi.org/10.1002/mus.24569.
[195] Morone M, Bali MA, Tunariu N, Messiou C, Blackledge M, Grazioli L, et al. Whole-Body MRI: Current Applications in Oncology. American Journal of Roentgenology 2017;209:W336–49. https://doi.org/10.2214/AJR.17.17984.
[196] Frahm J, Voit D, Uecker M. Real-Time Magnetic Resonance Imaging: Radial Gradient-Echo Sequences With Nonlinear Inverse Reconstruction. Investigative Radiology 2019;54:757–66. https://doi.org/10.1097/RLI.0000000000000584.
[197] Zhang S, Joseph AA, Voit D, Schaetz S, Merboldt K-D, Unterberg-Buchwald C, et al. Real-time magnetic resonance imaging of cardiac function and flow—Recent progress. Quantitative Imaging in Medicine and Surgery 2014;4:31329–31329.
[198] Thompson SM, Gorny KR, Koepsel EMK, Welch BT, Mynderse L, Lu A, et al. Body Interventional MRI for Diagnostic and Interventional Radiologists: Current Practice and Future Prospects. RadioGraphics 2021;41:1785–801. https://doi.org/10.1148/rg.2021210040.
[199] Shahid M, Rossholm A, Lövström B, Zepernick H-J. No-reference image and video quality assessment: a classification and review of recent approaches. EURASIP Journal on Image and Video Processing 2014;2014:40. https://doi.org/10.1186/1687-5281-2014-40.
[200] Liu X, van de Weijer J, Bagdanov AD. RankIQA: Learning From Rankings for No-Reference Image Quality Assessment, 2017, p. 1040–9.
[201] Athar S, Wang Z. A Comprehensive Performance Evaluation of Image Quality Assessment Algorithms. IEEE Access 2019;7:140030–70. https://doi.org/10.1109/ACCESS.2019.2943319.
[202] Weigel M. Extended phase graphs: Dephasing, RF pulses, and echoes - pure and simple. Journal of Magnetic Resonance Imaging 2015;41:266–95. https://doi.org/10.1002/jmri.24619.
[203] Weigel M, Schwenk S, Kiselev VG, Scheffler K, Hennig J. Extended phase graphs with anisotropic diffusion. Journal of Magnetic Resonance 2010;205:276–85. https://doi.org/10.1016/j.jmr.2010.05.011.
[204] Gómez PA, Molina-Romero M, Buonincontri G, Menzel MI, Menze BH. Designing contrasts for rapid, simultaneous parameter quantification and flow visualization with quantitative transient-state imaging. Scientific Reports 2019;9:8468. https://doi.org/10.1038/s41598-019-44832-w.
[205] Kellman P, Hansen MS, Nielles-Vallespin S, Nickander J, Themudo R, Ugander M, et al. Myocardial perfusion cardiovascular magnetic resonance: optimized dual sequence and reconstruction for quantification. Journal of Cardiovascular Magnetic Resonance 2017;19:43. https://doi.org/10.1186/s12968-017-0355-5.
[206] Lee D, Kim J, Moon W-J, Ye JC. CollaGAN : Collaborative GAN for Missing Image Data Imputation. ArXiv:190109764 [Cs, Stat] 2019.
[207] Yang H, Sun J, Carass A, Zhao C, Lee J, Xu Z, et al. Unpaired Brain MR-to-CT Synthesis Using a Structure-Constrained CycleGAN. In: Stoyanov D, Taylor Z,

Carneiro G, Syeda-Mahmood T, Martel A, Maier-Hein L, et al., editors. Deep Learning in Medical Image Analysis and Multimodal Learning for Clinical Decision Support, Springer International Publishing; 2018, p. 174–82.
[208] Pedersen H, Kozerke S, Ringgaard S, Nehrke K, Kim WY. k-t PCA: Temporally constrained k-t BLAST reconstruction using principal component analysis. Magnetic Resonance in Medicine 2009;62:706–16. https://doi.org/10.1002/mrm.22052.
[209] Tsao J, Boesiger P, Pruessmann KP. k-t BLAST and k-t SENSE: Dynamic MRI with high frame rate exploiting spatiotemporal correlations. Magnetic Resonance in Medicine 2003;50:1031–42. https://doi.org/10.1002/mrm.10611.
[210] Doneva M, Amthor T, Koken P, Sommer K, Börnert P. Matrix completion-based reconstruction for undersampled magnetic resonance fingerprinting data. Magnetic Resonance Imaging 2017;41:41–52. https://doi.org/10.1016/j.mri.2017.02.007.
[211] Tamir JI, Uecker M, Chen W, Lai P, Alley MT, Vasanawala SS, et al. T2 shuffling: Sharp, multicontrast, volumetric fast spin-echo imaging. Magnetic Resonance in Medicine 2017;77:180–95. https://doi.org/10.1002/mrm.26102.
[212] Shi C, Zhou Y, Wang Y, Lyu J, Liang D, Ying L. Recovery of parametric manifold from reduced measurements: Application to magnetic resonance parameter mapping. 2015 IEEE 12th International Symposium on Biomedical Imaging (ISBI), 2015, p. 901–4. https://doi.org/10.1109/ISBI.2015.7164016.
[213] Zhou Y, Shi C, Ren F, Lyu J, Liang D, Ying L. Accelerating MR parameter mapping using nonlinear manifold learning and supervised pre-imaging. 2015 IEEE 12th International Symposium on Biomedical Imaging (ISBI), 2015, p. 897–900. https://doi.org/10.1109/ISBI.2015.7164015.
[214] Zhu B, Liu JZ, Cauley SF, Rosen BR, Rosen MS. Image reconstruction by domain-transform manifold learning. Nature 2018;555:487–92. https://doi.org/10.1038/nature25988.
[215] Bugata P, Drotár P. Feature Selection Based on a Sparse Neural-Network Layer With Normalizing Constraints. IEEE Transactions on Cybernetics 2021:1–12. https://doi.org/10.1109/TCYB.2021.3087776.
[216] Golbabaee M, Buonincontri G, Pirkl C, Menzel M, Menze B, Davies M, et al. Compressive MRI quantification using convex spatiotemporal priors and deep auto-encoders. ArXiv:200108746 [Physics] 2020.
[217] Paszke A, Gross S, Massa F, Lerer A, Bradbury J, Chanan G, et al. PyTorch: an imperative style, high-performance deep learning library. Proceedings of the 33rd International Conference on Neural Information Processing Systems, Red Hook, NY, USA: Curran Associates Inc.; 2019, p. 8026–37.
[218] Kingma DP, Ba J. Adam: A Method for Stochastic Optimization. ArXiv:14126980 [Cs] 2017.

Curriculum Vitae

Education

Ph.D.	Johns Hopkins University Electrical and Computer Engineering Advisor: Paul A. Bottomley	Baltimore, MD, USA	2022
M.S.E.	Johns Hopkins University Electrical and Computer Engineering	Baltimore, MD, USA	2017
B.Sc.	Peking University Physics	Beijing, China	2014

Awards

1st Place for Best Oral Presentation, Interventional MR Study Group, ISMRM, Jun 2018

The ISMRM Magna Cum Laude Merit Award, ISMRM, Jun 2018

Outstanding Graduate Award of Beijing, Jun 2014

Outstanding Graduate Award of Peking University, Jun 2014

First-class Scholarship for Freshmen of Peking University, Sep 2010

Journal Articles

Xiaoyang Liu, Parag Karmarkar, Dirk Voit, Jens Frahm, Clifford R. Weiss, Dara L. Kraitchman, Paul A. Bottomley. Real-Time High-Resolution MRI Endoscopy at up to 10 Frames per Second. *BME Frontiers*. DOI: 10.34133/2021/6185616

Xiaoyang Liu, Nicholas Ellens, Emery Williams, Everette C. Burdette, Parag Karmarkar, Clifford R. Weiss, Dara Kraitchman, Paul A. Bottomley. High-resolution intravascular MRI-guided perivascular ultrasound ablation. *Magnetic Resonance in Medicine*. DOI: 10.1002/mrm.27932

Xiaoyang Liu, Paul A. Bottomley. Towards automated image contrast optimization in MRI. (finalized draft ready for submission)

Yi Zhang, Xiaoyang Liu, Jinyuan Zhou, and Paul A. Bottomley. Ultrafast Compartmentalized Relaxation Time Mapping With Linear Algebraic Modeling. *Magnetic Resonance in Medicine* (2018). 79:286–297

Conference Abstracts

Xiaoyang Liu and Paul Bottomley. Empirically-Trained Image Contrast Synthesis for Intravascular MRI Endoscopy. *Proc. Intl. Soc. Mag. Reson. Med. 28* (2020). 3538

Xiaoyang Liu, Nicholas Ellens, Emery Williams, Clif Burdette, Parag Karmarkar, and Paul Bottomley. Intra-vascular, MRI-Guided, perivascular ultrasound ablation with thermometric monitoring of therapy delivery. *Proc. Intl. Soc. Mag. Reson. Med. 26* (2018). 1194

Xiaoyang Liu, Parag Karmarkar, Dirk Voit, Jens Frahm, and Paul Bottomley. Real-time MRI endoscopy at up to 10 frames/sec. *Proc. Intl. Soc. Mag. Reson. Med. 26* (2018). 0603

Xiaoyang Liu, Nicholas Ellens, Emery Williams, Clif Burdette, Parag Karmarkar, Clifford R Weiss, Dara L Kraitchman, and Paul A Bottomley. Intravascular MRI Guided Perivascular Ultrasound Ablation. Proceedings of the 12th Interventional MRI Symposium (2018). 28

Paul Bottomley, Xiaoyang Liu, Parag Karmarkar, Dirk Voit, Jens Frahm, Dara Kraitchman. Real-time MRI Endoscopy. Proceedings of the 12th Interventional MRI Symposium (2018). 27

Xiaoyang Liu, Nicholas Ellens, Emery Williams, Everette Clif Burdette, Parag Karmarkar, and Paul Bottomley. A Combined Intravascular MRI Endoscope and Intravascular Ultrasound (IVUS) Transducer for High-Resolution Image-Guided Ablation. *Proc. Intl. Soc. Mag. Reson. Med. 25* (2017). 1178

Xiaoyang Liu, Nicholas Ellens, Parag Karmarkar, and Paul Bottomley. Multifunctional Intravascular MRI-Ultrasound Ablation/Imaging/Thermometry System. Proceedings of the 11th Interventional MRI Symposium (2016).

Invited Talks

Lessons Learned from Intravascular Magnetic Resonance Imaging. College of Biomedical Engineering and Instrument Science, Zhejiang University, China. 2019.

Intravascular MRI Endoscopy at 10 frames/sec. 21st Annual Division of MR Research Retreat. Department of Radiology, Johns Hopkins University. 2018.

Progress on Real-time MRI Endoscopy. Siemens Seminar. Department of Radiology, Johns Hopkins University. 2018.

Intravascular MRI-guided Perivascular Ablation. 20th Annual Division of MR Research Retreat. Department of Radiology, Johns Hopkins University. 2017.

An Image-guided Intravascular MRI-Ultrasound Ablation System. 19th Annual Division of MR Research Retreat. Department of Radiology, Johns Hopkins University. 2016.